Infrared Surface Brightness Fluctuation Distances for MASSIVE and Type Ia Supernova Host Galaxies[*]

Joseph B. Jensen,[1] John P. Blakeslee,[2] Chung-Pei Ma,[3] Peter A. Milne,[4] Peter J. Brown,[5] Michele Cantiello,[6] Peter M. Garnavich,[7] Jenny E. Greene,[8] John R. Lucey,[9] Anh Phan,[1] R. Brent Tully,[10] and Charlotte M. Wood[7]

[1]Department of Physics, Utah Valley University, 800 W. University Parkway, MS 179, Orem, UT 84058, USA
[2]Gemini Observatory and NSF's NOIRLab, 950 N. Cherry Ave., Tucson, AZ 85719, USA
[3]Department of Astronomy and Department of Physics, University of California, Berkeley, CA 94720, USA
[4]University of Arizona, Steward Observatory, 933 N. Cherry Avenue, Tucson, AZ 85721, USA
[5]George P. and Cynthia Woods Mitchell Institute for Fundamental Physics and Astronomy, Texas A&M University, College Station, TX 77843, USA
[6]INAF Osservatorio Astronomico d'Abruzzo, via Maggini, snc, 64100, Italy
[7]Department of Physics, University of Notre Dame, Notre Dame, IN 46556, USA
[8]Department of Astrophysical Sciences, Princeton University, Princeton, NJ 08544, USA
[9]Centre for Extragalactic Astronomy, University of Durham, Durham DH1 3LE, UK
[10]Institute for Astronomy, University of Hawaii, 2680 Woodlawn Dr., Honolulu, Hawaii, USA

ABSTRACT

We measured high-quality surface brightness fluctuation (SBF) distances for a sample of 63 massive early-type galaxies using the WFC3/IR camera on the Hubble Space Telescope. The median uncertainty on the SBF distance measurements is 0.085 mag, or 3.9% in distance. Achieving this precision at distances of 50 to 100 Mpc required significant improvements to the SBF calibration and data analysis procedures for WFC3/IR data. Forty-two of the galaxies are from the MASSIVE Galaxy Survey, a complete sample of massive galaxies within ∼100 Mpc; the SBF distances for these will be used to improve the estimates of the stellar and central supermassive black hole masses in these galaxies. Twenty-four of the galaxies are Type Ia supernova hosts, useful for calibrating SN Ia distances for early-type galaxies and exploring possible systematic trends in the peak luminosities. Our results demonstrate that the SBF method is a powerful and versatile technique for measuring distances to galaxies with evolved stellar populations out to 100 Mpc and constraining the local value of the Hubble constant.

1. INTRODUCTION

To understand the expansion history and contents of the universe, we must be able to measure accurate extragalactic distances with high precision and low systematic uncertainty well out into the Hubble flow. We have measured high-precision surface brightness fluctuation (SBF, Tonry & Schneider 1988) distances to 63 galaxies out to 100 Mpc to answer specific questions re-

lated to the most important issues in the extragalactic distance scale (e.g., Blakeslee et al. 2021; Verde et al. 2019; Cantiello et al. 2018). The SBF technique uses the Poisson statistics of discrete stars to determine the mean brightness of red giant branch (RGB) stars in a distant galaxy, even when such stars cannot be individually resolved (Tonry & Schneider 1988; Jensen et al. 1998; Blakeslee et al. 2009).

The SBF technique is particularly powerful for determining the distances to massive elliptical galaxies compared to other methods (Jensen et al. 2003; Blakeslee et al. 2009). It does not require the serendipitous discovery of a supernova explosion or assumptions about the relative velocities and distances of elliptical and spiral galaxies in a given group or galaxy cluster (Riess et al. 2021, for example). SBF reaches distances far greater than Cepheid variable stars or other techniques that de-

Corresponding author: Joseph B. Jensen
jjensen@uvu.edu

pend on resolving individual stars such as the tip of the red giant branch (Freedman et al. 2020, and references therein). It is also independent of the dynamics or mass of the target galaxy.

By measuring the power in the spatial Fourier power spectrum of an early-type galaxy (ETG) with globular clusters and background galaxies removed, we can determine the mean apparent luminosity of RGB stars in the galaxy statistically without having to measure them individually (Tonry & Schneider 1988; Jensen et al. 2003). The distance to the galaxy can then be computed using an empirical SBF calibration from which the absolute magnitude of the fluctuations has been determined as a function of the age and metallicity of the galaxy's stellar population (Jensen et al. 2003, 2015). Because RGB stars are very bright in the near-IR, the SBF signal at these wavelengths is very strong and measurable out to ∼100 Mpc with *HST* (Jensen et al. 2001) in modest exposure times. IR SBF with WFC3/IR has now been developed as a technique capable of achieving ∼5% distances out to 70 Mpc in a single *HST* orbit, as outlined by Jensen et al. (2015, hereafter J15) and demonstrated in a few individual cases (Cantiello et al. 2018; Nguyen et al. 2020; Liepold et al. 2020).

The IR SBF technique for *HST* WFC3/IR was calibrated by J15 using 16 galaxies in the Fornax and Virgo clusters with well-measured optical SBF distances. The optical SBF distances were taken from the large Advanced Camera for Surveys (ACS) Virgo and Fornax Cluster Surveys (ACSVCS and ACSFCS) (Mei et al. 2007; Blakeslee et al. 2009) based on Cepheid variable star distances to the Large Magellanic Cloud (LMC), as described below in Section 4. In this paper we describe additional improvements to the J15 procedures to further reduce the uncertainties of the SBF distance measurements, including (i) better measurements of the point-spread function (PSF); (ii) improved measurements of the instrumental background via reference to galaxy profiles from the 2MASS atlas images; (iii) more accurate measurements of the globular cluster and background galaxy luminosity functions; (iv) additional optical and IR color measurements from PanSTARRS, SDSS, and 2MASS for calibration of the absolute fluctuation magnitude; and (v) an updated distance to the LMC and Cepheid-derived SBF zero point. These improvements are described in detail below. We have now demonstrated the efficacy of the IR SBF methodology out to distances of 100 Mpc, taking advantage of the intrinsic IR brightness of the red giant branch stars that give rise to the fluctuations to reach much greater distances than achievable with optical SBF.

2. THE IR SBF SURVEY SAMPLE

There are two main subsamples in the current study. First, we observed 42 massive early-type galaxies in the MASSIVE sample (Ma et al. 2014) for the purpose of better constraining the relationship between black hole mass and the bulk dynamics of the galaxy. Galaxy evolution is linked to the growth of the central black hole in most galaxies, but the scatter in those relationships is often dominated by distance uncertainties. The second large subsample of this project was observed to explore how type Ia supernova luminosity correlates with galaxy mass or environment by measuring accurate distances to early-type SN host galaxies (Milne et al. 2015). The SN host distance measurements will help address the disagreement between values of the Hubble constant H_0 measured using SN Ia and Cepheids in spiral galaxies, and values inferred from the era of recombination (Riess et al. 2019; Planck Collaboration et al. 2020). Both of these topics are discussed in detail below. The target galaxies were all observed using WFC3/IR in the F110W filter for one or two orbits, sufficient for a precise distance measurement to 70 or 100 Mpc, respectively. The specific targets and programs are:

- GO-11711: NGC 4874 in the Coma cluster (PI J. Blakeslee).

- GO-12450: NGC 3504 (PI C. Kochanek), previously published by Nguyen et al. (2020).

- GO-14219: 35 early-type galaxies in the MASSIVE survey sample (PI J. Blakeslee).

- GO-14645: 19 type Ia SN early-type host galaxies (PI P. Milne).

- GO-15265: 6 additional distant MASSIVE sample galaxies (PI J. Blakeslee).

- GO-14771, GO-14804, and GO-15329: NGC 4993, host of the merging neutron stars detected through gravitational waves (PIs N. Tanvir, A. Levan, and E. Berger), previously published by Cantiello et al. (2018).

In addition to the galaxy distances from these programs, we also reprocessed the 16 Virgo and Fornax cluster galaxies used for the SBF calibration (GO-11712, PI J. Blakeslee), previously published by J15.

2.1. *The MASSIVE Survey*

The largest component (42/63) of our SBF distance database are the MASSIVE sample galaxies. MASSIVE is a volume-limited survey (Ma et al. 2014) of the ∼100 most massive ETGs within a distance of 108 Mpc in the

northern sky ($\delta > -6$ degrees). Within this volume, the sample is complete to an absolute K-band magnitude of $M_K = -25.3$ mag, or a stellar mass of $M_* \sim 10^{11.5}$ M$_\odot$, with no selection cuts on galaxy velocity dispersion, size, or environment. The MASSIVE survey goal is to obtain a comprehensive census of all the major constituents—luminous and dark—of local galaxies in the highest-mass regime. To achieve these goals, the MASSIVE team has acquired extensive data using optical integral-field spectrographs (IFS) on both sub-arcsecond and arc-minute scales, and obtained uniform measurements of spatially resolved stellar kinematics (Veale et al. 2017a,b, 2018; Ene et al. 2018, 2019, 2020), stellar populations (Greene et al. 2015, 2019) and ionized gas kinematics (Pandya et al. 2017). They also obtained radio and X-ray data to investigate the properties of cold molecular gas (Davis et al. 2016, 2019) and hot X-ray gas in these massive ETGs (Goulding et al. 2016; Voit et al. 2018).

Using the homogeneous set of sub-arcsecond and wide-field IFS and photometric data as constraints, the MASSIVE collaboration is performing dynamical mass modeling of the supermassive black holes (SMBH), stars, and dark matter components for a sample of MASSIVE galaxies (Liepold et al. 2020; Quenneville et al. 2020). Accurate and precise distances are essential to measuring the most fundamental properties of massive ETGs and their central black holes, including their masses. The largest ETGs contain the most massive black holes (BHs), the most extreme stellar initial mass functions (IMFs, Cappellari et al. 2012; van Dokkum & Conroy 2010), and the most dramatic size evolution over cosmic time (e.g., Collins et al. 2009; De Lucia & Blaizot 2007). The primary goals of MASSIVE include precisely constraining the SMBH-galaxy scaling relations, the stellar IMF, and the late-time assembly histories of elliptical galaxies.

The purpose of the current study with respect to MASSIVE is to use high-resolution F110W (1.1 μm) infrared images to determine high-precision SBF distances (Tonry & Schneider 1988) for all galaxies in the MASSIVE sample within 70 Mpc for which SBF distances were not previously available. Accurate SBF distances are needed to remove potentially large errors from peculiar velocities, especially in the high-density galaxy cluster regions typically occupied by massive ETGs, or systematic errors from heterogeneous distance measurement methods that would otherwise be used to determine the SMBH-galaxy mass scaling relations. Distance errors affect BH masses and galaxy properties in dis-

similar ways, and thus can bias both the *scatter* and *slopes* of the scaling relations. The measured distances and central profiles will be used to constrain the stellar, dark matter, and BH masses to high precision, giving unprecedented insight into the formation and evolution of the most massive galaxies in the local universe.

The IR SBF distance technique was recently used to measure the stellar dynamical mass of the SMBH in NGC 1453, one of the MASSIVE targets in the current SBF sample (Liepold et al. 2020); the 5% SBF distance from this study reported therein was instrumental to the interpretation of the SMBH mass being consistent with the mass and galaxy scaling relations in the potential of that galaxy. Another recent MASSIVE study by Goullaud et al. (2018) used the high-resolution WFC3/IR F110W images from this study to determine the central luminosity profiles of 35 MASSIVE galaxies, greatly reducing the degeneracy between M/L and BH masses in dynamical orbit modeling. Another example of how SBF distances can help constrain BH masses even in some later-type galaxies is the recent molecular gas dynamical measurement by Nguyen et al. (2020) using the SBF technique to determine the distance and BH mass in NGC 3504. Prior to the SBF measurement, the best Tully Fisher distance to NGC 3504 was 13.6 Mpc (Russell 2002), which is more than a factor of two smaller than the SBF distance. Using the shorter distance would have led to a significant difference in the derived BH mass.

2.2. *Type Ia Supernovae*

The SBF distance database also includes 24 Type Ia supernova (SN) host galaxies (five of which are also MASSIVE galaxies). These galaxies were observed to better understand the consistency of SN Ia luminosity as a function of galaxy type and environment. SN Ia are one of the highest-precision distance indicators for cosmology and have been used to measure the Hubble constant (Riess et al. 2021; Freedman et al. 2020; Khetan et al. 2021; Beaton et al. 2018). Precise and accurate distance measurements are critical to resolving the discrepancy between local values of H_0 and those inferred from high-redshift cosmic microwave background radiation measurements (Riess et al. 2019; Planck Collaboration et al. 2020). Resolving this discrepancy could reveal systematic errors in the distance measurements, provide new insight into the physics of the early universe, or both.

Table 1. WFC3/IR F110W SBF Observation and Morphology Data

Galaxy	HST Program		$t_{\exp}$	Extinction	Background	Type	Notes
	ID	sample	(s)	(mag)	$(\mathrm{e^{-}s^{-1}pix^{-1}})$	T	
(1)	(2)	(3)	(4)	(5)	(6)	(7)	(8)
IC 2597	14654	SN	2496	0.062	0.88 ± 0.12	-3.9	
NGC 0057	14219	M	2496	0.068	1.28 ± 0.08	-4.9	
NGC 0315	14219	M	2496	0.057	1.20 ± 0.23	-4.1	ND
NGC 0383	14219	M	2496	0.062	0.88 ± 0.11	-2.9	C
NGC 0410	14219	M	2496	0.052	1.80 ± 0.07	-4.3	Sh
NGC 0495	14654	SN	2496	0.063	1.00 ± 0.40	$+0.2$	SB
NGC 0507	14219	M	2496	0.055	1.80 ± 0.16	-3.3	Sh, C
NGC 0524	14654	SN	2496	0.073	1.60 ± 0.40	-1.2	Sh, ND
NGC 0533	14219	M	2496	0.027	1.76 ± 0.08	-4.9	
NGC 0545	14219	M	2496	0.036	1.44 ± 0.06	-2.9	C
NGC 0547	14219	M	2496	0.036	1.59 ± 0.06	-4.8	C
NGC 0665	14219	M	2496	0.078	1.28 ± 0.08	-2.0	SB, D
NGC 0708	14219	M	2496	0.079	1.36 ± 0.08	-4.9	ND, C
NGC 0741	14219	M	2496	0.046	1.28 ± 0.12	-4.8	C
NGC 0777	14219	M	2496	0.041	1.44 ± 0.08	-4.8	
NGC 0809	14654	SN	2496	0.021	1.40 ± 0.04	-1.8	R
NGC 0890	14219	M,SN	2496	0.068	1.88 ± 0.20	-2.6	
NGC 0910	14654	SN	5293	0.051	1.42 ± 0.06	-4.1	
NGC 1016	14219	M	2496	0.027	1.32 ± 0.14	-4.9	
NGC 1060	14219	M	2496	0.171	1.56 ± 0.15	-3.0	
NGC 1129	14219	M	2496	0.099	1.56 ± 0.09	-4.9	C
NGC 1167	14219	M	2496	0.160	1.60 ± 0.08	-2.4	Sp, D
NGC 1200	14654	SN	2496	0.064	1.24 ± 0.08	-2.9	
NGC 1201	14654	SN	1997	0.014	1.30 ± 0.15	-2.6	
NGC 1259	14654	SN	5293	0.140	1.34 ± 0.04	-3.0	
NGC 1272	14219	M,SN	2496	0.142	1.16 ± 0.04	-4.0	C
NGC 1278	14654	SN	2496	0.145	1.40 ± 0.12	-4.8	C
NGC 1453	14219	M	2496	0.093	1.74 ± 0.16	-4.7	
NGC 1573	14219	M	2496	0.121	3.00 ± 0.14	-4.8	
NGC 1600	14219	M	2496	0.038	1.60 ± 0.19	-4.6	
NGC 1684	14219	M	2496	0.051	1.56 ± 0.08	-3.9	ND
NGC 1700	14219	M	2496	0.038	1.44 ± 0.18	-4.7	
NGC 2258	14219	M,SN	2496	0.113	2.08 ± 0.12	-2.0	C
NGC 2274	14219	M	2496	0.092	1.56 ± 0.19	-4.8	
NGC 2340	15265	M	2812	0.065	1.32 ± 0.36	-4.8	Sh
NGC 2513	14219	M	2496	0.020	2.00 ± 0.06	-4.9	
NGC 2672	14219	M	2496	0.019	1.64 ± 0.19	-4.8	C
NGC 2693	14219	M	2496	0.017	1.40 ± 0.26	-4.8	C
NGC 2765	14654	SN	2496	0.028	1.92 ± 0.20	-1.9	R
NGC 2962	14654	SN	2496	0.051	1.76 ± 0.08	-1.1	R
NGC 3158	15265	M,SN	2612	0.012	1.26 ± 0.19	-4.8	
NGC 3392	14654	SN	2695	0.012	1.16 ± 0.04	-3.7	ND
NGC 3504	12450		1398	0.023	1.64 ± 0.14	$+2.1$	Sp, D
NGC 3842	15265	M	2612	0.019	1.34 ± 0.19	-4.9	C

Table 1 *continued*

Table 1 *(continued)*

Galaxy	HST Program		$t_{\exp}$	Extinction	Background	Type	Notes
	ID	sample	(s)	(mag)	$(\mathrm{e^- s^{-1} pix^{-1}})$	T	
(1)	(2)	(3)	(4)	(5)	(6)	(7)	(8)
NGC 4036	14654	SN	2695	0.021	1.63 ± 0.19	-2.5	R
NGC 4073	15265	M	2612	0.024	2.53 ± 0.19	-4.1	
NGC 4386	14654	SN	2695	0.034	1.22 ± 0.19	-2.0	R
NGC 4839	15265	M	2612	0.009	1.34 ± 0.19	-3.9	C
NGC 4874	11711	M	4794	0.008	1.56 ± 0.10	-3.6	C
NGC 4914	14219	M	2496	0.012	0.92 ± 0.08	-4.0	
NGC 4993	14771+14804	BNS	893	0.109	4.38^a	-3.0	Sh, D
	15329		1012		4.00^a		
NGC 5322	14219	M	2496	0.012	1.60 ± 0.20	-4.8	
NGC 5353	14219	M,SN	2496	0.011	1.32 ± 0.21	-2.0	R, C
NGC 5490	14654	SN	2496	0.024	0.92 ± 0.16	-4.9	
NGC 5557	14219	M	2496	0.011	1.16 ± 0.08	-4.8	
NGC 5839	14654	SN	2496	0.046	1.64 ± 0.08	-2.0	Sp, R
NGC 6482	14219	M	2496	0.089	0.88 ± 0.04	-4.9	
NGC 6702	14654	SN	2496	0.094	0.84 ± 0.08	-4.9	ND
NGC 6964	14654	SN	2496	0.087	1.76 ± 0.08	-4.5	
NGC 7052	14219	M	2496	0.108	0.88 ± 0.28	-4.9	
NGC 7242	15265	M	2612	0.133	1.38 ± 0.19	-4.0	C
NGC 7619	14219	M	2496	0.072	1.56 ± 0.06	-4.8	
ESO125-G006	14654	SN	5293	0.200	1.06 ± 0.06	-3.5	Sh

[a]The elevated background for the NGC 4993 observations resulted from the unusually small solar angle required to observe this galaxy during the period when the kilonova optical afterglow was still visible (Cantiello et al. 2018).

Column notes: (1) Galaxy name; (2) HST Program ID; (3) SBF sub-sample: M=MASSIVE, SN=supernova host, BNS=binary neutron star merger; (4) Exposure time; (5) F110W extinction from Schlafly & Finkbeiner (2011) retrieved from NED; (6) F110W instrumental background; (7) Galaxy T-type from the HyperLEDA database (Makarov et al. 2014), where $T < -3$ are elliptical galaxies, $-3 < T < 0$ are S0 galaxies, and spirals have $T > 0$; (8) Morphology notes: C=bright companions, D=dust, ND=nuclear dust, Sh=dynamical shells or arcs, Sp=spiral structure, SB=Barred spiral, R=rings and other residual disk galaxy subtraction artifacts, such as from edge-on disks or boxy structures.

There are several motivations for measuring distances to SN Ia in early-type hosts. The width of SN Ia light curves is correlated with host galaxy type, with slowly-declining, bright SN Ia typically found in late-type hosts while fast-declining, subluminous SN Ia are often found in early-type hosts (Hamuy et al. 1995). While light curve fitting techniques that correct for decline rate do not show significant residuals with host type, there is clear evidence that host galaxy properties have a systematic effect on SN Ia H_0 residuals (e.g., Lampeitl et al. 2010). SN Ia luminosities are typically calibrated using distances derived from Cepheids, which are found in young stellar populations in star-forming spiral galaxies. However, SN Ia in the Hubble flow occur in a wide range of galaxy types and local environments. Rigault et al.

(2020, 2015) found that H_0 can be biased up to $\sim 5\%$ if the SN in the Hubble flow are preferentially located in older stellar populations than those used for Cepheid calibration; the effect is smaller with different sample selection cuts (Jones et al. 2018). There are also differences in SN Ia properties between passively and actively star-forming hosts (e.g., Sullivan et al. 2010; Kang et al. 2016). In addition, Milne et al. (2013) discovered two previously unrecognized sub-populations of normal SN Ia, one of which preferentially occurs in early-type hosts. Therefore an independent determination of SN Ia distances in early-type hosts is important to understanding the luminosity variations arising from host galaxy type.

It is currently unclear if all faint, fast-declining SN Ia, which are most common in early-type hosts, can be de-

scribed along a continuum from normal SN Ia to an extreme of faint 1991bg-like SN Ia or if the faint events represent an entirely separate class (Kattner et al. 2012; Burns et al. 2014; Dhawan et al. 2017). This sample of 24 distance measurements to early-type SN host galaxies is an important step towards understanding the role of galaxy type in the SN distance scale.

One published example of how IR SBF has been used to better understand the properties of a stellar explosion is the 2017 binary neutron star merger in NGC 4993 that was first observed as a gravitational wave event. Cantiello et al. (2018) used WFC3/IR SBF measurements to provide the highest precision distance measurement of the galaxy to-date, which provided a better constraint on the viewing angle with respect to the rotation axis of the merging binary pair and the orientation of its relativistic jets.

The following section describes in detail the procedures used to make the SBF distance measurements to the galaxies reported in this study. Section 4 discusses the SBF calibration zero point. Section 5 contains transformations for galaxy colors, which are needed to correct fluctuation magnitudes for population effects and compute distances. Uncertainties are discussed in Section 6 and the SBF distances are presented in Section 7. Alternative calibrations and methods for determining SBF distances using other photometric systems are included in the Appendix.

3. SBF ANALYSIS PROCEDURES FOR WFC3/IR

The SBF method for measuring extragalactic distances was first described by Tonry & Schneider (1988) and the basic procedures as applied in the infrared were outlined by Jensen et al. (1998, 2001, 2003). J15 provided the calibration and procedures for WFC3/IR, which are updated below.

3.1. *Initial Pipeline Processing and Analysis*

The basic image processing steps followed those described in detail by J15 with a few modifications to improve reliability and reduce uncertainties. The first step in the SBF data reduction process was to produce a combined, cleaned, background-subtracted image. To avoid correlated noise between pixels, which leads to a variable noise component in the spatial power spectrum, we chose to perform the SBF analysis using the native WFC3/IR pixels and integer pixel shifts when combining, even though doing so results in a ∼10% difference between the x and y plate scales (due to the focal plane distortion from the WFC3/IR optics). We used the raw images from the *HST* archive without the geometric correction usually applied using *astrodrizzle*. Processed images are shown in Figure 1. The uncorrected images

were used in all subsequent SBF analysis steps except when comparing galaxy surface brightness profiles with other survey images.

Approximately 40% of the F110W images in our study were affected by the diffuse upper-atmosphere helium emission line at 1.083 μm (Brammer et al. 2014). During each MULTIACCUM exposure,[1] multiple reads of the detector allowed us to determine the signal in each pixel at multiple points during each exposure, and therefore identify pixels that were affected by saturation or cosmic rays, which can be identified as a break in the count rate of electrons being detected in a pixel. The He emission, which appears as a flickering variable background, also causes the signal rate to change during a MULTIACCUM exposure. Gabriel Brammer at STScI has written a specialized Python program to correct for variable backgrounds and events like satellite passages in MULTIACCUM sequences that affect the flux slope in a large number of pixels at once.[2] The correction algorithm compares the count rate over a large region of the detector in the first and last reads of a MULTIACCUM sequence, and then flattens the sequence of reads so that each individual subframe has the same average background count rate. We used this algorithm to identify individual subframes that had varying background and re-processed all images to have flattened (linear) background count rates. The new *flt* files were then combined using integer pixel offsets to produce the final images used for SBF analysis.

3.2. *Background Determination and Subtraction*

The next step in the SBF procedure was to determine the correct residual background level. The fluctuation power must be normalized by the mean galaxy brightness at a particular location, so any uncertainty in the background level affects the SBF amplitude measurement and its uncertainty. Measuring the background level was an iterative process that included several different complementary methods, most of which are described in detail by Goullaud et al. (2018) and summarized here.

We started with an estimate of the maximum possible sky value by measuring the mean level in the corners of the image, and then used $r^{1/4}$ galaxy fits to make a more realistic estimate of the residual galaxy flux in the corners. We made an elliptical model of each galaxy using the ELLIPROF routine (Tonry et al. 1997; Jordán et al. 2004) by determining the surface brightness in an-

---

[1] See https://www.stsci.edu/hst/instrumentation/wfc3 for a description of the WFC3/IR readout modes.

[2] https://github.com/gbrammer/wfc3

nuli that were allowed to vary in ellipticity, position, and orientation. The galaxy model is also a key ingredient in the SBF measurement, since the fluctuations are normalized by the galaxy surface brightness model. The surface brightness profiles from the elliptical fits were compared to $r^{1/4}$ profiles to determine the likely residual background level. Several galaxies have bright neighbor galaxies in the WFC3/IR field of view that also had to be removed by iteratively fitting and subtracting elliptical models for each galaxy one at a time, and masking all other compact galaxies and point sources.

Many of the galaxies do not follow a $r^{1/4}$ profile, so an improved sky estimate was determined by matching the F110W surface brightness profiles (in their geometrically-corrected forms from the HST pipeline for consistent comparison) to the 2MASS J-band radial profiles (Jarrett 2000). The 2MASS profiles were measured in elliptical annuli after subtracting the sky background level measured well away from the galaxies, much farther than possible in the limited field of view of the WFC3/IR frames (the MASSIVE sample galaxies extend well beyond the edges of the WFC3/IR field of view, making direct sky estimation difficult). The F110W profiles generally agree very well with the 2MASS profiles; in some cases they disagreed due to the presence of companions or other morphological oddities. Adjustments to the background estimates were made to improve agreement with 2MASS profiles, and the results were published by Goullaud et al. (2018).

To ensure the best possible SBF measurements, the background levels reported by Goullaud et al. (2018) were revised to take into account the radial behavior of the SBF signal. The SBF amplitude depends on distance and stellar population. Making the justifiable assumption that all the stars in the galaxy are at the same distance and that any trend in stellar population age or metallicity with radius is revealed by a $(g-z)$ color gradient (if any), we refined the background levels from Goullaud et al. (2018) to minimize the scatter between the radial regions in which the SBF amplitude was measured. The updated background levels are listed in Table 1. The background subtraction uncertainties for the MASSIVE galaxies were taken from Goullaud et al. (2018) and computed for the rest of the galaxies using the technique therein. The average F110W background level for these data, revised as described above and excluding NGC 4993, is 1.50 $\mathrm{e^- s^{-1}}$, with a minimum of 0.88 and maximum of 3.0 $\mathrm{e^- s^{-1}}$ (the NGC 4993 observations were scheduled with an unusually small solar angle to observe the fading optical afterglow of the merging neutron star hypernova explosion). This corresponds to an average surface brightness of 21.95 mag $\mathrm{arcsec^{-2}}$

and a range of 21.16 to 22.50 mag $\mathrm{arcsec^{-2}}$. The mean background level reported by Goullaud et al. (2018) was 1.78 $\mathrm{e^- s^{-1}\,pix^{-1}}$, or 21.77 AB mag $\mathrm{arcsec^{-2}}$. These values are also consistent with the HST published values for the F110W background (Pirzkal 2014) and the mean background level of 1.3 $\mathrm{e^-\ s^{-1}\ pix^{-1}}$ measured by J15, given the standard deviation of 0.4 $\mathrm{e^- s^{-1} pix^{-1}}$ between individual observations.

3.3. *Creating a Smooth Galaxy Model*

After background subtraction, each galaxy in our sample was fitted using the ELLIPROF isophotal fitting routine a second time. To get the best possible fits for the galaxies with bright companions, we computed the fit to each of the galaxies iteratively and independently, starting at smaller radii and progressing to larger distances from the center, removing companions by degrees and carefully masking other compact objects. The iterations yielded clean fits to most of the galaxies. The smooth galaxy models were used to plot $r^{1/4}$ profiles, check for residual non-zero background levels, and saved for later use to normalize the SBF power spectrum. In a few cases, neighboring galaxies, central dust lanes, shell structure, and spiral structure or bars left significant residual patterns after fitting and removing the elliptical profile, which we removed using a spline fitting routine on a grid with 8 to 16 nodes in each pixel dimension. This residual fit procedure usually cleaned up the residuals, but we avoided fitting the SBF spatial power spectrum in regions with persistent residuals and for wavenumbers less than 25 to 30 $\mathrm{pix^{-1}}$ because the residual fit artificially suppresses power at these scales. For such galaxies, a fit to the lower wavenumbers in the power spectrum would not have been possible anyway.

3.4. *Measuring the Point-Spread Function*

Another ingredient needed for SBF measurement is an accurate representation of the point-spread function (PSF) for the geometrically-uncorrected WFC3/IR F110W images. The spatial Fourier power spectrum is a convolution of the pixel-to-pixel stellar Poisson variations with the PSF plus a white noise component resulting from the background flux and detector readout noise. The SBF signal, in the absence of instrumental blurring, would simply be the Poisson variance between pixels due to the varying number of stars per pixel. The real images are blurred by the instrumental PSF, however, so the SBF signal is the sum of the white noise component and the SBF signal convolved with the PSF. Accurately fitting the SBF spatial power spectrum therefore requires a very high S/N measurement of the PSF.

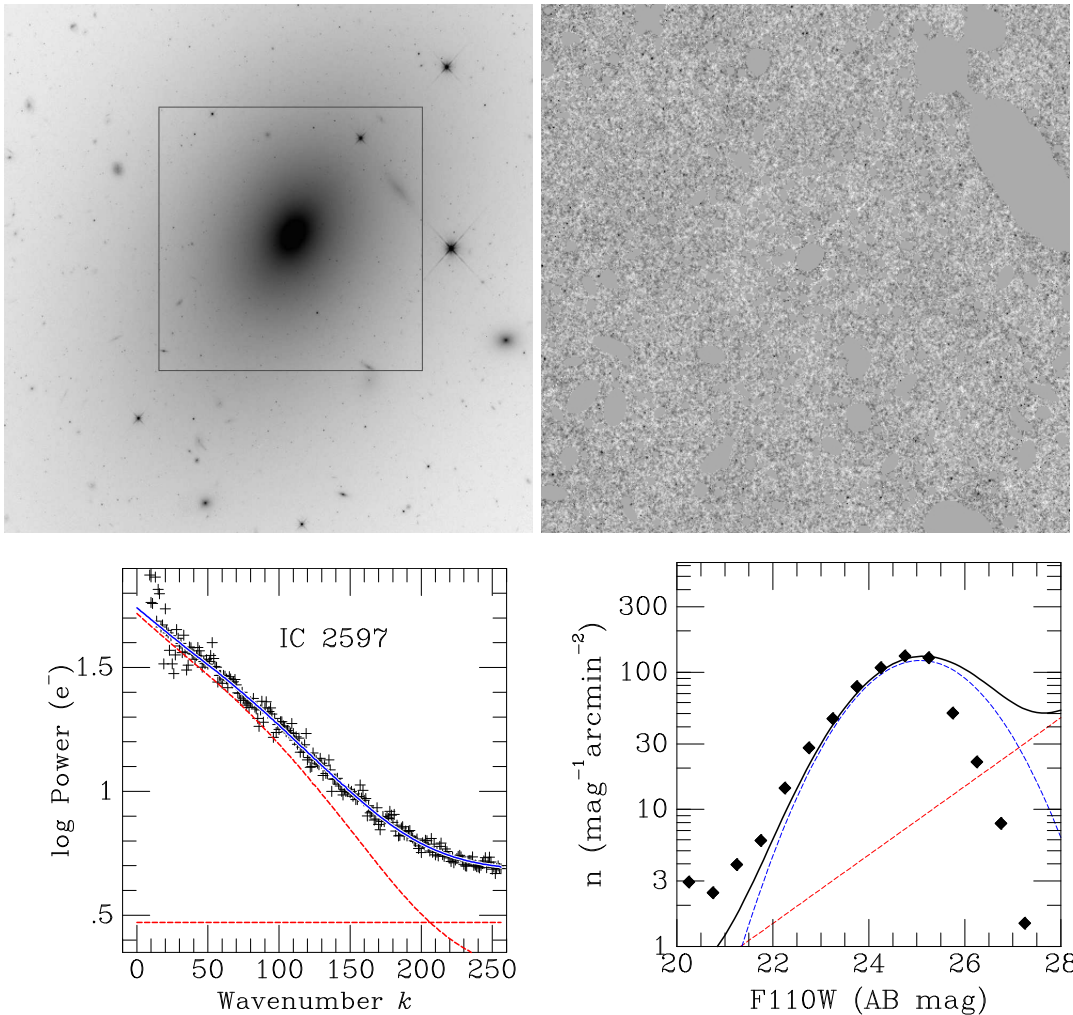A library of reference PSF star images was compiled by extracting the best clean, bright point sources

Figure 1. Combined figure for IC 2597. The upper left image is the full field of view (127 arcsec on a side). The upper right image shows the central 63×63 arcsec region (the region in the box in the left image) with the smooth galaxy model subtracted, scaled by the square root of the galaxy model, and with globular clusters and background galaxies masked. The lower left plot is the spatial power spectrum (crosses) in units of total electrons detected in the full exposure fitted to the scaled expectation power spectrum $P_0 \times E(k)$ and white noise floor P_1 (red dashed lines). The solid blue line is the sum of the two, fitted to the residual power spectrum. The lower right panel shows the fit to the GCLF (Gaussian, blue dashed line) and background galaxy luminosity function (power law, red dashed line) used to estimate the P_r contribution from undetected sources. The black solid line is the sum of the two luminosity functions as fitted to the points. The diamond points in the lower right panel include both globular clusters and background galaxies. This is the first of the set of 61 figures available in the online version of the paper. All the galaxy images use the same logarithmic stretch and limiting values; the residual images are plotted with linear stretch and the same upper and lower limits. The closer galaxies show larger amplitude fluctuations. Comparable images and power spectra for NGC 3504 and NGC 4993 have already been published by Nguyen et al. (2020) and Cantiello et al. (2018).

(Galactic foreground stars) from the residual images of a dozen galaxies (with background and galaxy removed). We also extracted many more intermediate brightness stars and combined the best-centered ones to construct additional composite PSF references. The extracted PSFs were used to compute the fluctuation magnitudes for many different galaxies, compared to each other, and compared to the composite PSFs selected for their individual centering. This provided a library of 12 individual PSF stars and several composite PSFs from four

different *HST* programs. During the creation of the PSF library, we were careful to choose stars within approximately 100 pixels of the vertical location of the center of the galaxy, where the geometrical distortion is $\lesssim 1\%$ and the resulting PSF normalization is less subject to the pixel scale variation in WFC3/IR. The central region is also the area on the detector where the highest-S/N SBF measurements are made. In the final error analysis we used all the PSF stars to measure each galaxy, determined the best-fitting PSFs, and used the standard

deviation of the full set of more than a dozen individual and combined PSFs to determine the PSF-fitting uncertainty.

This new library of PSF stars yielded much more reliable and consistent SBF measurements than the limited set of fainter stars used for the original WFC3 calibration (J15), which allowed us to reduce the uncertainty due to PSF normalization from ∼0.05 mag in the J15 study to 0.015 mag for the current study, with a systematic offset of ∼0.05 mag compared to J15, as described by Cantiello et al. (2018). We also compared the empirical PSFs to Tiny Tim models (Krist et al. 2011);[3] the latter were symmetrical, unlike the PSFs extracted from the uncorrected images, but with modest Gaussian softening they still matched the SBF measurements reasonably well. A quantitative analysis of the PSF fits is presented below in the analysis of the uncertainties.

3.5. *Residual Power from Undetected Globular Clusters and Background Galaxies*

In addition to the stellar SBF component, the spatial Fourier power spectrum has a contribution from globular clusters (GC) and background galaxies superimposed on it, which can be the dominant source of uncertainty at large distances. The established procedure for removing their contribution to the spatial power spectrum requires fitting a Gaussian luminosity function to the GC population and a power law luminosity function to the background galaxies that *can* be detected, and then integrating those functions beyond the photometric completeness limit to estimate the residual contribution from fainter undetected objects (see Figure 1).

At distances beyond 50 Mpc, like the majority of the galaxies in this study, even when the SBF signal is still easy to detect, the point source sensitivity and resulting GC and galaxy luminosity function fits are usually the limiting factor in measuring accurate SBF distances. For giant elliptical galaxies that have significant populations of GCs, it is very important to measure as much of the globular cluster luminosity function (GCLF) as possible, determine the photometric completeness limit, and correct the SBF signal for the undetected objects beyond the completeness limit. In most cases, the GCLF can be measured well enough by reaching within 0.5 mag of the peak of the GCLF. We found that when this sensitivity limit was reached, the contribution to the SBF signal from unmasked, undetected objects is less than ∼10%, and the uncertainty in the correction was low enough (see Section 6) that the resulting SBF distance

[3] http://tinytim.stsci.edu/cgi-bin/tinytimweb.cgi

is good to 5% out to 70 Mpc in a single orbit, and to 10% out to ∼100 Mpc in one orbit.

To test the robustness of the GCLF and background galaxy luminosity function measurements, we compared two different photometry programs. We used SExtractor (Bertin & Arnouts 1996), which uses a combination of aperture photometry and elliptical model fits for point sources and extended sources, respectively, and an updated version of DoPHOT (Schechter et al. 1993) modified by J. Alonso-Garcia (Alonso-García et al. 2012), to determine magnitudes using PSF-fitting of identified objects. To ensure that the photometric performance of the two programs was consistent for point sources of the appropriate brightness (i.e., near the peak of the GCLF for galaxies from 50 to 100 Mpc), we made detailed comparisons using the F110W and F160W observations of the GC population around NGC 4874 (GO-11711), which were deeper than most of the other observations in this study (two orbits at F110W). We compared our SExtractor aperture magnitudes to those from Cho et al. (2016) to determine the aperture correction for the PSF-fit magnitudes from DoPHOT: the aperture correction Cho et al. used for F160W was −0.259 mag for 0.6 arcsec diameter apertures, and we found that the same correction worked well for F110W. As expected, the agreement between Cho's and our independent analyses of the F110W data using the same data and same photometry package was excellent. We then used the SExtractor results to determine the aperture corrections for the PSF-fit magnitudes from DoPHOT. Because DoPHOT determines the magnitude in a smaller region near the core of the PSF, the aperture corrections were larger (−0.539 mag at F110W), with a small additional correction for objects fainter than 24 mag AB.

For the purpose of finding objects superimposed on a bright galaxy, we started by removing a smooth fit to all the large galaxies in the field of view and masking bright foreground stars. The resulting residual images do not have uniform noise because of the galaxy subtraction, and so a variance map was created and used with both SExtractor and DoPHOT to prevent them from identifying spurious objects near the galaxy center, or, alternatively, from missing objects farther away where galaxy subtraction noise was not significant. As in past SBF studies, we added an additional component (the galaxy model scaled by a constant) to the variance map to prevent SExtractor and DoPHOT from detecting the surface brightness fluctuations themselves as point sources. The empirically-determined scale factor we used with SExtractor is ∼7 at 20 Mpc and decreases to 1.5 times the mean galaxy surface brightness at distances of 70 Mpc and beyond (c.f. Jordán et al. 2004); the factor

used with DoPHOT was typically twice as large since DoPHOT is capable of detecting fainter compact objects near the center of the galaxy than SExtractor.

While both SExtractor and DoPHOT were successful at detecting and measuring faint point sources, SExtractor did a better job at measuring the faint *extended* objects (primarily background galaxies) that abound in deep *HST* images. DoPHOT, on the other hand, did a better job measuring faint point sources (mostly GCs), particularly near the centers of the galaxies. The PSF fitting procedure used by DoPHOT would often interpret faint extended objects as multiple faint point sources, however. DoPHOT therefore finds significantly more faint objects than SExtractor and fewer brighter ones, as expected if the flux from one extended object is divided among many fainter ones.

To get the best possible measurements of both the GC and background galaxy populations, we adopted a hybrid approach for this study that utilized the strengths of both systems. The extended objects (those with SExtractor CLASS_STAR < 0.7) were extracted from the SExtractor output catalog and used to make a mask of those objects, and the extended object mask was applied to the DoPHOT input image to remove faint galaxies and isolate the point sources. DoPHOT was then used to photometer the point sources using PSF-fitting, and the output catalog was then merged with the SExtractor extended source catalog. The result was generally an excellent fit to both the GC and background galaxy luminosity functions, with a fainter limiting cutoff magnitude that avoided the contamination caused by extended objects being broken up into many smaller ones. Individual and combined GCLF and galaxy luminosity function fits are shown in Fig. 1. The separate independent catalogs were also retained to help identify problematic regions or fits, as described below.

Using the merged SExtractor+DoPHOT photometric catalog, the contribution to the total SBF signal from undetected globular clusters and galaxies was determined by fitting the GCLF assuming a Gaussian width of 1.2 to 1.4 mag, appropriate for giant ellipticals and early-type galaxies with rich GC populations. The GCLF was shifted to the distance of each galaxy by adopting an absolute peak magnitude of $M_J = -9.18$ (Nantais et al. 2006). An initial first guess at the distance was used to get an approximate SBF distance, which was then used to make a more precise GCLF fit, followed by the final SBF distance measurement. (The SBF distance measurement process was done blindly until this second iteration where the distance was needed to constrain the GCLF peak brightness.) The background galaxy population was assumed to follow a power-law

distribution with a slope of 0.25 and normalized at the faint end to match the GOODs and HUDF surveys (Retzlaff et al. 2010; Windhorst et al. 2011). The two luminosity functions (galaxies and GC) were then combined and integrated beyond the photometric completeness limit, typically ∼25 AB mag for single-orbit F110W measurements, to determine how much the undetected sources contribute to the stellar SBF signal (P_r). The correction to the SBF signal was typically largest nearer the centers of the galaxies, where the median was 9% of the total SBF signal (P_0), and smaller in the outer regions (∼5%) where GC were less numerous and the completeness limit was fainter. For the most distant galaxies in our sample (80 to 100 Mpc), values were 25% of the total SBF power P_0 near the center and 10% in the outer regions. The uncertainty in this correction, as measured by repeating the SBF analysis using a variety of plausible fit parameters and cutoff limits, is shown in Table 2, and was determined by taking half the difference between the correction determined using SExtractor and DoPHOT and combining in quadrature with 25% of the fractional correction (P_r/P_0). The separate GCLF and galaxy luminosity function fits are shown in the lower right panels of the combined figure set (see Fig. 1).

The calibration galaxies from J15 were near enough that the corrections for undetected GCs and background galaxies were negligible (<1%). For galaxies beyond 50 Mpc, the power in undetected sources is a strong function of both distance and position relative to the center of the galaxy. Near the center, the galaxy brightness prevents detection of the faint sources near the peak of the GCLF. Because fewer sources are detected, the GCLF fit is less reliable. The regions farther from the center are better for detecting GCs and galaxies, but the lower galaxy surface brightness makes detection of the SBF signal less reliable. To balance the two sources of uncertainty (correction and background subtraction), we optimized both by measuring the radial behavior of the stellar SBF signal and the residual source correction in a series of radial annuli as described below.

3.6. *Fluctuation Magnitudes*

The SBF fluctuation power P_0 was determined by fitting the measured two-dimensional Fourier spatial power spectrum of the residual image $P(k)$, normalized by the mean galaxy brightness, with expectation power spectrum $E(k)$, the normalized power spectrum of the PSF reference star convolved with the mask window function:

$$P(k) = P_0 \times E(k) + P_1 \qquad (1)$$

where the scale factor P_0 is the SBF signal and is the white noise component. As long as the noise between

pixels is uncorrelated, which is true for images combined using integer pixel shifts to avoid pixel interpolation, the term is constant with wavenumber k. P_0 has units of flux (total electrons detected), which is converted to an apparent "fluctuation magnitude"

$$\overline{m}_{110} = -2.5 \log(P_0 - P_r) + 26.8223 - A_{110} \quad (2)$$

where is the correction for the contribution from undetected GC and background galaxies and A_{110} is the foreground extinction in the F110W bandpass from Schlafly & Finkbeiner (2011) and adapted for F110W using the NASA Extragalactic Database extinction lists (Table 1).

We measured the fluctuations independently in four radial annuli spanning 32–64, 64–128, 128–256, and 256–512 pixels. Fitting the power spectrum to get a reliable value for $\overline{m}_{110}$ is a trade-off between stronger S/N near the center where the galaxy is brightest, but the number of pixels is smaller and the contribution from is larger, and the regions farther out, where the galaxy surface brightness is lower relative to the background, and is therefore subject to larger background variations. The four annular regions were treated independently. We measured the fluctuation magnitudes in each annulus individually, and then combined the final results into a single distance measurement for each galaxy by taking the uncertainty-weighted average of the good regions.

Annuli were excluded from the average for a variety of reasons. Some were affected by nearby bright companion galaxies, dust lanes, shells, or other galaxy fitting defects that rendered the fluctuation measurements unreliable. We also excluded from the weighted average any region of the galaxy where the total $\overline{m}_{110}$ uncertainty was greater than 0.15 mag (roughly twice the average uncertainty). A region was also excluded when the difference between the independent SExtractor and DoPHOT fits exceeded 0.15 mag. The final distance measurement made use of the hybrid SExtractor and DoPHOT photometry only when the two were independently consistent within 0.15 mag. We also required that the photometric completeness limit for point sources be no more than 0.5 mag brighter than the GCLF peak. When the photometry does not go deep enough to catch most of the GCs close to the peak of the GCLF, the correction becomes unreliable and $\overline{m}_{110}$ is potentially biased. The central annulus was the most likely to be excluded because point sources become increasingly difficult to detect when superimposed on the bright galaxy profile. Other exclusions included annuli where the fraction of masked pixels in the annulus was greater than 50%, the background level exceeded the galaxy surface brightness, or the SBF $S/N = (P_0 - P_r)/P_1 < 5$. These latter conservative criteria have been established

through experience with WFC3/IR SBF measurements (J15).

Some of the galaxies in this sample are lenticular and their projected shapes are very elongated or disky. If these galaxies have population gradients, then using elliptical annuli instead of circular ones could produce more consistent distances. To check this possibility, we repeated the $\overline{m}_{110}$ measurements for a subsample of 14 galaxies using elliptical annuli that were completely contained within the original (default) circular annuli to prevent cross-talk (Phan & Jensen 2020). Seven galaxies were highly elongated and seven were nearly round. Eight of the galaxies showed less than 0.01 mag differences between elliptical and circular annuli, and included some of the most elongated galaxies in our entire sample (including NGC 2765 and NGC 4036, for example). All but one galaxy differed by less than 0.03 mag, and the only exception was NGC 495, a barred S0 galaxy where neither elliptical nor circular apertures match the light distribution well. Given that the differences were significantly less than the individual annular uncertainties in $\overline{m}_{110}$, we did not repeat the $\overline{m}_{110}$ measurements using elliptical annuli for the rest of the sample. This result is consistent with similar tests done using optical I-band SBF measurements (Cantiello et al. 2011).

4. CALIBRATION OF SBF DISTANCES

Determining the distance to a galaxy using the apparent fluctuation magnitude $\overline{m}_{110}$ requires knowledge of the absolute magnitude $\overline{M}_{110}$, which was determined empirically by J15 using Cepheid variable stars to determine the distance zero point and fitting variations in $\overline{M}_{110}$ as a function of galaxy optical or IR color to correct for variations in stellar population age and metallicity. Since SBF are typically measured in giant elliptical galaxies and Cepheids in spiral galaxies, the SBF calibration must take into account the spatial relationship between the elliptical and spiral galaxies in the Fornax and Virgo clusters. The J15 F110W and F160W SBF calibration was performed using optical F850LP SBF distances (both individual and mean cluster distances) for a subset of 16 galaxies in the extensive ACS SBF surveys of the Virgo and Fornax clusters (Blakeslee et al. 2009). The SBF distances for those large surveys were derived from the Cepheid measurements and tied to the LMC Cepheid distance modulus of 18.50 mag (Freedman et al. 2001; Freedman & Madore 2010). For this study we have adopted the updated LMC distance of 18.477 mag (Pietrzyński et al. 2019). The systematic zero point uncertainty arising from this calibration chain was estimated to be 0.10 mag by J15, Cantiello et al. (2018), and Blakeslee et al. (2010). Improvements in the

distance to the LMC reduce this uncertainty to 0.09 mag (for details, see Section 2.4 of Blakeslee et al. 2021).

This study includes several other procedural improvements and updates from the detailed calibration presented by J15, including changes to the initial *HST* pipeline reduction, correction for sky background and undetected sources, choice of PSF reference stars, etc. These changes have little or no effect on the measurement of $\overline{m}_{110}$ for the nearby galaxies in the Virgo and Fornax clusters where the SBF signal is large and is small, but are important for the more distant sample here. Some of the changes to the calibration zero point have been described by Cantiello et al. (2018). A small change in the ACS calibration led to a 0.004 mag shift in the ACS $(g-z)$ colors, resulting in a 0.009 mag shift in $\overline{M}_{110}$. A more significant change of 0.05 mag to the zero point was the result of the expanded WFC3/IR PSF library that we used for NGC 4993 and all the galaxies in this survey. The increased S/N of the brighter PSF stars also reduced the individual statistical uncertainty considerably.

5. COLOR MEASUREMENTS AND TRANSFORMATIONS

Measuring accurate SBF distances also requires knowledge of the galaxy's color to correct the absolute fluctuation magnitude $\overline{M}_{110}$ for variations in the age and metallicity of the underlying stellar population (Jensen et al. 2015, 2003; Tonry et al. 1997). Optical $(g-z)$ colors are effective for constraining population variations, particularly for SBF measurements at wavelengths near 1 μm where the effects of age and metallicity are largely degenerate. In this section we establish the transform for determining the colors needed for WFC3/IR SBF measurements from the ground-based Panoramic Survey Telescope and Rapid Response System (PanSTARRS) as an alternative to ACS F475W and F850LP photometry (Waters et al. 2016). Similar transformations for the Sloan Digital Sky Survey (SDSS) and 2-Micron All-Sky Survey (2MASS) can be found in the Appendix.

The IR SBF calibration galaxies from J15 and the observations of NGC 4993 (Cantiello et al. 2018) had ample ACS F475W and F850LP imaging for determination of the $(g_{475}-z_{850})$ colors and deep F110W and F160W observations useful for determining $(J_{110}-H_{160})$. This is not generally the case for most *HST* observations, however, and the subsequent IR SBF projects described in this paper rely on ground-based color measurements instead of using valuable *HST* orbits for color measurements. For the purpose of establishing a uniform WFC3/IR SBF database, we have carefully cross-calibrated the WFC3/IR F110W SBF distance calibra-

tion using PanSTARRS survey DR1 images (Chambers et al. 2019; Waters et al. 2020) and 2MASS images (2MASS, Skrutskie et al. 2006) for $(J-H)$ as an alternative when $(g-z)$ is unavailable or unreliable due to high optical foreground extinction. In all cases we used the survey images to consistently measure colors in the specific annuli used for SBF, and did not rely on catalog photometry for the galaxies.

The PanSTARRS images are preferred for measuring $(g-z)$ colors in support of WFC3/IR SBF because they have higher spatial resolution and greater depth than SDSS or 2MASS, making color measurements more reliable in the outer annuli. PanSTARRS $(g-z)$ colors were used for all the distances in this paper with the exception of ESO 125-G006, for which no $(g-z)$ data was available. To measure colors using PanSTARRS, we retrieved large g and z-band images (12.5 arcmin square) from the public archive.[4] We determined the background level for each image from regions well away from the target galaxies. We then constructed masks of stars and other galaxies by first subtracting a smooth model of the galaxy and then using SExtractor (Bertin & Arnouts 1996) on the galaxy-subtracted images to identify and mask objects. We manually masked any undetected objects and regions where the background subtraction left sharp edges or other processing artifacts. The next step was to apply the correct photometric calibration for each image (in AB mag) and scale by the relative exposure times in the headers, correct for extinction (Schlafly & Finkbeiner 2011), and create the color map image.

Once we had a color map for each galaxy, we applied a series of annular masks to each map and measured the median color in the same regions of the galaxies that we used to measure the SBF magnitudes in the WFC3/IR images (the color maps were not remapped to the WFC3/IR focal plane geometry, so there is a distortion of a few percent in the y-axis in the outer annuli). The majority of the galaxies in this survey are giant elliptical or massive S0 galaxies that have little or no color gradient in the regions used for SBF analysis, but this step was still important to ensure that we could measure SBF distances completely independently in several radial regions of each galaxy and use the radial variations in the SBF magnitudes to further constrain background subtraction uncertainties and distinguish such from population variations in the galaxies.

Translating the PanSTARRS colors into the relevant ACS photometric system used for the J15 calibration

---

[4] http://panstarrs.stsci.edu

required a statistically significant overlap sample with which to make the comparison. The J15 sample contains 16 galaxies total, eight in the Fornax cluster and eight in the Virgo cluster. Four of the Virgo galaxies were low-luminosity blue dwarf galaxies; not only were they outside the calibration color range (their inclusion in the J15 sample was primarily for studying stellar population variations), but they were also poorly measured in the ground-based optical survey images. The Fornax cluster is too far to be included in the PanSTARRS survey. The remaining four galaxies from J15 are too few to get a robust color calibration link, so we expanded the sample by including 68 Virgo cluster galaxies from the ACS Virgo Cluster Survey (Mei et al. 2007; Blakeslee et al. 2009). These galaxies do not have IR SBF measurements, but they do allow us to link the $(g-z)$ colors from PanSTARRS to the ACS $(g_{475}-z_{850})$ color system for 68 galaxies.

Multiple color maps of the same galaxies from four different sources (ACS, PanSTARRS, SDSS, and 2MASS) allowed us to compare radial luminosity and color profiles and check consistency (see the Appendix). We found that the ACS, PanSTARRS, and SDSS $(g-z)$ color profiles are consistent near the centers of the galaxies, in the innermost SBF measurement annulus; the PanSTARRS profiles remain consistent with ACS farther out, but the SDSS and 2MASS are not as deep and the color measurements become inconsistent and noisy in the outer annuli. We therefore computed the calibration offsets for the central region and use the PanSTARRS $(g-z)$ measurements for the SBF measurements in all the annuli.

The PanSTARRS $(g-z)$ colors differ from the ACS system by about 10% with a modest slope with galaxy color. The relation we measured for 68 calibrators in the inner, high surface brightness region is:

$$(g_{475}-z_{850})_{ACS} = 1.092(g-z)_{PS} - 0.009 \qquad (3)$$

in AB mags (Fig. 2), with a standard deviation of 0.016 mag measured among the subset of 33 color calibrators with $(g_{475}-z_{850})$ between 1.3 and 1.5 mag, the same color range as the SBF sample galaxies. The color calibration is nearly identical in the next two larger annuli, where the scatter is 0.016 and 0.018 mag, respectively. The fit is shown in Figure 2; since all of the target SBF galaxies have $(g-z)$ colors in a narrow range, the distance measurements are not very sensitive to the slope in Equation 3. We adopted the standard deviation of the color calibrator galaxies with $(g_{475}-z_{850}) > 1.3$ as the uncertainty on the PanSTARRS color measurements, added in quadrature with the extinction uncertainty (see Section 6).
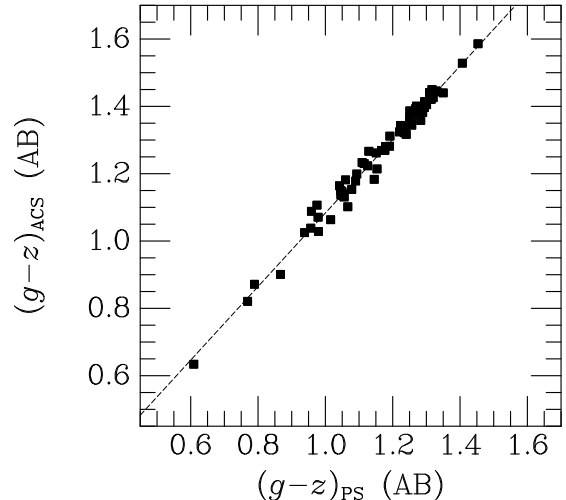
Figure 2. Relationship between PanSTARRS and ACS $(g-z)$ color photometry for 68 galaxies in the ACSVCS sample.

For IR SBF, when foreground extinction is high or $(g-z)$ colors are unavailable, $(J-H)$ can be used instead (e.g., ESO 125-G006 in this study). In the near IR, the range of $(J-H)$ color spanned by different stellar populations is smaller, however, and the leverage on population variations is therefore reduced and the corresponding uncertainty is larger. The $(J-H)$ distances are discussed in the Appendix.

6. SBF UNCERTAINTIES

The apparent fluctuation magnitudes $\overline{m}_{110}$ are subject to several sources of uncertainty that were measured empirically by repeating the SBF measurements with different input parameters in different independent annular regions around the galaxy center. These uncertainties, which were treated as independent and added in quadrature, include:

1. Power spectrum fit uncertainty. The process of fitting the PSF power spectrum to the residual data results in a statistical fit uncertainty of $\sim 2\%$. The quality of the power spectrum fit is affected by the number of good pixels in the annulus, the spatial structure of the mask, and patterns in the residual image due to shells, bars, spiral arms, or tidal interaction features. Residual features often have low-wavenumber power that can be filtered in the power spectrum fit.

2. Background subtraction. The background subtraction exhibits scatter due to uncertain correction for the He emission, instrumental background, and the fit of the galaxy model. Once the back-

ground was determined as described above, we off-set the background subtraction by $\pm 1\sigma$ and repeated the entire SBF measurement in each annulus, and used the offsets in the uncertainty calculation. Background subtraction uncertainty increases substantially in the outer annuli where the galaxy surface brightness is faintest.

3. PSF fit. As described above, we developed a library of PSF reference stars. For any given galaxy, some PSF stars fit better than others (depending on the details of the fine guidance and dithering accuracy). After choosing the best PSF for a particular observation, we then repeated the SBF measurements in all four annuli with 12 individual PSF stars, and used the standard deviation of the measurements as the PSF fitting uncertainty for each annulus.

4. Globular cluster and background galaxy correction. To determine the uncertainty on the correction for background galaxies and undetected globular clusters, we used the difference between the results achieved using SExtractor and DoPHOT independently. We adopted a correction uncertainty of one half of the difference, added in quadrature with a minimum estimated uncertainty of 25% of the fractional contribution P_r/P_0.

5. Extinction correction. The extinction in the F110W filter is quite low for the majority of the galaxies (see Table 1); 10% of the extinction was added to the uncertainty in $\overline{m}_{110}$.

The presence of dust in a galaxy also adds to the uncertainty in $\overline{m}_{110}$, but in ways that are not easily quantified. Clumpy dust can add to the fluctuation power quite dramatically, while a uniform screen of dust would reduce the apparent brightness of the galaxy. The effects of dust are greatly reduced when we use the optical images and color maps to identify and mask dusty regions of the galaxy. We have included the uncertainty in the foreground Galactic extinction as part of the error budget but do not add an additional contribution from dust in the target galaxy. Instead, we mask the dusty regions and flag galaxies with apparent dust when computing distances. Computations of the Hubble constant are not significantly affected by including or excluding galaxies with dust (Blakeslee et al. 2021).

Our final $\overline{m}_{110}$ was computed by taking the uncertainty-weighted mean of the SBF measurements in the good annuli (usually two or three of the four) as discussed in Section 3.6. The combined uncertainty in

$\overline{m}_{110}$ used in calculating the distances was the weighted

Table 2. SBF Uncertainties

Uncertainty Source σ	Median (mag)	Range (mag)
Power spectrum fit (P_0)	0.020	0.01–0.08
Background subtraction	0.020	0.01–0.11
PSF fit	0.015	0.012–0.062
GCLF + galaxy LF fits (P_r)	0.027	0.001–0.119
F110W extinction correction	0.004	0.0004–0.014
Combined $\overline{m}_{110}$ uncertainty[a]	0.057	0.021–0.131
($g-z$) extinction correction	0.011	0.001–0.036
Total ($g-z$) uncertainty	0.021	0.016–0.040
Stellar population scatter[b]	0.06	0.05–0.06
Combined $\overline{M}_{110}$ uncertainty[c]	0.075	0.060–0.105
Total ($m-M$) uncertainty	0.085	0.072–0.195

[a] Individual sources of uncertainty added in quadrature for each annulus.

[b] The scatter due to stellar population variations was measured by Jensen et al. (2015) and Cantiello et al. (2018).

[c] The combined uncertainty on $\overline{M}_{110}$ includes the total ($g-z$) uncertainty times 2.16 added in quadrature with the stellar population scatter.

average of the uncertainties in the good annuli (with the extinction uncertainty treated as a systematic uncertainty common to all annuli), which has a median value of 0.057 mag. Median values and ranges for the individual sources of uncertainty are listed in Table 2.

The uncertainty associated with the absolute fluctuation magnitude $\overline{M}_{110}$ includes the color measurement uncertainty and intrinsic scatter due to population variations. Although the old massive galaxies in this sample typically show very little color gradient, we still computed $\overline{M}_{110}$ for each annulus using the ($g-z$) or ($J-H$) color measured in each region. The weighted average distance for each galaxy made use of the individual $\overline{M}_{110}$ values. The combined uncertainty in the weighted average included the rms scatter for the color conversions added in quadrature with 10% of the difference between the g and z extinction values. The median ($g-z$) uncertainty calculated in this way was 0.021 mag (Table 2). The combined color uncertainty was added in quadrature (multiplied by the calibration slope of 2.16) with the $\overline{M}_{110}$ calibration uncertainty of 0.06 mag arising from stellar population variations (Blakeslee et al. 2009; Jensen et al. 2015; Cantiello et al. 2018). Combining the $\overline{m}_{110}$ and $\overline{M}_{110}$ uncertainties in quadrature gives a median uncertainty on our distance moduli of 0.085 mag, or ~3.9% in distance (see Table 2).

Table 3. F110W SBF Distances and Velocities

Galaxy	$(g-z)$	$\overline{m}_{110}$	$(\overline{m}-\overline{M})$	$d_{\rm SBF}$	$v_{\rm gal}$	$v_{\rm grp}$	$v_{\rm flow}$	v_{2M++}	$v_{\rm rms}$	$N_{\rm grp}$
	(mag)	(mag)	(mag)	(Mpc)	(km/s)	(km/s)	(km/s)	(km/s)	(km/s)	
(1)	(2)	(3)	(4)	(5)	(6)	(7)	(8)	(9)	(10)	(11)
IC 2597	1.509 ± 0.021	31.044 ± 0.031	33.673 ± 0.082	54.3 ± 2.1	3334	4099	4003	4227	648	85
NGC 0057	1.613 ± 0.022	31.723 ± 0.053	34.126 ± 0.094	66.9 ± 2.9	5088	5278	5875	5485	339	6
NGC 0315	1.561 ± 0.022	31.650 ± 0.027	34.166 ± 0.081	68.1 ± 2.5	4635	4819	4707	4938	327	14
NGC 0383	1.513 ± 0.021	31.481 ± 0.037	34.101 ± 0.084	66.1 ± 2.6	4802	4900	4555	5087	432	48
NGC 0410	1.538 ± 0.020	31.371 ± 0.034	33.937 ± 0.082	61.3 ± 2.3	5002	4900	4579	5086	432	48
NGC 0495	1.456 ± 0.021	31.306 ± 0.030	34.049 ± 0.081	64.5 ± 2.4	3831	4626	4181	4547	424	47
NGC 0507	1.497 ± 0.021	31.298 ± 0.032	33.953 ± 0.081	61.7 ± 2.3	4651	4626	4196	4548	424	47
NGC 0524	1.565 ± 0.024	29.703 ± 0.043	32.212 ± 0.090	27.7 ± 1.1	2068	2166	2429	2229	171	9
NGC 0533	1.514 ± 0.018	31.693 ± 0.029	34.310 ± 0.077	72.8 ± 2.6	5240	5073	5013	5177	351	8
NGC 0545	1.426 ± 0.019	31.682 ± 0.083	34.489 ± 0.110	79.0 ± 4.0	5162	5083	5214	5184	460	43
NGC 0547	1.459 ± 0.019	31.653 ± 0.063	34.391 ± 0.096	75.5 ± 3.3	5162	5083	5214	5184	460	43
NGC 0665	1.525 ± 0.024	31.380 ± 0.027	33.973 ± 0.084	62.3 ± 2.4	5127	5074	5283	5164	168	9
NGC 0708	1.581 ± 0.024	31.476 ± 0.029	33.945 ± 0.085	61.5 ± 2.4	4601	4687	4182	4521	520	63
NGC 0741	1.560 ± 0.020	31.696 ± 0.028	34.214 ± 0.080	69.6 ± 2.6	5280	5144	5308	5172	189	8
NGC 0777	1.564 ± 0.019	31.652 ± 0.036	34.161 ± 0.082	68.0 ± 2.6	4758	4988	4851	5265	148	10
NGC 0809	1.311 ± 0.017	31.320 ± 0.084	34.376 ± 0.109	75.0 ± 3.8	5080	5148	5469	5302	0	1
NGC 0890	1.399 ± 0.023	30.430 ± 0.022	33.296 ± 0.081	45.6 ± 1.7	3745	3782	3361	3248	0	1
NGC 0910	1.532 ± 0.021	31.880 ± 0.055	34.459 ± 0.093	77.9 ± 3.3	4995	5597	6051	5993	656	54
NGC 1016	1.531 ± 0.018	32.089 ± 0.047	34.670 ± 0.085	85.9 ± 3.4	6428	6449	6533	6350	512	16
NGC 1060	1.572 ± 0.040	31.160 ± 0.016	33.653 ± 0.108	53.8 ± 2.7	4977	4788	4270	4668	474	21
NGC 1129	1.557 ± 0.027	31.580 ± 0.043	34.105 ± 0.095	66.2 ± 2.9	5009	5247	5244	5218	683	46
NGC 1167	1.463 ± 0.037	30.922 ± 0.050	33.650 ± 0.113	53.7 ± 2.8	4757	4808	4234	4514	105	4
NGC 1200	1.467 ± 0.022	30.940 ± 0.026	33.660 ± 0.080	54.0 ± 2.0	3805	3793	3822	3721	104	4
NGC 1201	1.425 ± 0.017	28.538 ± 0.021	31.347 ± 0.074	18.6 ± 0.6	1494	1500	1856	1754	0	1
NGC 1259	1.477 ± 0.033	31.668 ± 0.046	34.365 ± 0.105	74.6 ± 3.6	5653	5281	5031	5199	962	180
NGC 1272	1.529 ± 0.034	31.671 ± 0.022	34.256 ± 0.099	71.0 ± 3.2	3655	5281	4984	5194	962	180
NGC 1278	1.512 ± 0.035	31.580 ± 0.044	34.202 ± 0.106	69.2 ± 3.4	5931	5281	4980	5193	962	180
NGC 1453	1.532 ± 0.026	30.967 ± 0.022	33.546 ± 0.085	51.2 ± 2.0	3778	3946	3867	3879	193	13
NGC 1573	1.504 ± 0.030	31.374 ± 0.027	34.014 ± 0.094	63.5 ± 2.7	4161	4408	4411	4594	320	17
NGC 1600	1.486 ± 0.020	31.600 ± 0.038	34.277 ± 0.083	71.7 ± 2.7	4620	4502	4450	4570	401	30
NGC 1684	1.412 ± 0.020	31.151 ± 0.025	33.989 ± 0.079	62.8 ± 2.3	4378	4511	4471	4610	226	15
NGC 1700	1.368 ± 0.019	30.657 ± 0.022	33.590 ± 0.076	52.2 ± 1.8	3870	3953	3783	3808	143	7
NGC 2258	1.541 ± 0.029	31.221 ± 0.034	33.781 ± 0.094	57.0 ± 2.5	4055	3979	4102	4053	105	3
NGC 2274	1.499 ± 0.026	31.545 ± 0.025	34.196 ± 0.086	69.1 ± 2.7	5171	5207	4861	5233	136	6
NGC 2340	1.537 ± 0.022	31.947 ± 0.067	34.514 ± 0.102	79.9 ± 3.8	6007	6061	6292	6071	512	29
NGC 2513	1.484 ± 0.018	31.576 ± 0.033	34.258 ± 0.078	71.1 ± 2.6	4903	4724	4623	4802	318	7
NGC 2672	1.497 ± 0.017	31.450 ± 0.040	34.103 ± 0.081	66.2 ± 2.5	4611	4502	4067	4503	129	5
NGC 2693	1.501 ± 0.017	31.609 ± 0.065	34.256 ± 0.096	71.0 ± 3.1	5098	5248	5483	5271	97	6
NGC 2765	1.346 ± 0.018	30.744 ± 0.041	33.725 ± 0.083	55.6 ± 2.1	4086	4130	4239	4184	0	1
NGC 2962	1.465 ± 0.020	29.789 ± 0.040	32.532 ± 0.084	32.1 ± 1.2	2300	2354	2485	2490	57	2
NGC 3158	1.548 ± 0.017	32.261 ± 0.069	34.806 ± 0.099	91.5 ± 4.2	7170	7185	7490	7120	388	13
NGC 3392	1.351 ± 0.016	30.890 ± 0.054	33.861 ± 0.088	59.2 ± 2.4	3340	3456	3953	3751	121	2

Table 3 *continued*

Table 3 *(continued)*

Galaxy	$(g-z)$	$\overline{m}_{110}$	$(\overline{m}-\overline{M})$	$d_{\rm SBF}$	$v_{\rm gal}$	$v_{\rm grp}$	$v_{\rm flow}$	v_{2M++}	$v_{\rm rms}$	$N_{\rm grp}$
	(mag)	(mag)	(mag)	(Mpc)	(km/s)	(km/s)	(km/s)	(km/s)	(km/s)	
(1)	(2)	(3)	(4)	(5)	(6)	(7)	(8)	(9)	(10)	(11)
NGC 3504[a]	1.312 ± 0.023	29.630 ± 0.039	32.683 ± 0.095	34.4 ± 3.8	1829	1760	1981	2009	110	2
NGC 3842	1.532 ± 0.017	32.132 ± 0.073	34.711 ± 0.102	87.5 ± 4.1	6561	6987	6665	6656	707	61
NGC 4036	1.447 ± 0.018	29.013 ± 0.031	31.776 ± 0.078	22.7 ± 0.8	1574	1442	1580	1693	124	3
NGC 4073	1.529 ± 0.019	32.060 ± 0.121	34.646 ± 0.141	85.0 ± 5.5	6268	6380	6152	6154	358	13
NGC 4386	1.442 ± 0.019	29.653 ± 0.034	32.427 ± 0.080	30.6 ± 1.1	1721	1661	1807	1940	188	7
NGC 4839	1.553 ± 0.017	32.267 ± 0.065	34.800 ± 0.096	91.2 ± 4.0	7610	7331	7202	7324	866	136
NGC 4874	1.545 ± 0.012	32.430 ± 0.107	34.981 ± 0.128	99.1 ± 5.8	7436	7331	7230	7336	866	136
NGC 4914	1.317 ± 0.018	31.090 ± 0.023	34.133 ± 0.075	67.1 ± 2.3	4896	4962	5228	4813	2	2
NGC 4993[b]	1.329 ± 0.027	30.024 ± 0.043	33.023 ± 0.076	40.2 ± 1.4	3215	2924	2989	2888	143	8
NGC 5322	1.432 ± 0.017	29.695 ± 0.013	32.490 ± 0.072	31.5 ± 1.0	1857	2071	2365	2366	213	8
NGC 5353	1.525 ± 0.017	30.116 ± 0.028	32.711 ± 0.076	34.8 ± 1.2	2510	2645	2712	2827	160	18
NGC 5490	1.490 ± 0.018	31.597 ± 0.036	34.267 ± 0.080	71.4 ± 2.6	5092	5357	5307	5043	280	8
NGC 5557	1.378 ± 0.017	30.546 ± 0.015	33.458 ± 0.072	49.2 ± 1.6	3390	3295	3667	3363	158	4
NGC 5839	1.386 ± 0.019	29.475 ± 0.027	32.369 ± 0.078	29.8 ± 1.1	1417	1825	1534	1821	280	13
NGC 6482	1.534 ± 0.026	30.994 ± 0.040	33.570 ± 0.091	51.8 ± 2.2	3859	3871	3824	3908	121	3
NGC 6702	1.397 ± 0.026	31.121 ± 0.029	33.992 ± 0.087	62.9 ± 2.5	4592	4648	4751	4781	0	1
NGC 6964	1.421 ± 0.025	30.867 ± 0.052	33.685 ± 0.096	54.6 ± 2.4	3494	3698	3622	3811	253	8
NGC 7052	1.511 ± 0.028	31.333 ± 0.031	33.957 ± 0.092	61.9 ± 2.6	4362	4412	4353	4561	0	1
NGC 7242	1.529 ± 0.033	31.918 ± 0.044	34.504 ± 0.104	79.6 ± 3.8	5439	5610	6284	5703	389	17
NGC 7619	1.516 ± 0.023	30.727 ± 0.023	33.341 ± 0.081	46.6 ± 1.7	3391	3043	3237	3102	306	16
ESO125-G006	0.22 ± 0.024[c]	31.670 ± 0.056	34.896 ± 0.195	95.3 ± 8.6	6762	6883	6766	6752	0	1

[a] F110W measurements from Nguyen et al. (2020) adjusted by –0.023 mag.

[b] F110W measurements from Cantiello et al. (2018) adjusted by –0.023 mag.

[c] The color used for ESO 125-G006 is $(J-H)$, not $(g-z)$.

Column notes: (1) galaxy name; (2) $(g-z)$ colors from PanSTARRS transformed to the ACS $(g_{475}-z_{850})$ system using Equation 3, with the exception of ESO 125-G006, which is $(J-H)$ from 2MASS transformed to $(J_{110} - H_{160})$ using Equation A8; (3) Apparent fluctuation magnitude; (4) SBF distance modulus; (5) SBF distance; (6) individual and (7) group velocities in the CMB frame are taken from the Cosmic Flows 3 Extragalactic Database (Tully 2015; Tully et al. 2009, see also http://edd.ifa.hawaii.edu) except NGC 4993 (Cantiello et al. 2018); (8) flow-corrected velocities derived from the linear velocity model used in Cosmic Flows 3 (Graziani et al. 2019) using the calculator described by Kourkchi et al. (2020); (9) redshift velocities from the 2M++ compilation of Carrick et al. (2015); (10) rms velocity dispersion of the cluster or group to which the galaxy belongs (0 for solitary galaxies); and (11) the number of galaxies in the cluster or group, both from the Cosmic Flows 3 Extragalactic Database.

7. DISTANCE CALCULATIONS

Distance moduli for each annulus were computed using the absolute magnitude

$$\overline{M}_{110} = -2.864 + 2.16[(g-z)_{\rm ACS} - 1.4], \qquad (4)$$

which is Equation 1 from Cantiello et al. (2018) using $(g_{475} - z_{850})$ values from ACS and including a correction of -0.023 mag to adjust to the LMC distance of 18.477 mag (Pietrzyński et al. 2019). Similarly,

$$\overline{M}_{110} = -2.841 + 2.36[(g-z)_{\rm PS} - 1.3], \qquad (5)$$

can be used with $(g-z)$ from PanSTARRS as described above in Section 5. The distances listed in Table 3 are

uncertainty-weighted averages of all good annuli with reliable SBF measurements, free of dust or other galaxy subtraction residuals, and with the background level corrected as described above. The individual galaxies are shown in Figure 1, which includes the residual fluctuation images, the spatial power spectra fits, and the GCLF and background galaxy fits.

The nearby J15 calibration galaxies in the Virgo and Fornax clusters required no k-corrections to account for redshift; the more distant galaxies in this sample could require a redshift-dependent filter correction, which would have to be calculated using theoretical SBF models as a function of age and metallicity. The most re-

cent SBF models with published k-corrections are those of Liu et al. (2000). For the standard J filter (similar to F110W), the k-corrections are quite small: 0.003 mag at 50 Mpc and 0.006 mag at 100 Mpc. These model-dependent values are small enough to be insignificant for our distance measurements. The SBF calibration from J15 was compared with several newer stellar population models to explore the sensitivity of the calibration to the spread in age and metallicity as a function of the optical ($g_{475}-z_{850}$) and infrared ($J_{110}-H_{160}$) colors. The SBF signals measured by J15 were consistent for old, metal-rich stellar populations but showed significant scatter for bluer, younger, and metal-poor galaxies. The J15 comparisons also showed significant scatter among the different models compared, but k-corrections were not calculated for those models. Improved IR SBF models will be required before reliable k-corrections can be calculated for distances greater than 100 Mpc.

8. APPLICATIONS

8.1. *MASSIVE Galaxies and Black Hole Masses*

The new SBF distances presented here for the MASSIVE galaxies are on average 8% shorter than the redshift distances adopted by Ma et al. (2014) at the beginning of the MASSIVE project. The original distance estimates were derived assuming a Hubble constant of $H_0 = 70$ kms^{-1}Mpc^{-1} and using group velocities in the CMB frame from Crook et al. (2007). The new SBF distance measurements presented here imply a value of $H_0 \sim 75$ kms^{-1}Mpc^{-1}, as reported by Verde et al. (2019) using the same velocities; the Ma et al. (2014) velocities included the velocity field corrections of Mould et al. (2000), which lead to a somewhat larger value of H_0 than current best estimates (Blakeslee et al. 2021). The new SBF distances obtained here will help reduce one of the major systematic uncertainties in ongoing efforts to determine dynamical masses of black holes in MASSIVE galaxies (e.g. Liepold et al. 2020).

8.2. *Supernova Luminosity Calibration*

This study includes 24 Type Ia supernova host galaxies that can be used to extend the calibration of SN absolute magnitude to earlier galaxy types and nearer the centers of rich clusters. These SBF distances, along with other published SBF distances, is the subject of two companion papers by Garnavich et al. (2021) and Milne et al. (2021) addressing these and other issues related to the SN distance scale. The new SBF distances are also part of a concurrent study by Milne et al. (2021) that explores the dependence of supernova luminosity on galaxy type for the "narrow-normal" SN Ia population. These SBF distances are crucial to extending the SN distance calibration to early-type galaxies for which Cepheid distances are not available, and for determining the relationship between supernova luminosity and UV color (Milne et al. 2013, 2015; Brown et al. 2017, 2019).

8.3. *The Hubble Constant*

The new SBF distances to a substantial sample of galaxies reaching 100 Mpc provides an opportunity to measure the Hubble constant independently of the SN distance scale, which is reported in detail in the paper by Blakeslee et al. (2021). The combined sample of SBF distances gives a robust determination of the Hubble Constant $H_0 = 73.3$ kms^{-1}Mpc^{-1}, where the difference between the current best estimate and that from Verde et al. (2019) is the improvement to the correction for bulk flows (for details, see Blakeslee et al. 2021). The new SBF distances provide important insights into the current disagreement between the values of H_0 derived from SN and cosmic microwave background radiation measurements (Riess et al. 2019; Planck Collaboration et al. 2020).

9. SUMMARY

This paper presents an updated description of the SBF methodology of Jensen et al. (2015) that we used to measure extragalactic distances out to 100 Mpc with WFC3/IR F110W. The revised calibration of $\overline{M}_{110}$ includes the updated distance to the LMC (Pietrzyński et al. 2019) and corrections to the PSF normalization (Cantiello et al. 2018). We also provide transformations between PanSTARRS, SDSS, and ACS ($g-z$) colors, and between 2MASS and WFC3/IR ($J-H$), which are required to determine the SBF distances. The revised procedures and calibration are applied to WFC3/IR F110W observations of 63 galaxies from a variety of *HST* programs to provide a uniform database of IR SBF distances that can now be used for a number of new studies related to the extragalactic distance scale, including a measurement of the Hubble constant (Blakeslee et al. 2021).

APPENDIX

A. ALTERNATE COLOR TRANSFORMATIONS AND DISTANCES

The WFC3/IR SBF calibrations from Cantiello et al. (2018) and J15, shifted by -0.023 mag to take into account the updated distance to the LMC (Pietrzyński et al. 2019) are:

$$\overline{M}_{110} = -2.864 + 2.16[(g_{475}-z_{850})_{\rm ACS} - 1.4] \quad (A1)$$

$$\overline{M}_{160} = -3.617 + 2.13[(g_{475}-z_{850})_{\rm ACS} - 1.4] \quad (A2)$$

$$\overline{M}_{110} = -2.891 + 6.7[(J_{110}-H_{160})_{\rm WFC3} - 0.27] \quad (A3)$$

$$\overline{M}_{160} = -3.645 + 7.1[(J_{110}-H_{160})_{\rm WFC3} - 0.27] \quad (A4)$$

The preferred calibration of $\overline{M}_{110}$ presented by J15 depends on the $(g_{475}-z_{850})$ colors measured in the F475W and F850LP filters using ACS on *HST*. In this Appendix we provide the color transformations required to make WFC3/IR SBF distance measurements using $(g-z)$ colors from the Sloan Digital Sky Survey (SDSS) and $(J-H)$ colors from 2-Micron All-Sky Survey (2MASS) images as we did in Section 7 for the PanSTARRS case.

The SDSS images we used for this study (including both the SBF targets and the ACSVCS galaxies) were taken from the SDSS DR9 data release[5] and processed using the "ubercal" pipeline (Padmanabhan et al. 2008). The ubercal algorithm achieves $\sim$1% photometric calibration across the full survey area using relative stellar fluxes in overlapping observations. The native SDSS flux units were offset by 0.02 mag in the z filter (AB mags) as recommended on the SDSS website[6] and extinction corrected (Schlafly & Finkbeiner 2011).

To create color maps from SDSS images, a similar procedure was followed as was used for the PanSTARRS images (see Section 5). A smooth galaxy model was subtracted, objects were identified and masked using SExtractor, and the background level checked. The galaxy luminosity and color profiles were compared with ACS and PanSTARRS to confirm that the process yielded consistent results.

---

[5] http://sdss.org
[6] http://www.sdss.org/dr16/algorithms/fluxcal/
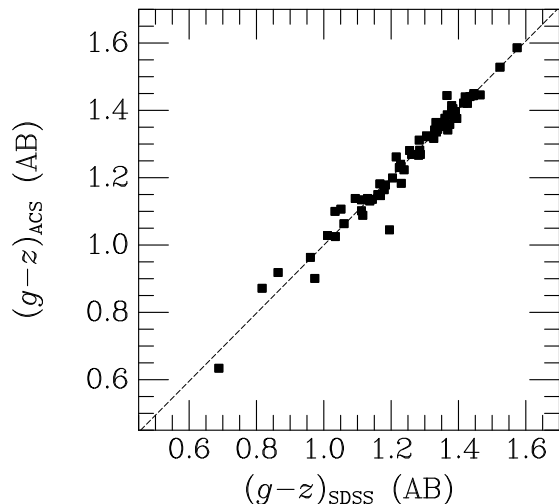
Figure 3. Comparison of SDSS and ACS $(g-z)$ color photometry for 72 galaxies in the ACSVCS sample. The dashed line is the fit from Equation A5.

The SDSS $(g-z)$ color measurements for 72 ACSVCS galaxies are very consistent with the ACS $(g-z)$ colors, with almost no offset or slope, but with somewhat higher scatter than the PanSTARRS measurements (0.019 mag in the inner SBF annulus, increasing to 0.040 and 0.098 mag moving to the outer annuli). The relationship shown in Fig. 3 is

$$(g-z)_{ACS} = 1.010(g-z)_{SDSS} - 0.010. \qquad (A5)$$

For the red early-type galaxies in this sample, the relationship between SDSS and PanSTARRS can be written as

$$(g-z)_{SDSS} = 1.081(g-z)_{PS} + 0.001. \qquad (A6)$$

To use SDSS $(g-z)$ for computing distances, the SBF calibration is therefore

$$\overline{M}_{110} = -2.855 + 2.18[(g-z)_{SDSS} - 1.4]. \qquad (A7)$$

For SBF targets for which ACS, PanSTARRS, or SDSS $(g-z)$ data are not available, 2MASS $(J-H)$ is a viable (though less precise) alternative.[7] The SBF distances calculated using $(g-z)$ are superior to the near-IR $(J-H)$ colors for two reasons: first, the PanSTARRS optical images are deeper and the $(g-z)$ colors are more accurately measured than 2MASS J and H; and second, the dependence of $\overline{M}_{110}$ on color is steeper in the near-IR than it is for $(g-z)$. The slope of $\overline{M}_{110}$ with $(g-z)$ is 2.16 (Equation A1); this means an uncertainty in color of 0.01 mag will result in 0.022 mag uncertainty in distance modulus. Alternatively, when using $(J_{110}-H_{160})$,

[7] http://irsa.ipac.caltech.edu/Missions/2mass.html
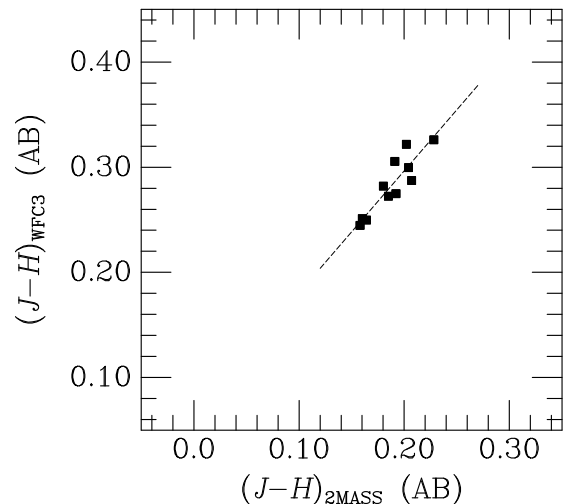
Figure 4. Comparison of WFC3/IR and 2MASS $(J-H)$ colors for 11 calibrator galaxies from J15. The dashed line is the relation from Equation A8. The figure axis limits are set so that the color ranges reflect the same range in derived distance as in Figures 2 and 3, thus the relative scatter in these figures as they affect the distance measurements may be compared directly. The distance calibration using $(J-H)$ has larger scatter because of the limited leverage provided by the relatively small range in $(J-H)$ spanned by the calibrator galaxies (and early-type galaxies in general).

the calibration has a slope of 6.7 (Equation A3) because of the greater age and metallicity sensitivity at longer wavelengths, and so generally IR colors result in less precise distance measurements. For 2MASS, the SBF distance uncertainties are typically twice as large as those for PanSTARRS $(g-z)$.

2MASS $(J-H)$ colors were similarly translated into the WFC3/IR (F110W–F160W) system for SBF measurements using the eleven red galaxies in the Virgo/Fornax calibration sample (J15). For the 2MASS images, the magnitude zero points were retrieved from the image headers and the background level checked (Goullaud et al. 2018, Sec. 2.2). The 2MASS $(J-H)$ colors differ from WFC3/IR $(J_{110}-H_{160})$ by about 10%, with a color translation relationship of

$$(J_{110}-H_{160})_{WFC3} = 1.158(J-H)_{2MASS} + 0.065 \quad (A8)$$

as shown in Figure 4. The corresponding equation for calculating distance moduli is

$$\overline{M}_{110} = -2.891 + 7.76[(J-H)_{2MASS} - 0.177] \quad (A9)$$

where the $(J-H)$ color is in AB mag, which can be computed from the equivalent Vega $(J-H)$ by subtracting 0.492 mag. While the distances measured using $(J-H)$ are less precise, it is still useful for southern hemisphere galaxies for which PanSTARRS data is unavailable, and
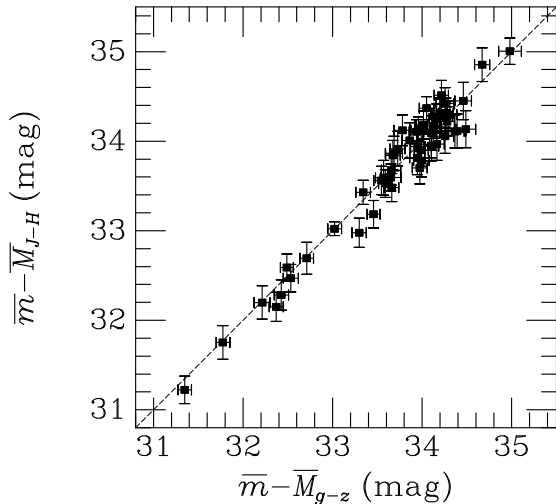
Figure 5. SBF distance moduli computed using $(J−H)$ plotted against the $(g−z)$ SBF distance moduli for the 54 galaxies for which we have reliable 2MASS colors. The dotted line is the 1:1 line, and is not a fit to the data. The $(J−H)$-calibrated distances are less precise but show no significant offset from the distances derived from the PanSTARRS $(g−z)$ color calibration. With one exception (ESO 125-G006), the distances presented in this paper are all derived using the PanSTARRS $(g−z)$ calibration.
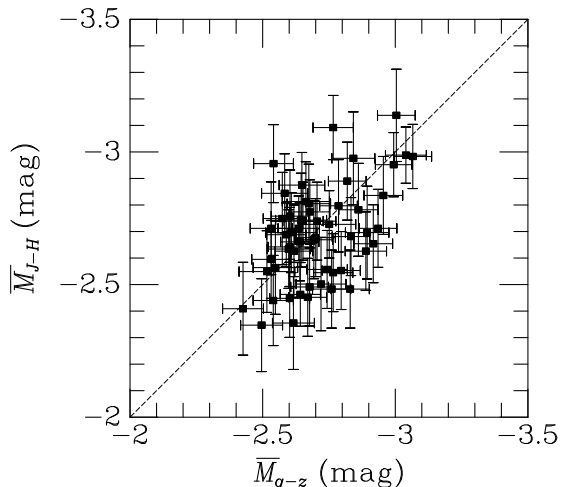
Figure 6. Absolute $\overline{M}_{110}$ derived from $(J−H)$ and $(g−z)$ colors compared to each other. This plot is similar to Figure 5, but is distance independent. The dotted line is the 1:1 line, and is not a fit to the data.

in regions where foreground extinction makes optical color measurements less reliable.

We can use the current sample to establish the reliability of the $(J−H)$ measurements by looking for systematic offsets between the optical and IR color systems and as a function of foreground extinction. The 2MASS colors are completely independent of the PanSTARRS and SDSS $(g−z)$ colors, and are less sensitive to dust ab-
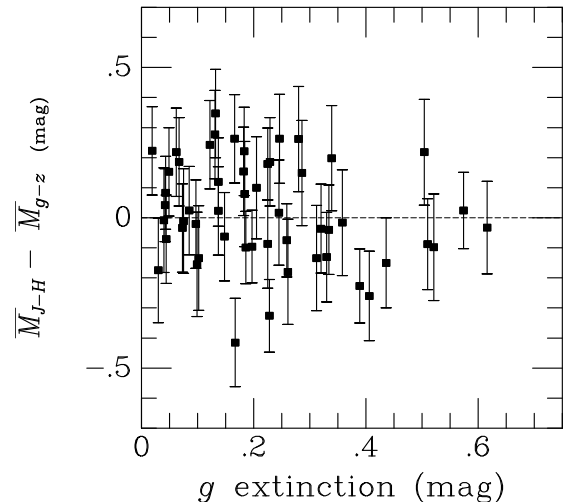
Figure 7. The difference between the $(J−H)$ and $(g−z)$ distances are plotted as a function of optical g-band extinction. Given the relatively large scatter in $\overline{M}_{110}$ determined from the $(g−z)$ and $(J−H)$ colors, we looked for systematic trends in the absolute magnitude differences as a function of extinction and found none.

sorption and Galactic foreground extinction. We plotted the $(g−z)$ and $(J−H)$ SBF distance moduli and $\overline{M}_{110}$ values against each other in Figures 5 and 6. We found that the two systems agree with an insignificant median offset between the $(J−H)$ and $(g−z)$ calibrations of 0.011 mag in distance modulus (measured in individual annuli) and 0.004 mag in $\overline{M}_{110}$ (weighted averages) for 54 galaxies, which is less than the typical uncertainty on an individual $(J−H)$ distance measurement (0.17 mag) divided by the square root of 54. We computed the reduced $\chi^2/N = 0.97$ relative to the one-to-one line (with no degrees of freedom), indicating that our total uncertainties on the distance moduli are statistically robust.

We also checked for systematic offsets between the distances derived using optical and IR colors in Figure 7. There is no evidence of any systematic offset in the $(g−z)$-derived distances compared to the $(J−H)$ values for g-band extinctions up to 0.6 mag, nor any evidence that the scatter in the calibration has any dependence on foreground extinction.

REFERENCES

Alonso-García, J., Mateo, M., Sen, B., et al. 2012, AJ, 143, 70, doi: 10.1088/0004-6256/143/3/70

Beaton, R. L., Bono, G., Braga, V. F., et al. 2018, SSRv, 214, 113, doi: 10.1007/s11214-018-0542-1

Bertin, E., & Arnouts, S. 1996, A&AS, 117, 393, doi: 10.1051/aas:1996164

Blakeslee, J. P., Jensen, J. B., Ma, C.-P., Milne, P. A., & Greene, J. E. 2021, ApJ, 911, 65, doi: 10.3847/1538-4357/abe86a

Blakeslee, J. P., Jordán, A., Mei, S., et al. 2009, ApJ, 694, 556, doi: 10.1088/0004-637X/694/1/556

Blakeslee, J. P., Cantiello, M., Mei, S., et al. 2010, ApJ, 724, 657, doi: 10.1088/0004-637X/724/1/657

Brammer, G., Pirzkal, N., McCullough, P., & MacKenty, J. 2014, WFC3 Instrument Science Report 2014-03, Space Telescope Science Institute

Brown, P. J., Landez, N. J., Milne, P. A., & Stritzinger, M. D. 2017, ApJ, 836, 232, doi: 10.3847/1538-4357/aa5f5a

Brown, P. J., Hosseinzadeh, G., Jha, S. W., et al. 2019, ApJ, 877, 152, doi: 10.3847/1538-4357/ab1a3f

Burns, C. R., Stritzinger, M., Phillips, M. M., et al. 2014, ApJ, 789, 32, doi: 10.1088/0004-637X/789/1/32

Cantiello, M., Brocato, E., & Capaccioli, M. 2011, A&A, 534, A35, doi: 10.1051/0004-6361/201015670

Cantiello, M., Jensen, J. B., Blakeslee, J. P., et al. 2018, ApJL, 854, L31, doi: 10.3847/2041-8213/aaad64

Cappellari, M., McDermid, R. M., Alatalo, K., et al. 2012, Nature, 484, 485, doi: 10.1038/nature10972

Carrick, J., Turnbull, S. J., Lavaux, G., & Hudson, M. J. 2015, MNRAS, 450, 317, doi: 10.1093/mnras/stv547

Chambers, K. C., Magnier, E. A., Metcalfe, N., et al. 2019, The Pan-STARRS1 Surveys. https://arxiv.org/abs/1612.05560

Cho, H., Blakeslee, J. P., Chies-Santos, A. L., et al. 2016, ApJ, 822, 95, doi: 10.3847/0004-637X/822/2/95

Collins, C. A., Stott, J. P., Hilton, M., et al. 2009, Nature, 458, 603, doi: 10.1038/nature07865

Crook, A. C., Huchra, J. P., Martimbeau, N., et al. 2007, ApJ, 655, 790, doi: 10.1086/510201

Davis, T. A., Greene, J., Ma, C.-P., et al. 2016, MNRAS, 455, 214, doi: 10.1093/mnras/stv2313

Davis, T. A., Greene, J. E., Ma, C.-P., et al. 2019, MNRAS, 486, 1404, doi: 10.1093/mnras/stz871

De Lucia, G., & Blaizot, J. 2007, MNRAS, 375, 2, doi: 10.1111/j.1365-2966.2006.11287.x

Dhawan, S., Leibundgut, B., Spyromilio, J., & Blondin, S. 2017, A&A, 602, A118, doi: 10.1051/0004-6361/201629793

Ene, I., Ma, C.-P., McConnell, N. J., et al. 2019, ApJ, 878, 57, doi: 10.3847/1538-4357/ab1f04

Ene, I., Ma, C.-P., Walsh, J. L., et al. 2020. https://arxiv.org/abs/2001.11046

Ene, I., Ma, C.-P., Veale, M., et al. 2018, MNRAS, 479, 2810, doi: 10.1093/mnras/sty1649

Freedman, W. L., & Madore, B. F. 2010, ARA&A, 48, 673, doi: 10.1146/annurev-astro-082708-101829

Freedman, W. L., Madore, B. F., Gibson, B. K., et al. 2001, ApJ, 553, 47, doi: 10.1086/320638

Freedman, W. L., Madore, B. F., Hoyt, T., et al. 2020, ApJ, 891, 57, doi: 10.3847/1538-4357/ab7339

Goulding, A. D., Greene, J. E., Ma, C.-P., et al. 2016, ApJ, 826, 167, doi: 10.3847/0004-637X/826/2/167

Goullaud, C. F., Jensen, J. B., Blakeslee, J. P., et al. 2018, ApJ, 856, 11, doi: 10.3847/1538-4357/aab1f3

Graziani, R., Courtois, H. M., Lavaux, G., et al. 2019, MNRAS, 488, 5438, doi: 10.1093/mnras/stz078

Greene, J. E., Janish, R., Ma, C. P., et al. 2015, ApJ, 807, 11, doi: 10.1088/0004-637X/807/1/11

Greene, J. E., Veale, M., Ma, C.-P., et al. 2019, ApJ, 874, 66, doi: 10.3847/1538-4357/ab01e3

Hamuy, M., Phillips, M. M., Maza, J., et al. 1995, AJ, 109, 1, doi: 10.1086/117251

Jarrett, T. H. 2000, PASP, 112, 1008, doi: 10.1086/316603

Jensen, J. B., Blakeslee, J. P., Gibson, Z., et al. 2015, ApJ, 808, 91, doi: 10.1088/0004-637X/808/1/91

Jensen, J. B., Tonry, J. L., Barris, B. J., et al. 2003, ApJ, 583, 712, doi: 10.1086/345430

Jensen, J. B., Tonry, J. L., & Luppino, G. A. 1998, ApJ, 505, 111, doi: 10.1086/306163

Jensen, J. B., Tonry, J. L., Thompson, R. I., et al. 2001, ApJ, 550, 503, doi: 10.1086/319819

Jones, D. O., Riess, A. G., Scolnic, D. M., et al. 2018, ApJ, 867, 108, doi: 10.3847/1538-4357/aae2b9

Jordán, A., Blakeslee, J. P., Peng, E. W., et al. 2004, ApJS, 154, 509, doi: 10.1086/422977

Kang, Y., Kim, Y.-L., Lim, D., Chung, C., & Lee, Y.-W. 2016, ApJS, 223, 7, doi: 10.3847/0067-0049/223/1/7

Kattner, S., Leonard, D. C., Burns, C. R., et al. 2012, PASP, 124, 114, doi: 10.1086/664734

Khetan, N., Izzo, L., Branchesi, M., et al. 2021, A&A, 647, A72, doi: 10.1051/0004-6361/202039196

Kourkchi, E., Courtois, H. M., Graziani, R., et al. 2020, AJ, 159, 67, doi: 10.3847/1538-3881/ab620e

Krist, J. E., Hook, R. N., & Stoehr, F. 2011, Society of Photo-Optical Instrumentation Engineers (SPIE) Conference Series, Vol. 8127, 20 years of Hubble Space Telescope optical modeling using Tiny Tim, 81270J, doi: 10.1117/12.892762

Lampeitl, H., Smith, M., Nichol, R. C., et al. 2010, ApJ, 722, 566, doi: 10.1088/0004-637X/722/1/566

Liepold, C. M., Quenneville, M. E., Ma, C.-P., et al. 2020, ApJ, 891, 4, doi: 10.3847/1538-4357/ab6f71

Liu, M. C., Charlot, S., & Graham, J. R. 2000, ApJ, 543, 644, doi: 10.1086/317147

Ma, C.-P., Greene, J. E., McConnell, N., et al. 2014, ApJ, 795, 158, doi: 10.1088/0004-637X/795/2/158

Makarov, D., Prugniel, P., Terekhova, N., Courtois, H., & Vauglin, I. 2014, A&A, 570, A13, doi: 10.1051/0004-6361/201423496

Mei, S., Blakeslee, J. P., Côté, P., et al. 2007, ApJ, 655, 144, doi: 10.1086/509598

Milne, P. A., Brown, P. J., Roming, P. W. A., Bufano, F., & Gehrels, N. 2013, ApJ, 779, 23, doi: 10.1088/0004-637X/779/1/23

Milne, P. A., Foley, R. J., Brown, P. J., & Narayan, G. 2015, ApJ, 803, 20, doi: 10.1088/0004-637X/803/1/20

Mould, J. R., Huchra, J. P., Freedman, W. L., et al. 2000, ApJ, 529, 786, doi: 10.1086/308304

Nantais, J. B., Huchra, J. P., Barmby, P., Olsen, K. A. G., & Jarrett, T. H. 2006, AJ, 131, 1416, doi: 10.1086/500011

Nguyen, D. D., den Brok, M., Seth, A. C., et al. 2020, The Astrophysical Journal, 892, 68, doi: 10.3847/1538-4357/ab77aa

Padmanabhan, N., Schlegel, D. J., Finkbeiner, D. P., et al. 2008, ApJ, 674, 1217, doi: 10.1086/524677

Pandya, V., Greene, J. E., Ma, C.-P., et al. 2017, ApJ, 837, 1, doi: 10.3847/1538-4357/aa5ebc

Phan, A., & Jensen, J. B. 2020, in Astronomical Society of the Pacific Conference Series, Vol. 525, 2020 Compendium of Undergraduate Research in Astronomy and Space Science, ed. J. B. Jensen, J. Barnes, & B. Wardell, 45

Pietrzyński, G., Graczyk, D., Gallenne, A., et al. 2019, Nature, 567, 200, doi: 10.1038/s41586-019-0999-4

Pirzkal, N. 2014, WFC3 Instrument Science Report 2014-11, Space Telescope Science Institute

Planck Collaboration, Aghanim, N., Akrami, Y., et al. 2020, A&A, 641, A6, doi: 10.1051/0004-6361/201833910

Quenneville, M. E., Liepold, C. M., & Ma, C.-P. 2020, arXiv e-prints, arXiv:2005.00542. https://arxiv.org/abs/2005.00542

Retzlaff, J., Rosati, P., Dickinson, M., et al. 2010, A&A, 511, A50, doi: 10.1051/0004-6361/200912940

Riess, A. G., Casertano, S., Yuan, W., et al. 2021, ApJL, 908, L6, doi: 10.3847/2041-8213/abdbaf

Riess, A. G., Casertano, S., Yuan, W., Macri, L. M., & Scolnic, D. 2019, ApJ, 876, 85, doi: 10.3847/1538-4357/ab1422

Rigault, M., Aldering, G., Kowalski, M., et al. 2015, ApJ, 802, 20, doi: 10.1088/0004-637X/802/1/20

Rigault, M., Brinnel, V., Aldering, G., et al. 2020, A&A, 644, A176, doi: 10.1051/0004-6361/201730404

Russell, D. G. 2002, ApJ, 565, 681, doi: 10.1086/337917

Schechter, P. L., Mateo, M., & Saha, A. 1993, PASP, 105, 1342, doi: 10.1086/133316

Schlafly, E. F., & Finkbeiner, D. P. 2011, ApJ, 737, 103, doi: 10.1088/0004-637X/737/2/103

Skrutskie, M. F., Cutri, R. M., Stiening, R., et al. 2006, AJ, 131, 1163, doi: 10.1086/498708

Sullivan, M., Conley, A., Howell, D. A., et al. 2010, MNRAS, 406, 782, doi: 10.1111/j.1365-2966.2010.16731.x

Tonry, J., & Schneider, D. P. 1988, AJ, 96, 807, doi: 10.1086/114847

Tonry, J. L., Blakeslee, J. P., Ajhar, E. A., & Dressler, A. 1997, ApJ, 475, 399, doi: 10.1086/303576

Tully, R. B. 2015, AJ, 149, 171, doi: 10.1088/0004-6256/149/5/171

Tully, R. B., Rizzi, L., Shaya, E. J., et al. 2009, AJ, 138, 323, doi: 10.1088/0004-6256/138/2/323

van Dokkum, P. G., & Conroy, C. 2010, Nature, 468, 940, doi: 10.1038/nature09578

Veale, M., Ma, C.-P., Greene, J. E., et al. 2017a, MNRAS, 471, 1428, doi: 10.1093/mnras/stx1639

—. 2018, MNRAS, 473, 5446, doi: 10.1093/mnras/stx2717

Veale, M., Ma, C.-P., Thomas, J., et al. 2017b, MNRAS, 464, 356, doi: 10.1093/mnras/stw2330

Verde, L., Treu, T., & Riess, A. G. 2019, Nature Astronomy, 3, 891, doi: 10.1038/s41550-019-0902-0

Voit, G. M., Ma, C. P., Greene, J., et al. 2018, ApJ, 853, 78, doi: 10.3847/1538-4357/aaa084

Waters, C. Z., Magnier, E. A., Price, P. A., et al. 2016, arXiv e-prints, arXiv:1612.05245. https://arxiv.org/abs/1612.05245

—. 2020, ApJS, 251, 4, doi: 10.3847/1538-4365/abb82b

Windhorst, R. A., Cohen, S. H., Hathi, N. P., et al. 2011, ApJS, 193, 27, doi: 10.1088/0067-0049/193/2/27
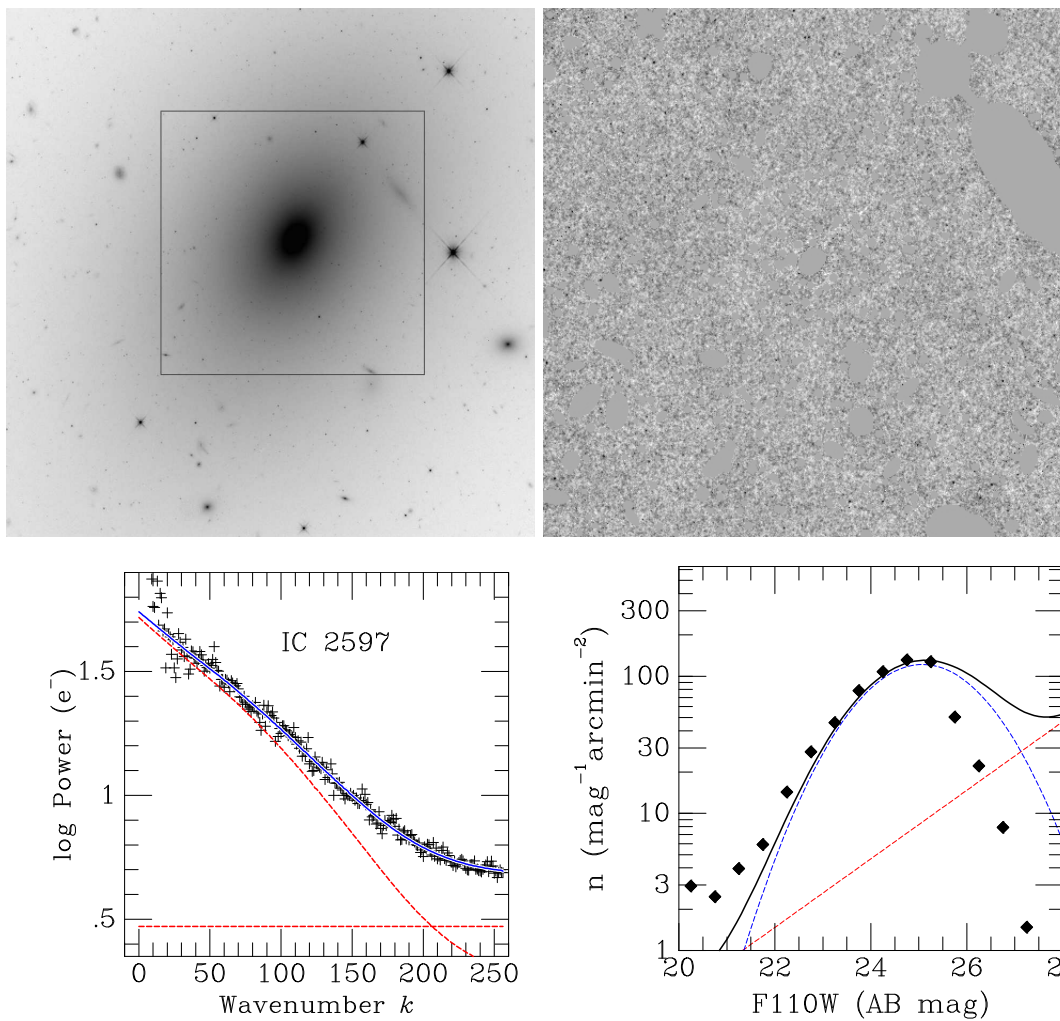
Figure 8. Combined figure for IC 2597.

These figures are included as an online figure set in the published version. They are reproduced here for the convenience of the reader.
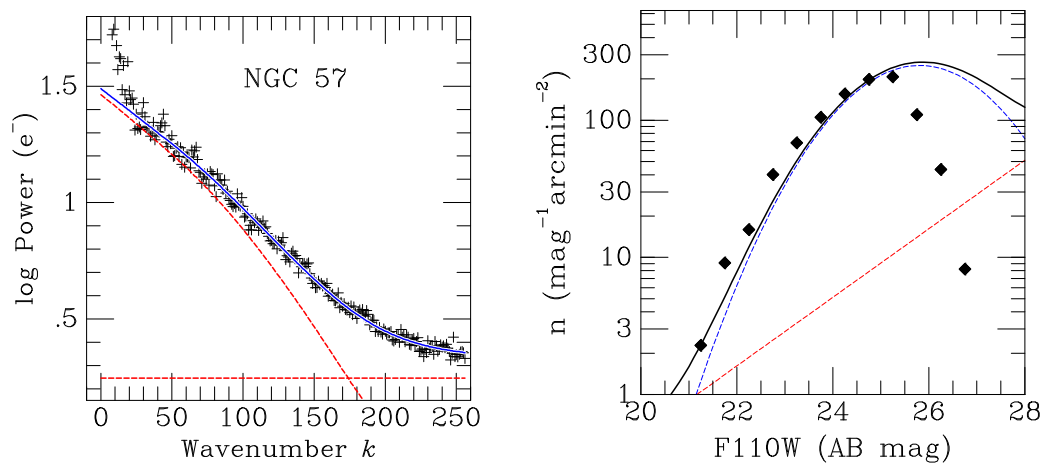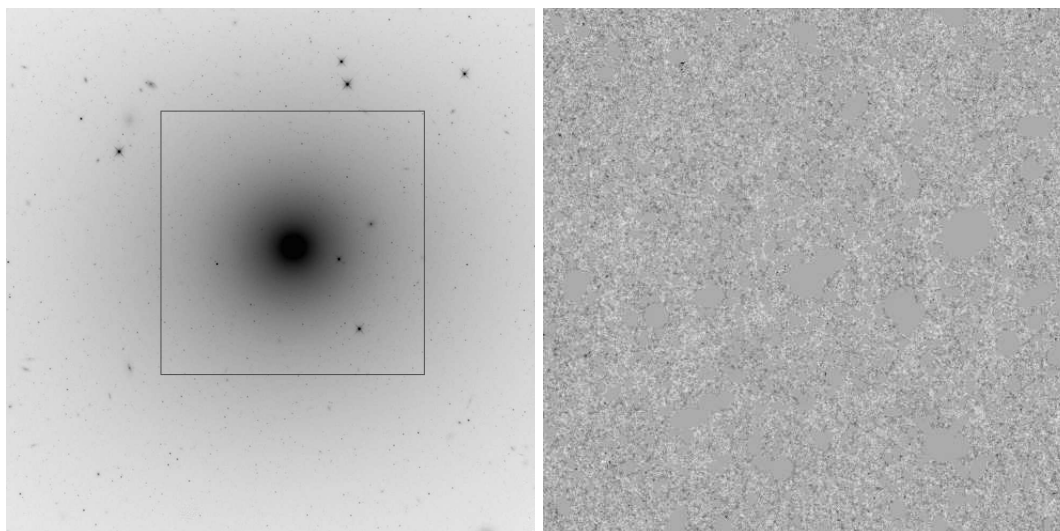
Figure 9. Combined figure for NGC 57.
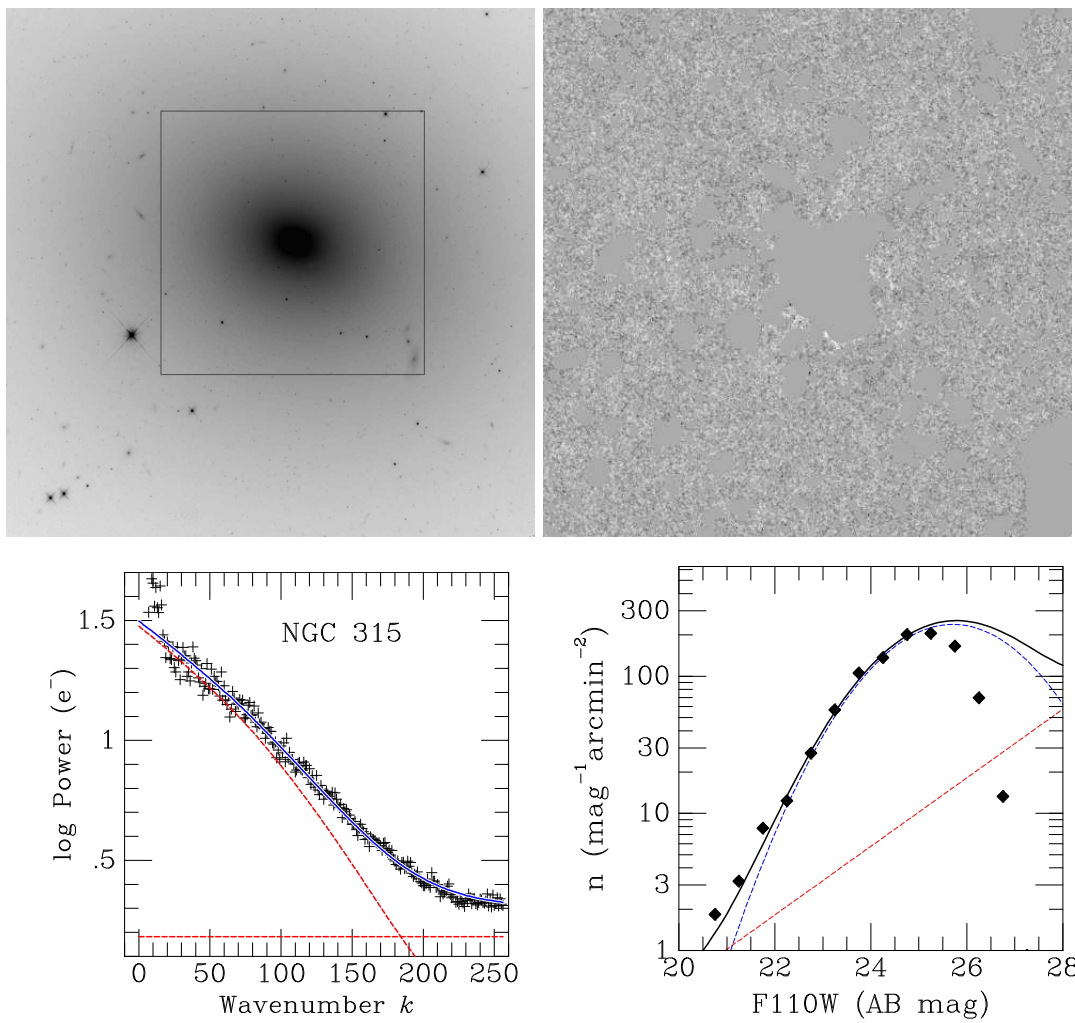
Figure 10. Combined figure for NGC 315.
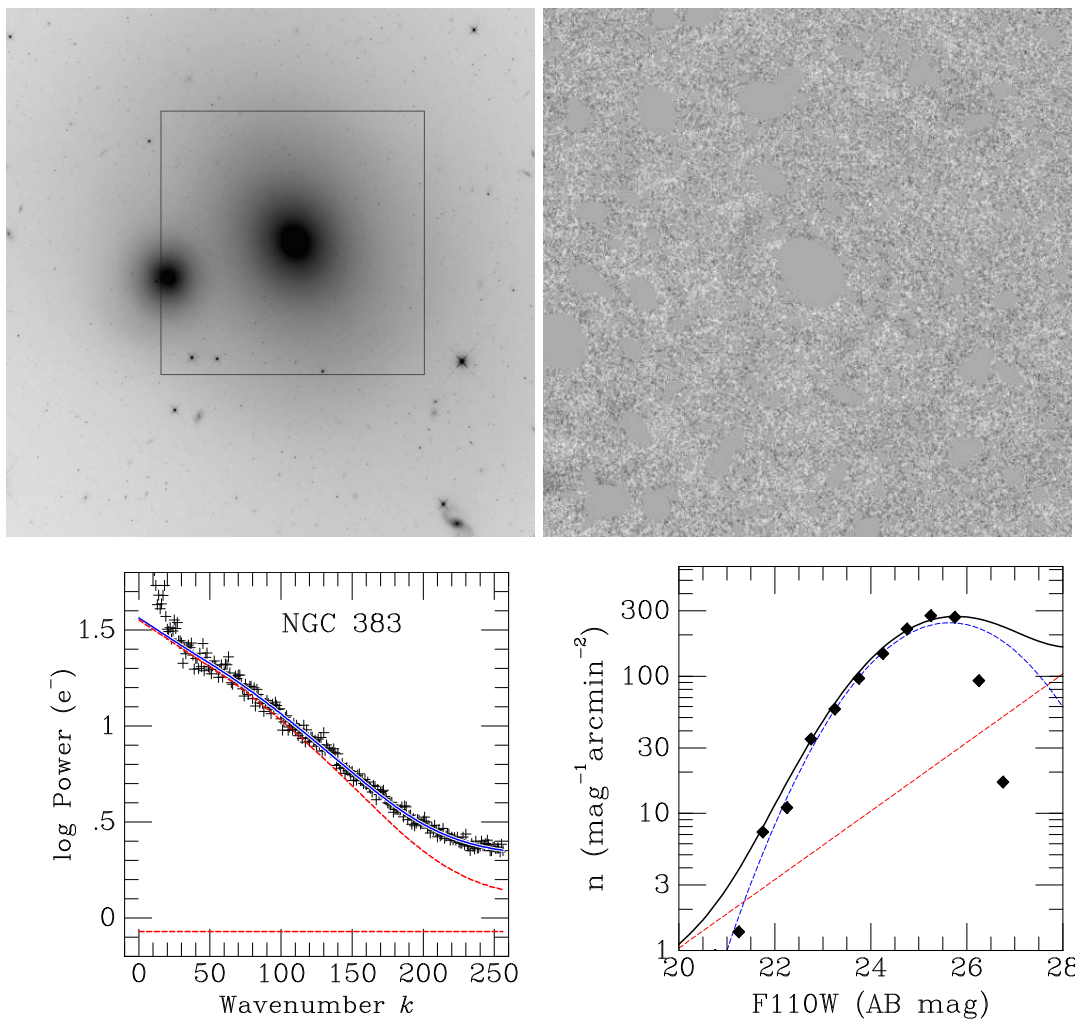
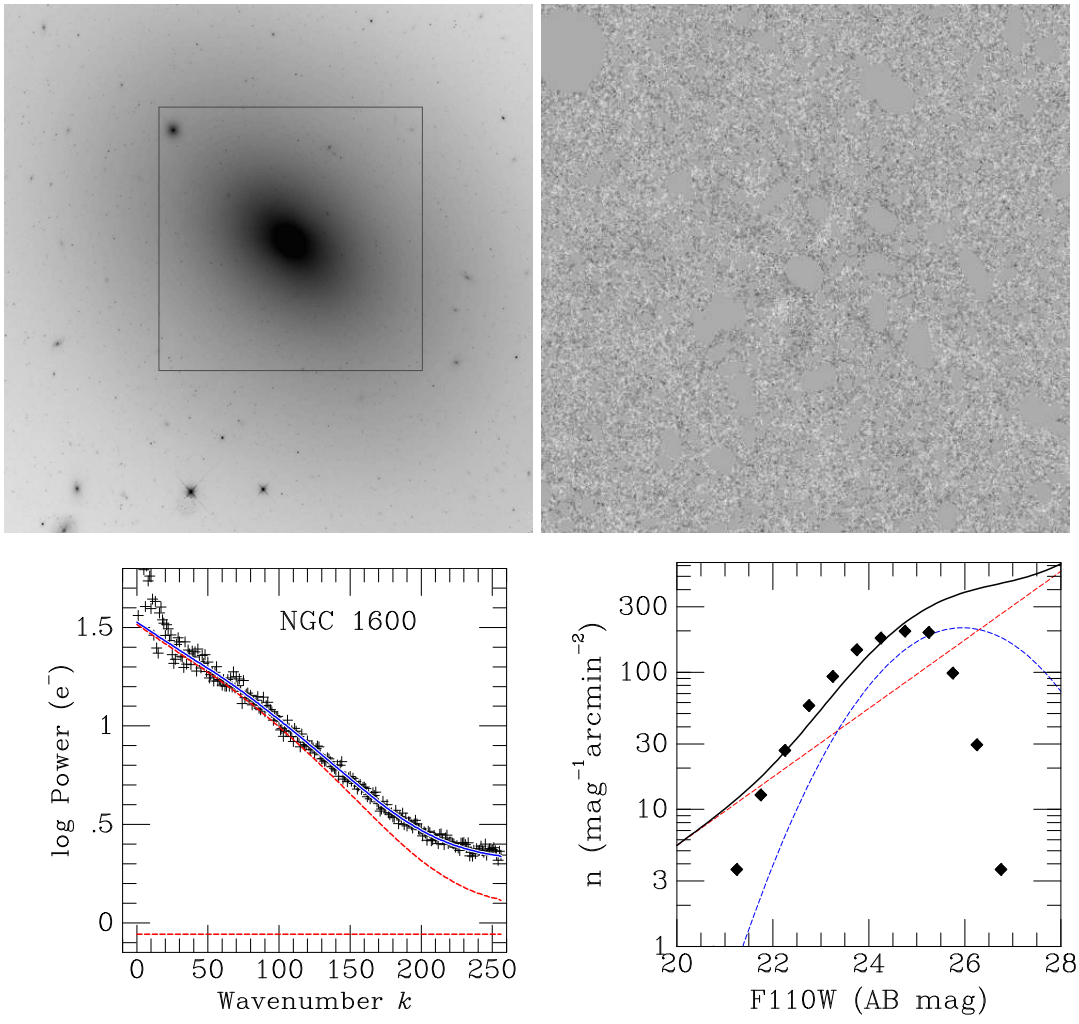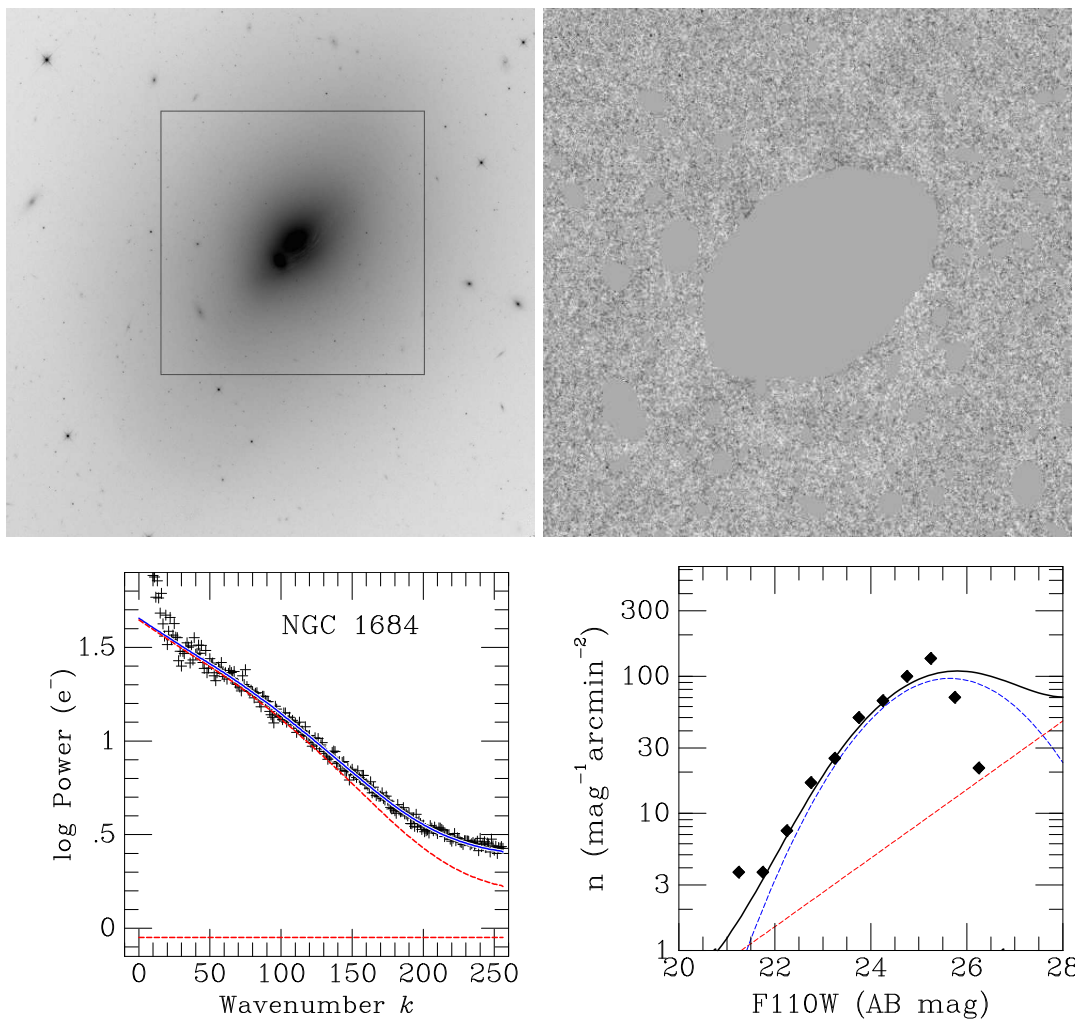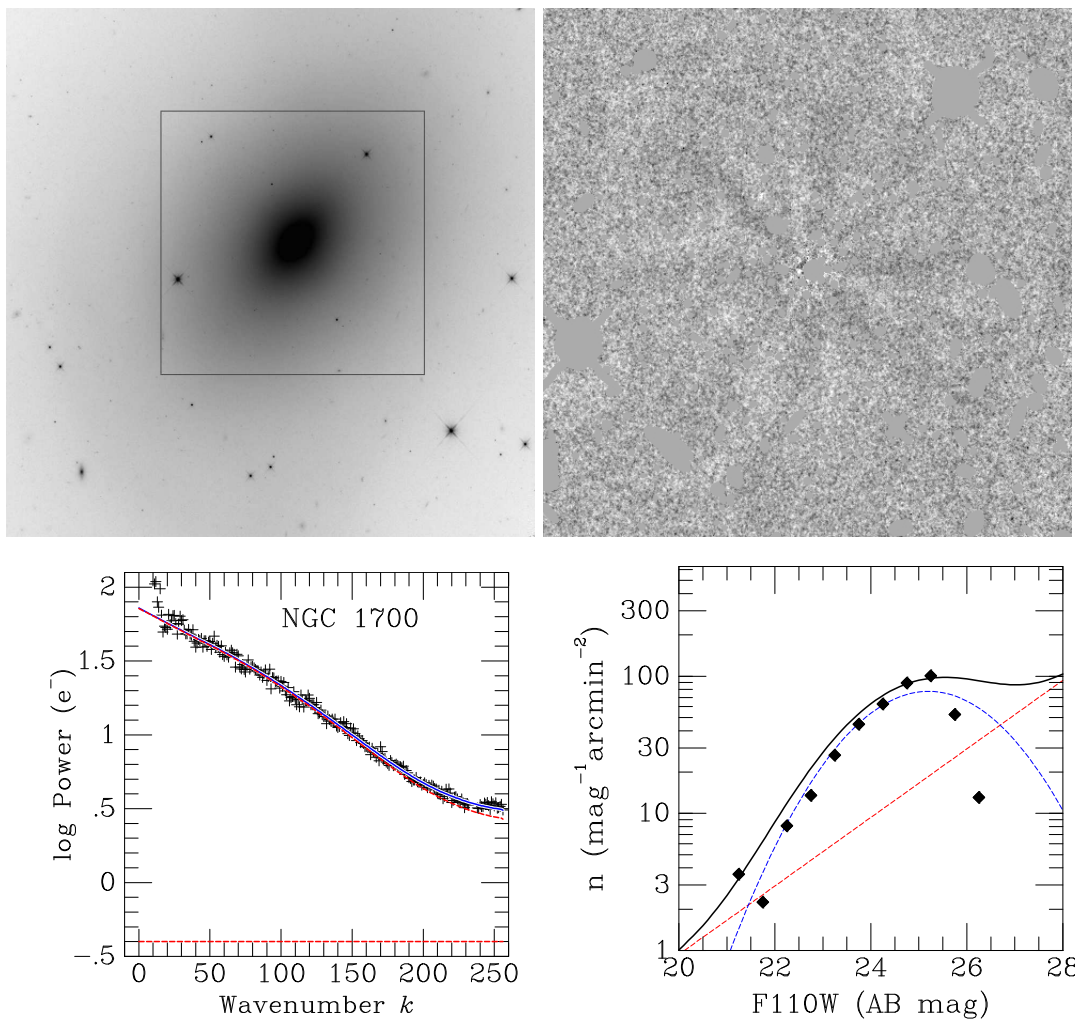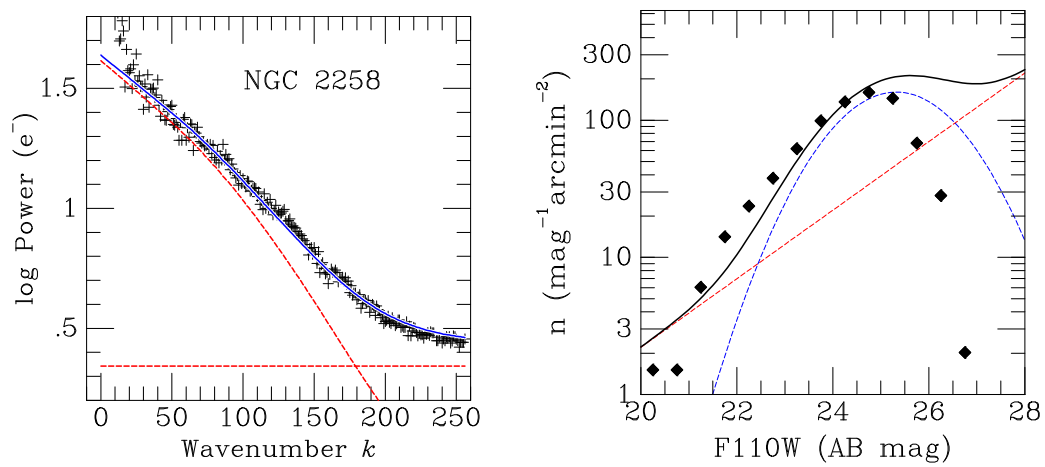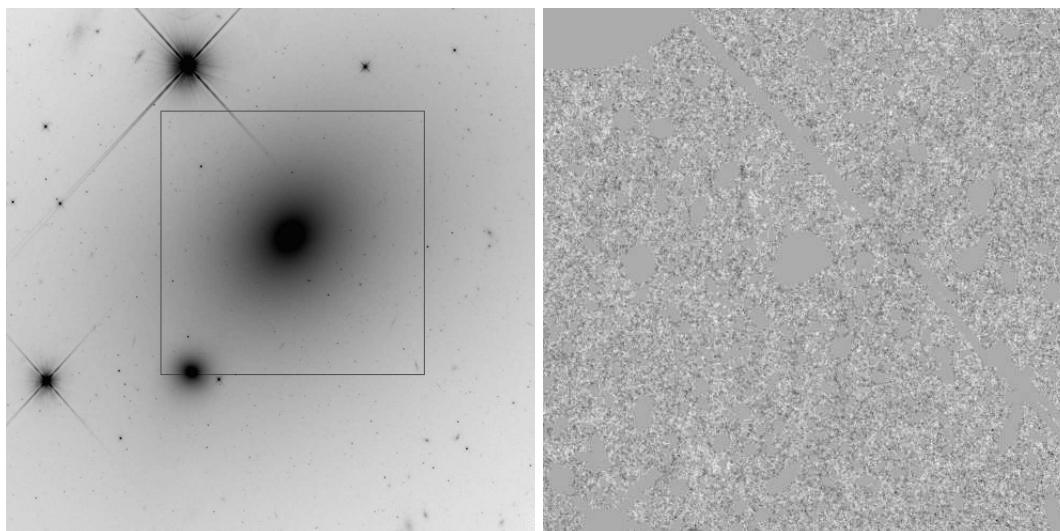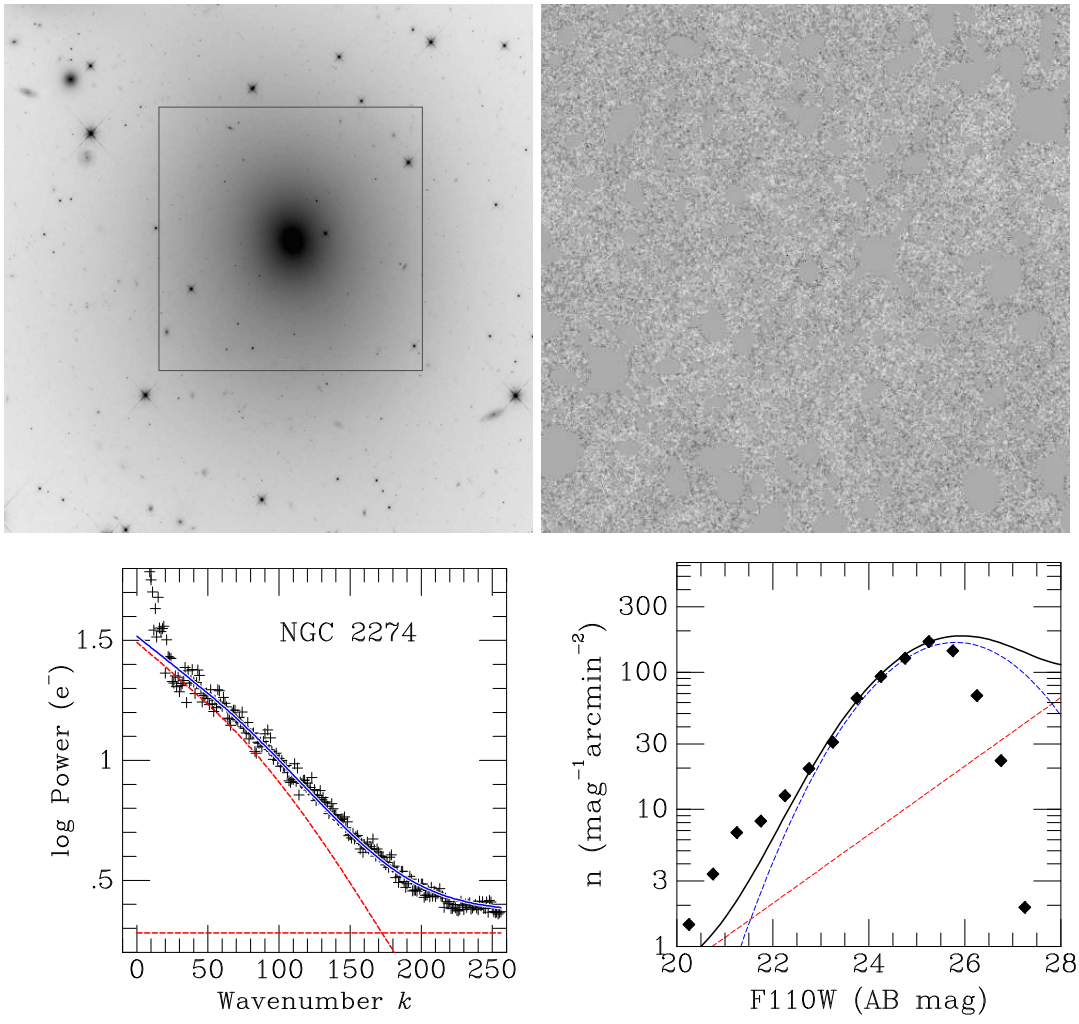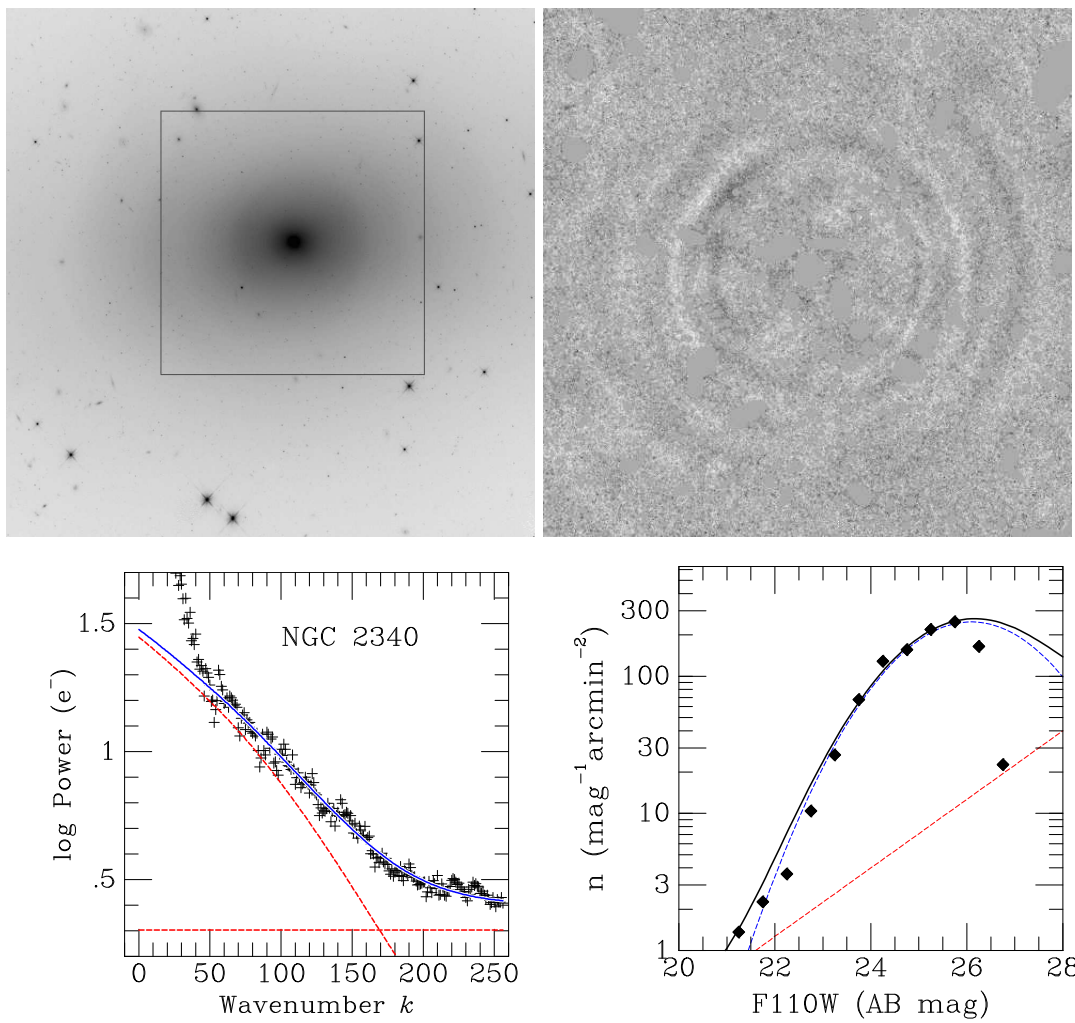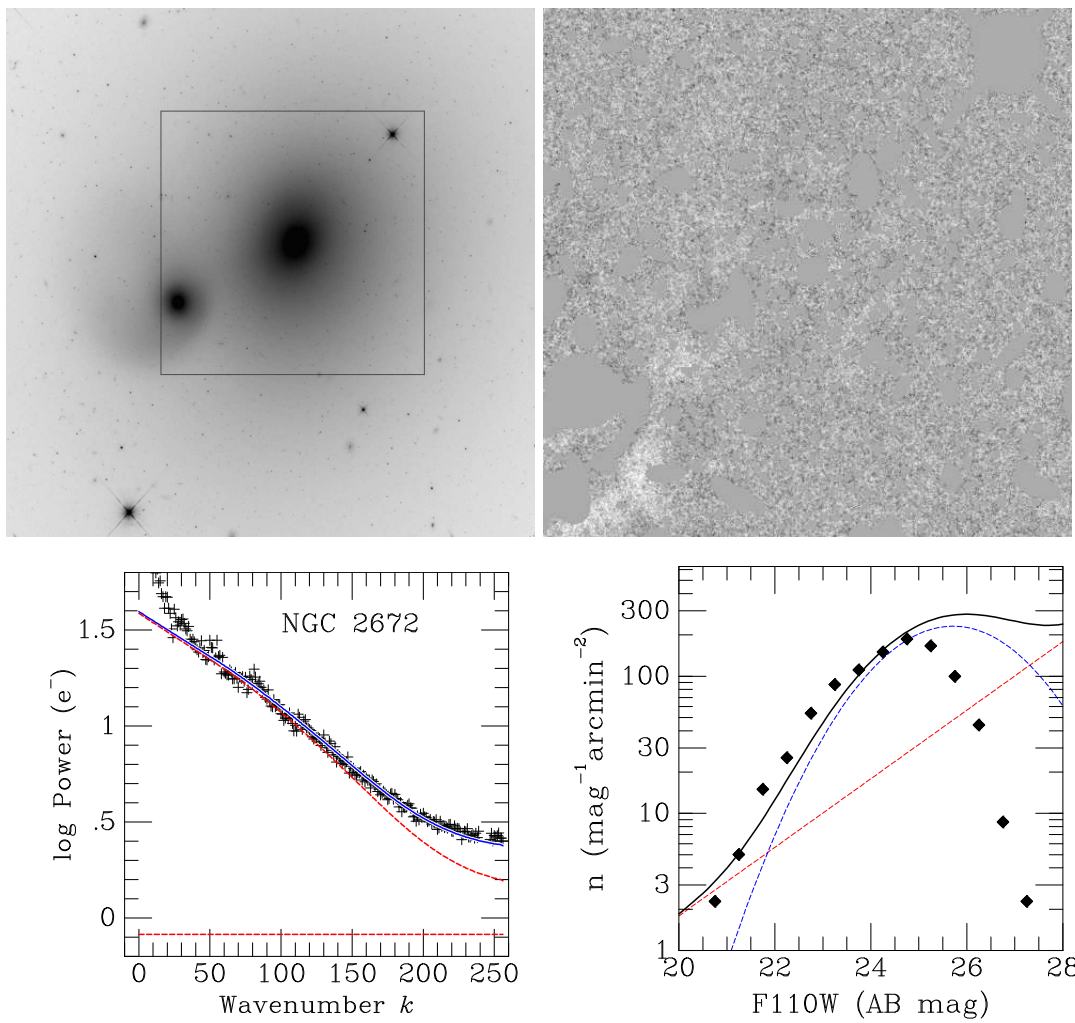**Figure 11.** Combined figure for NGC 383.
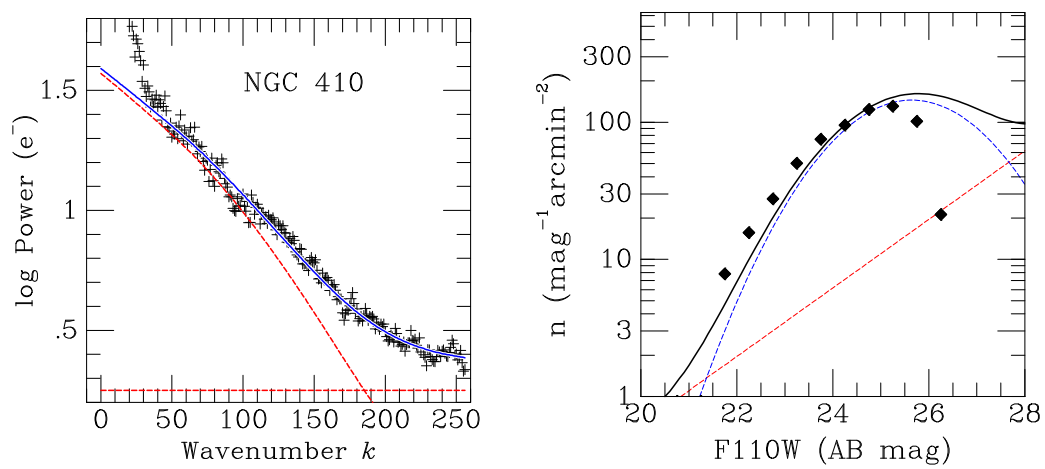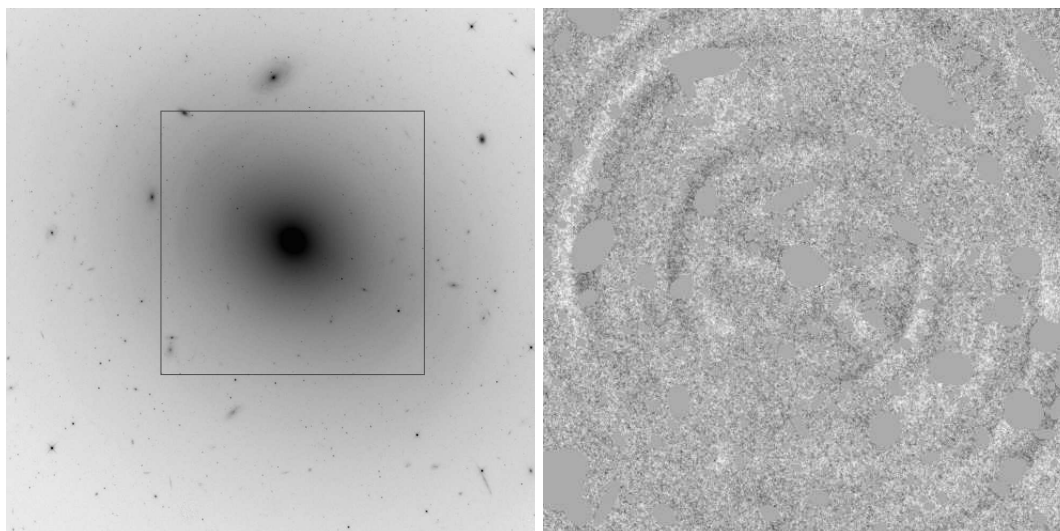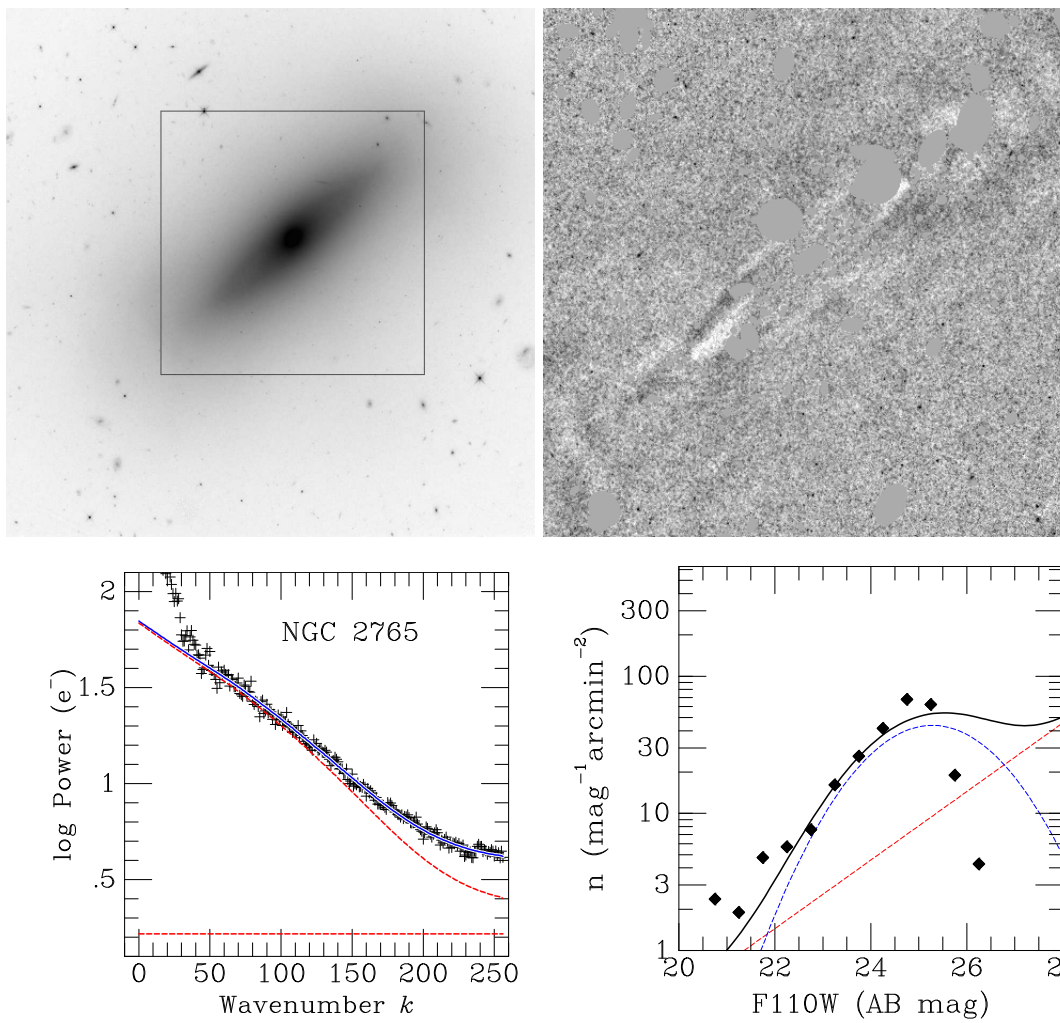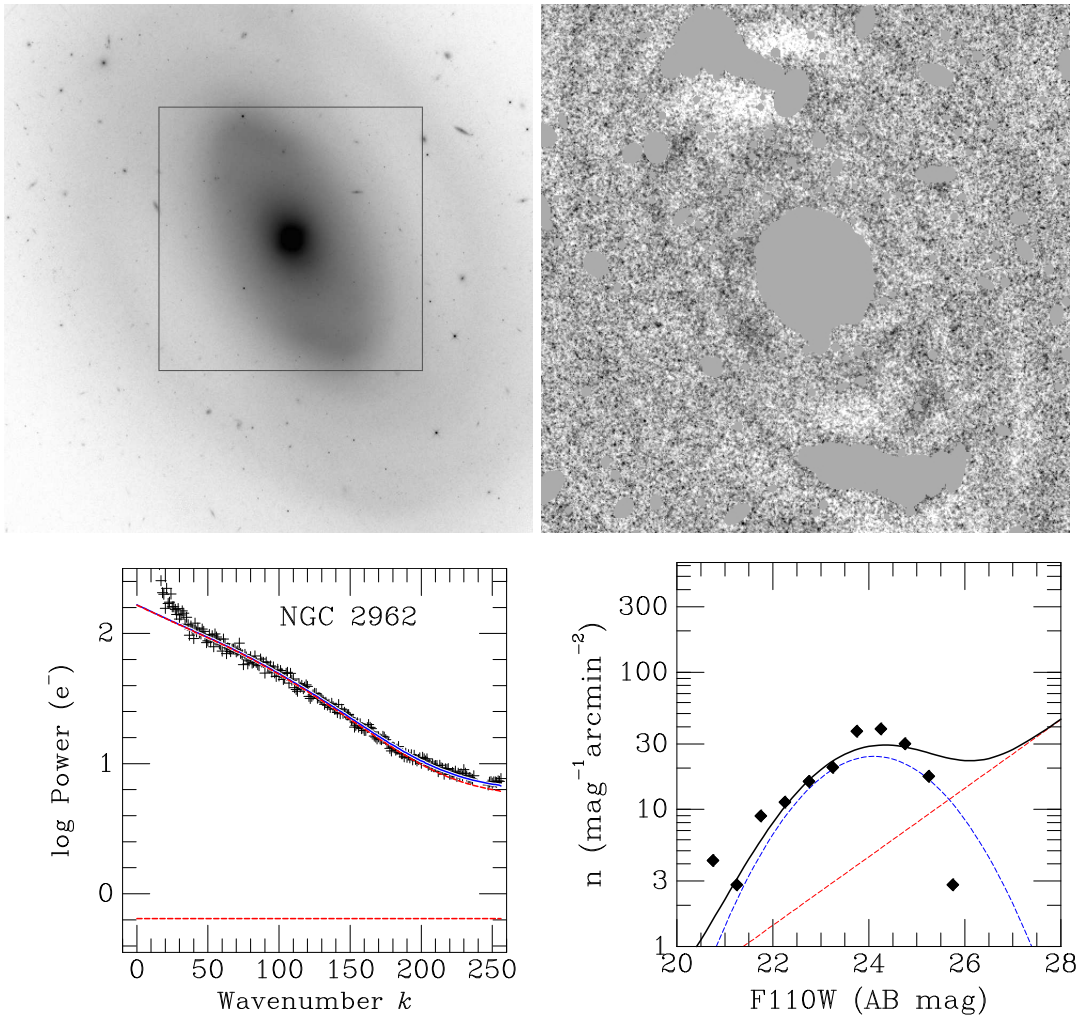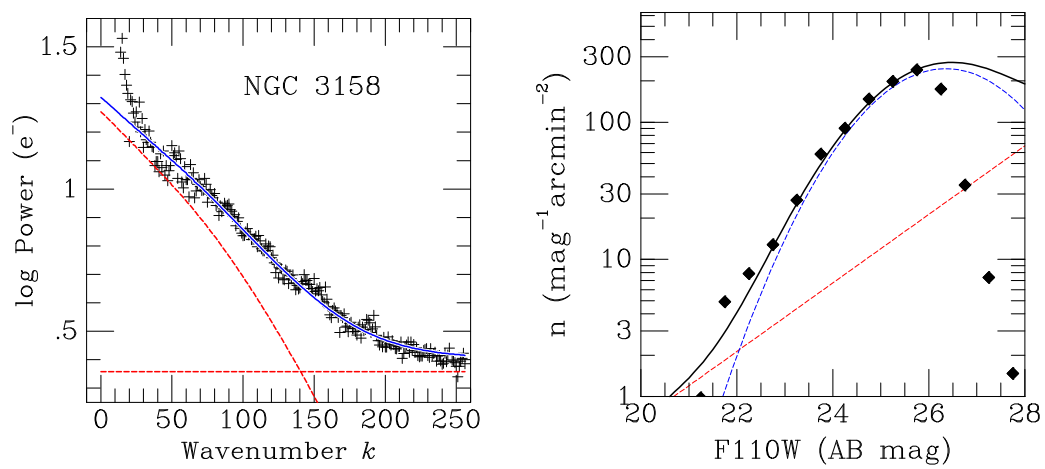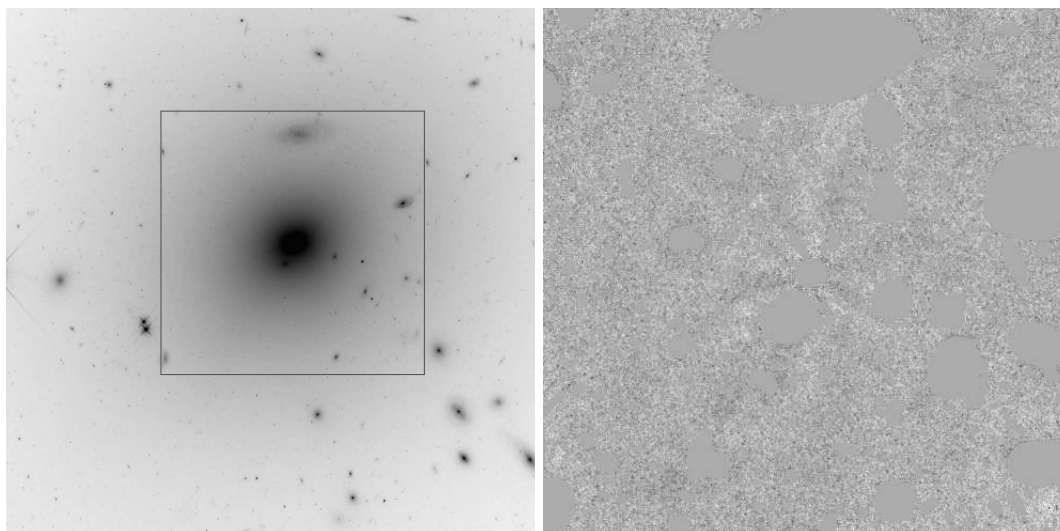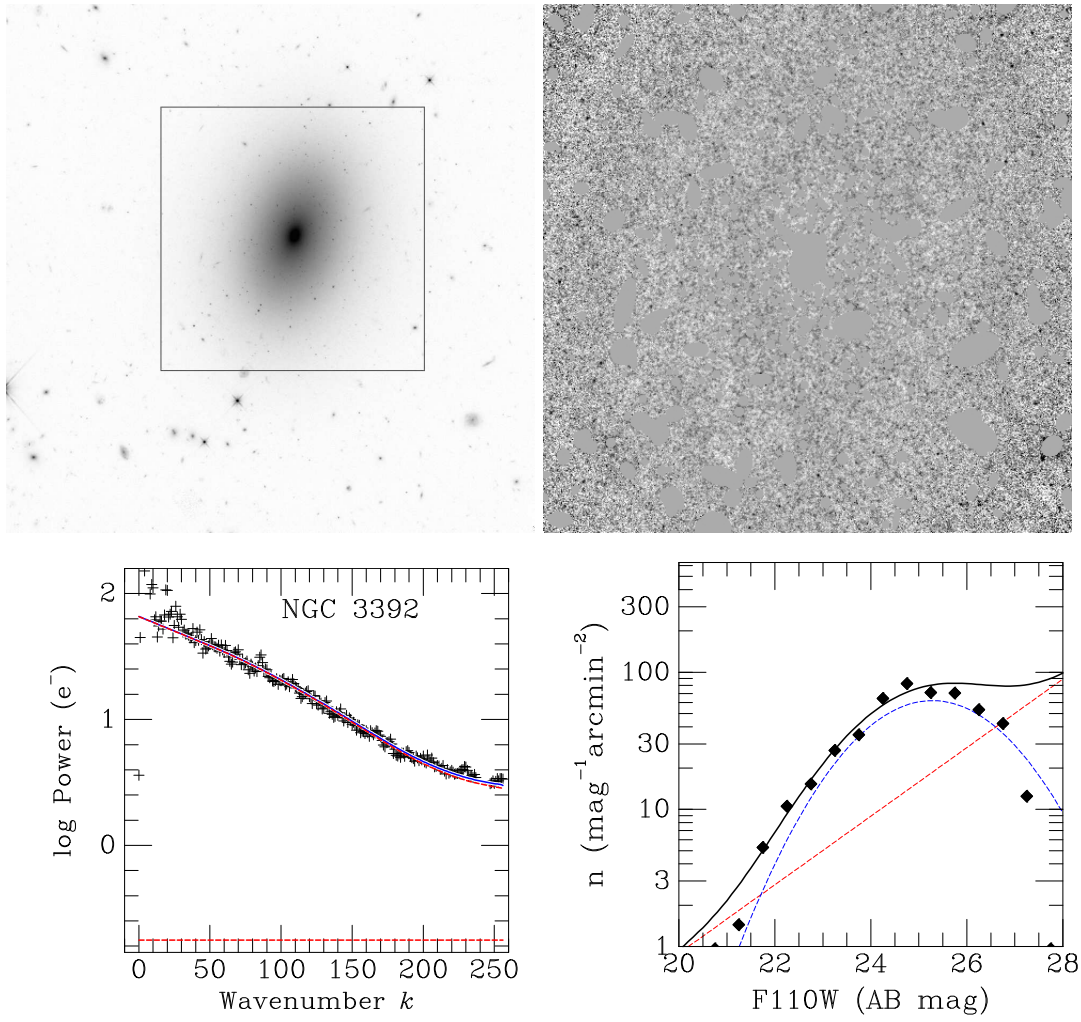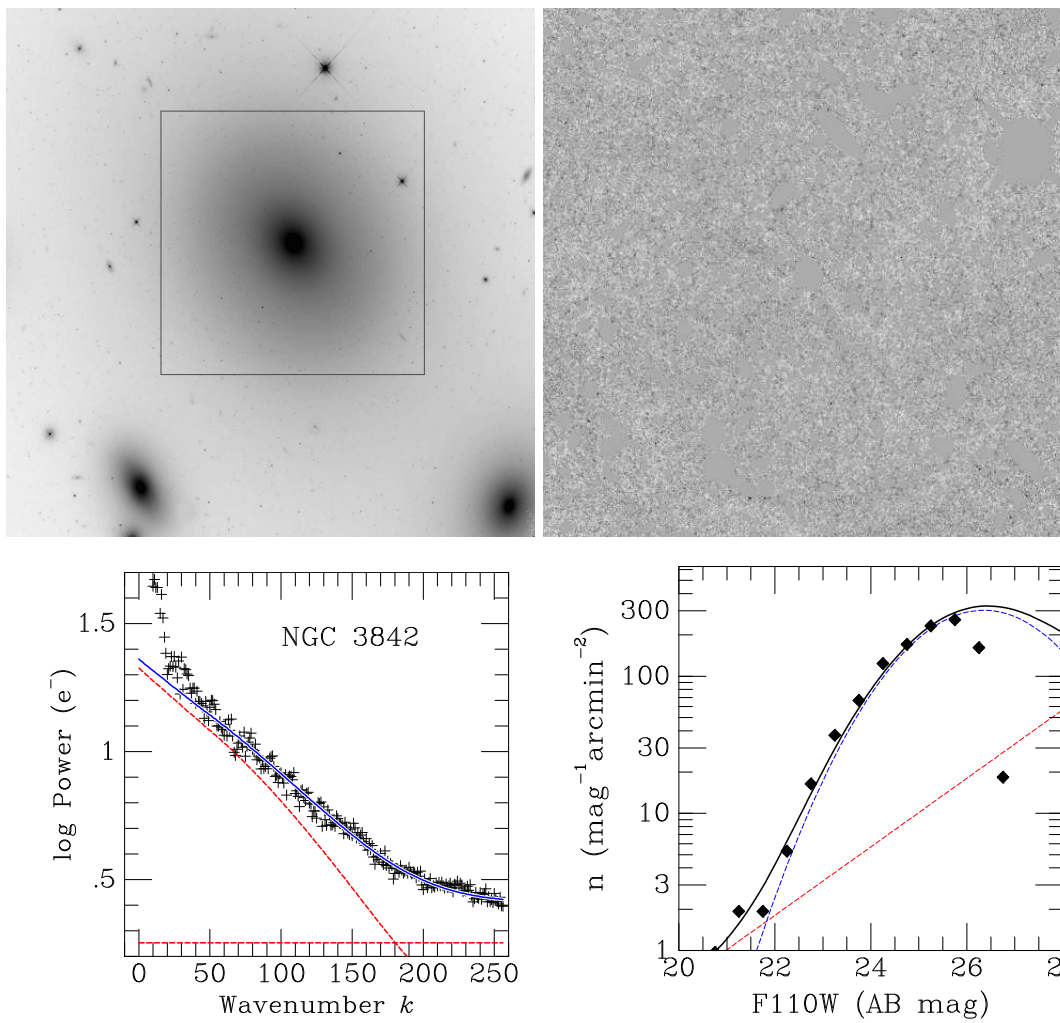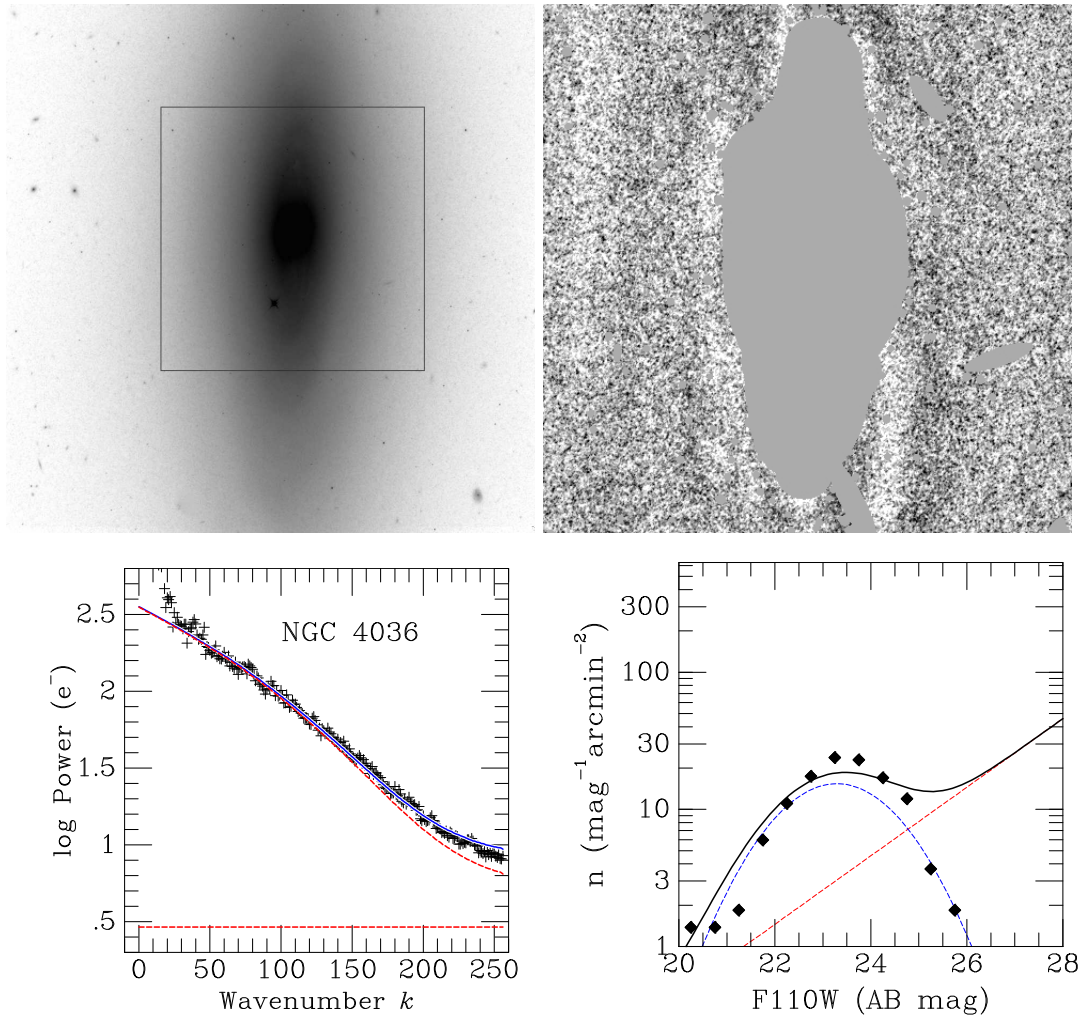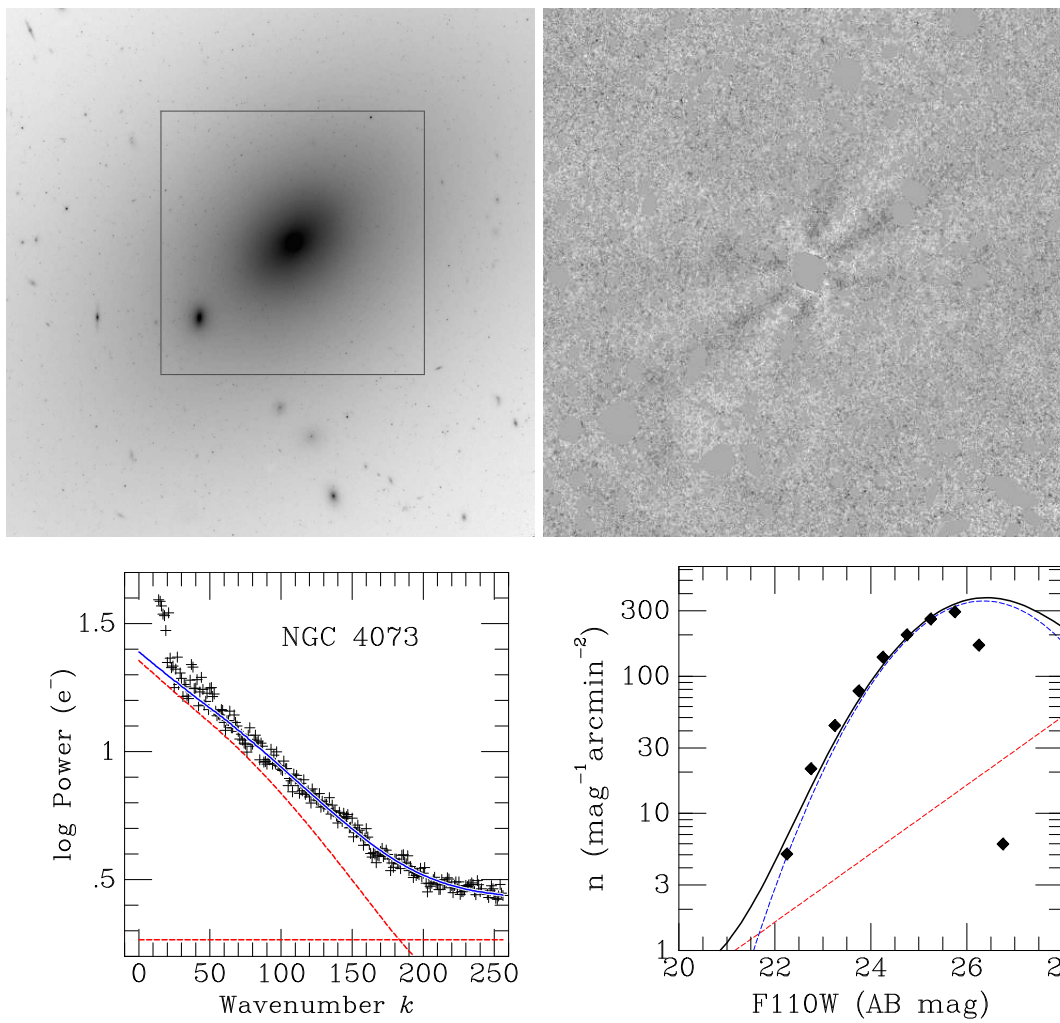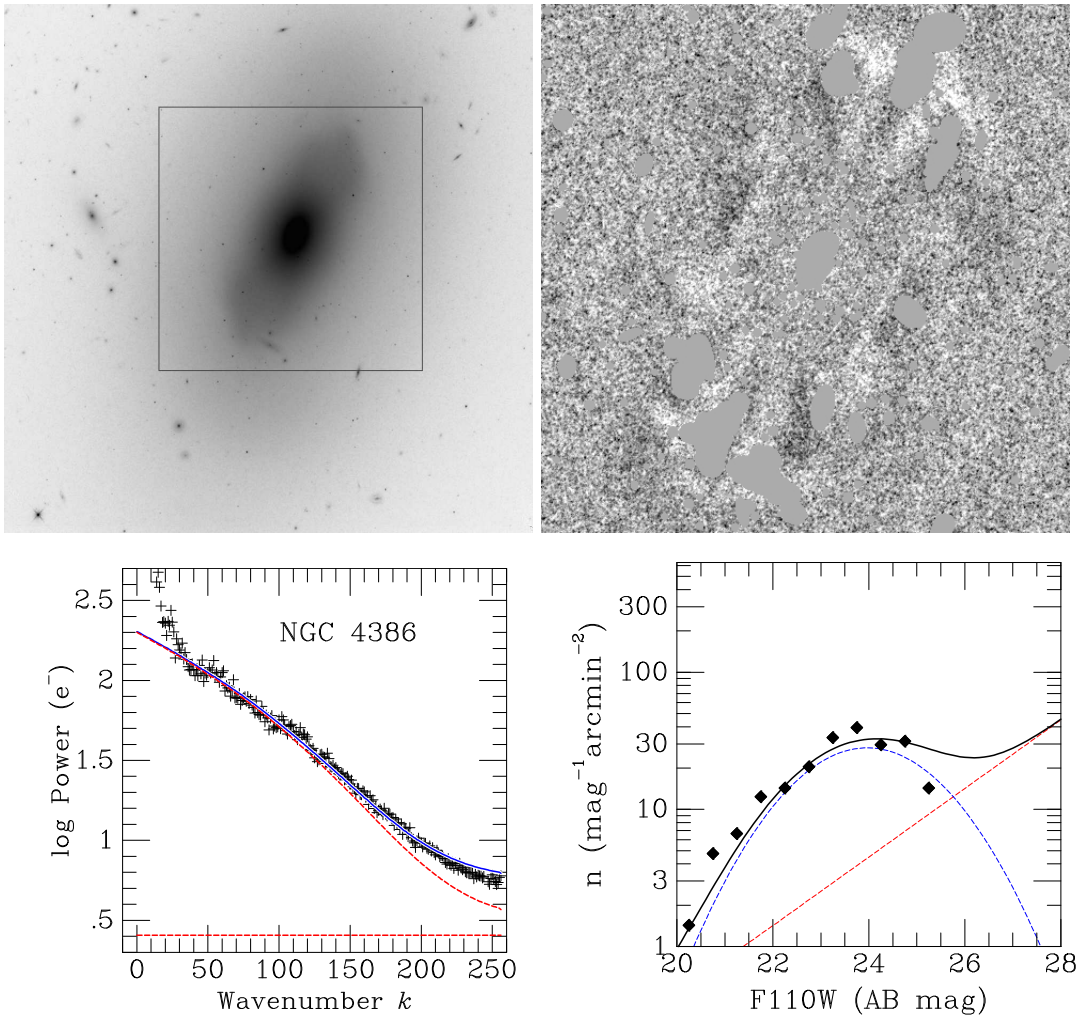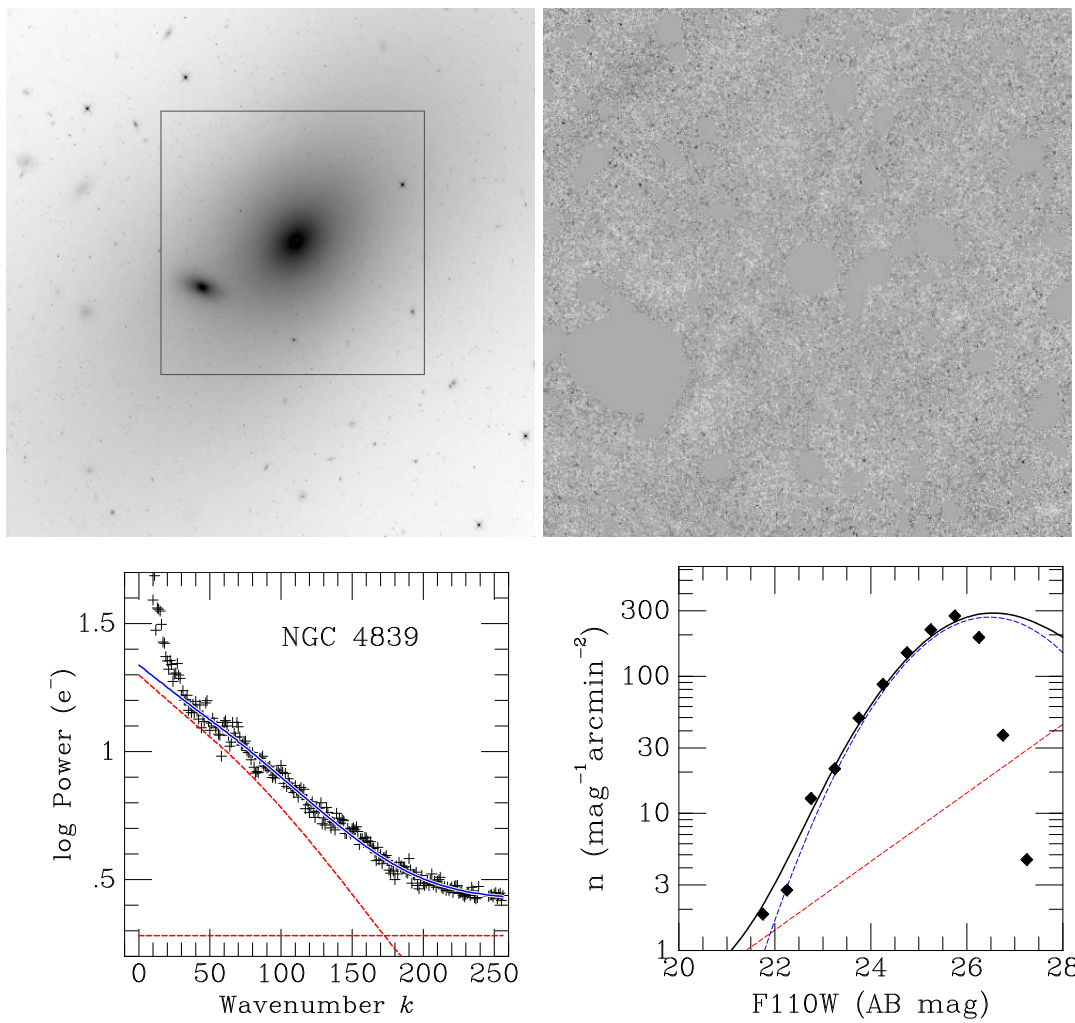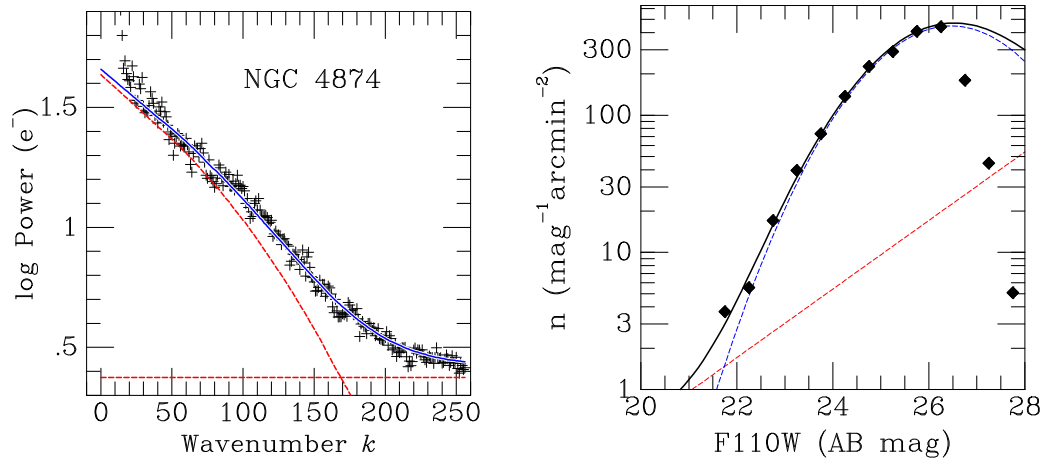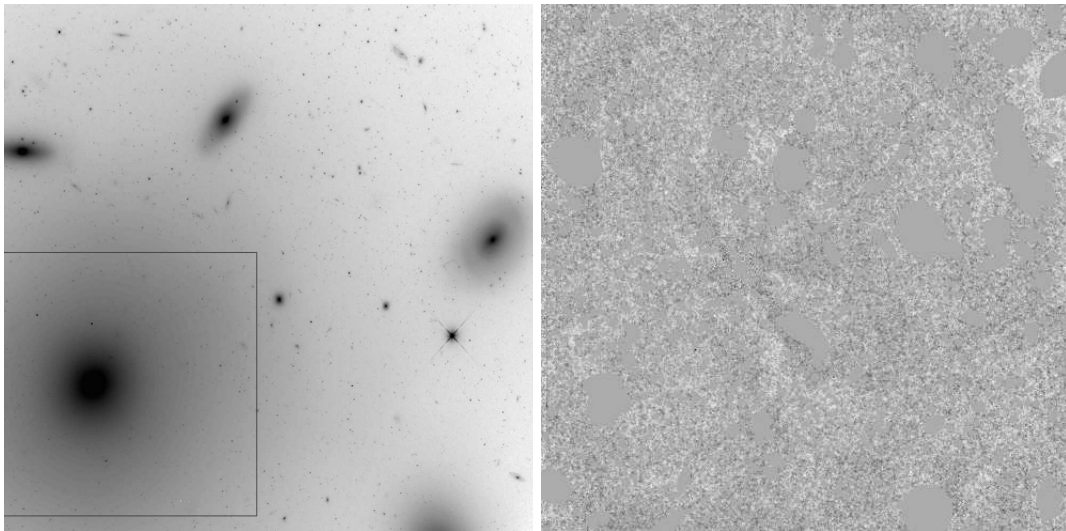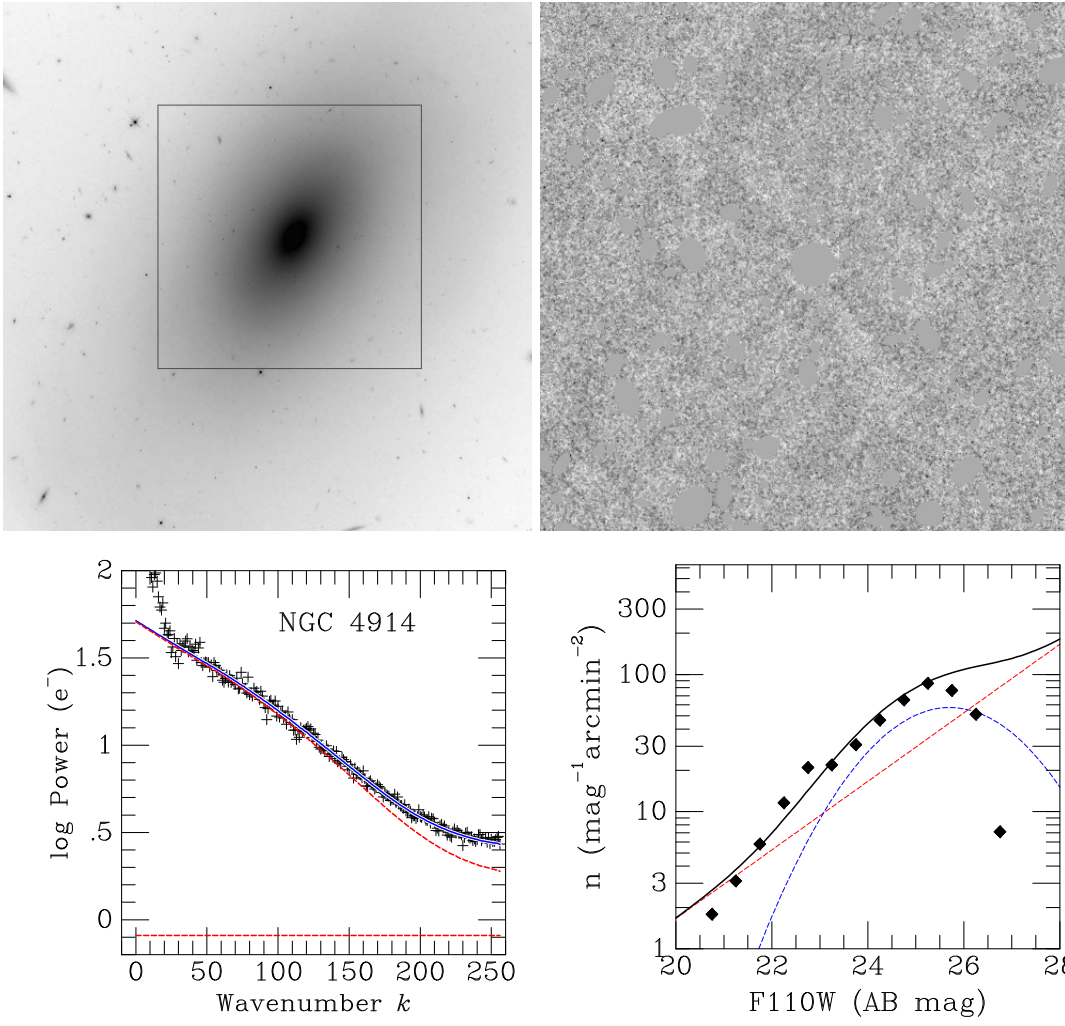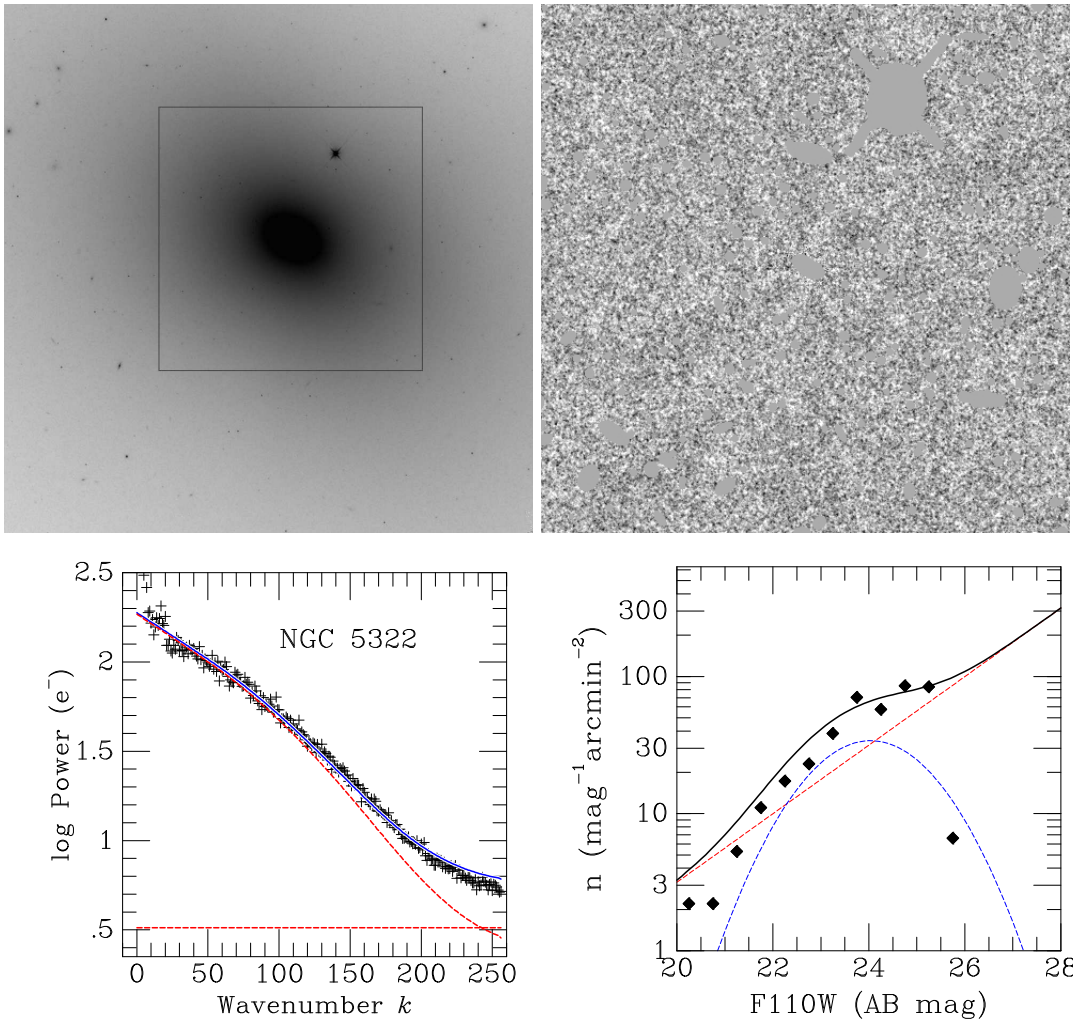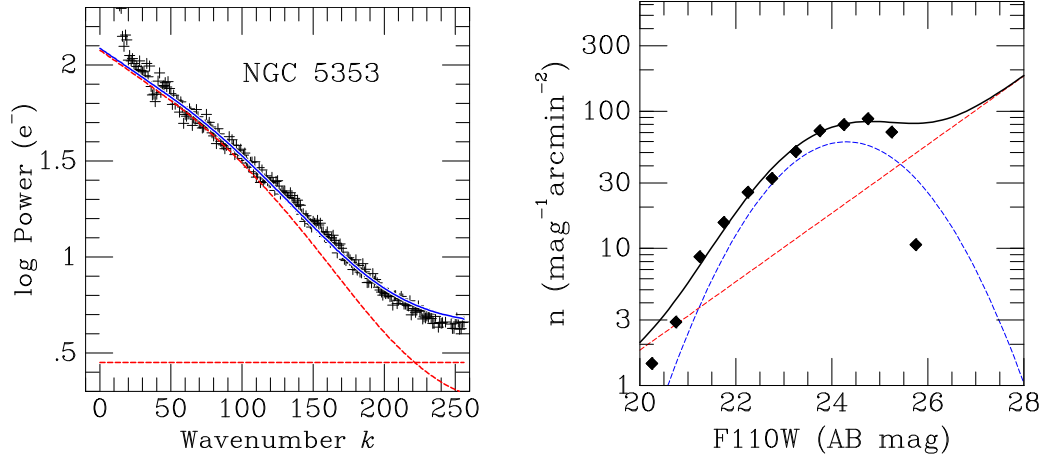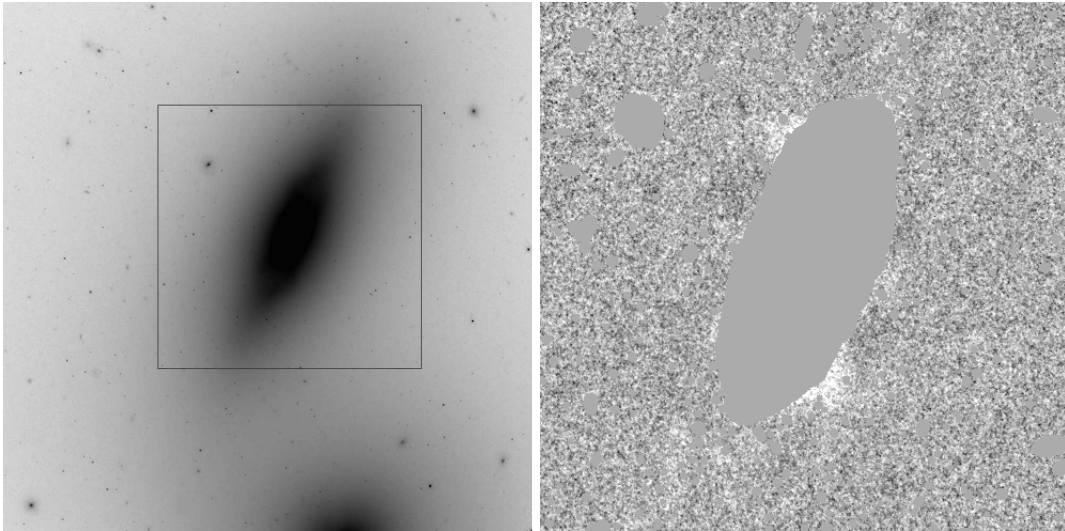
Figure 12. Combined figure for NGC 410.
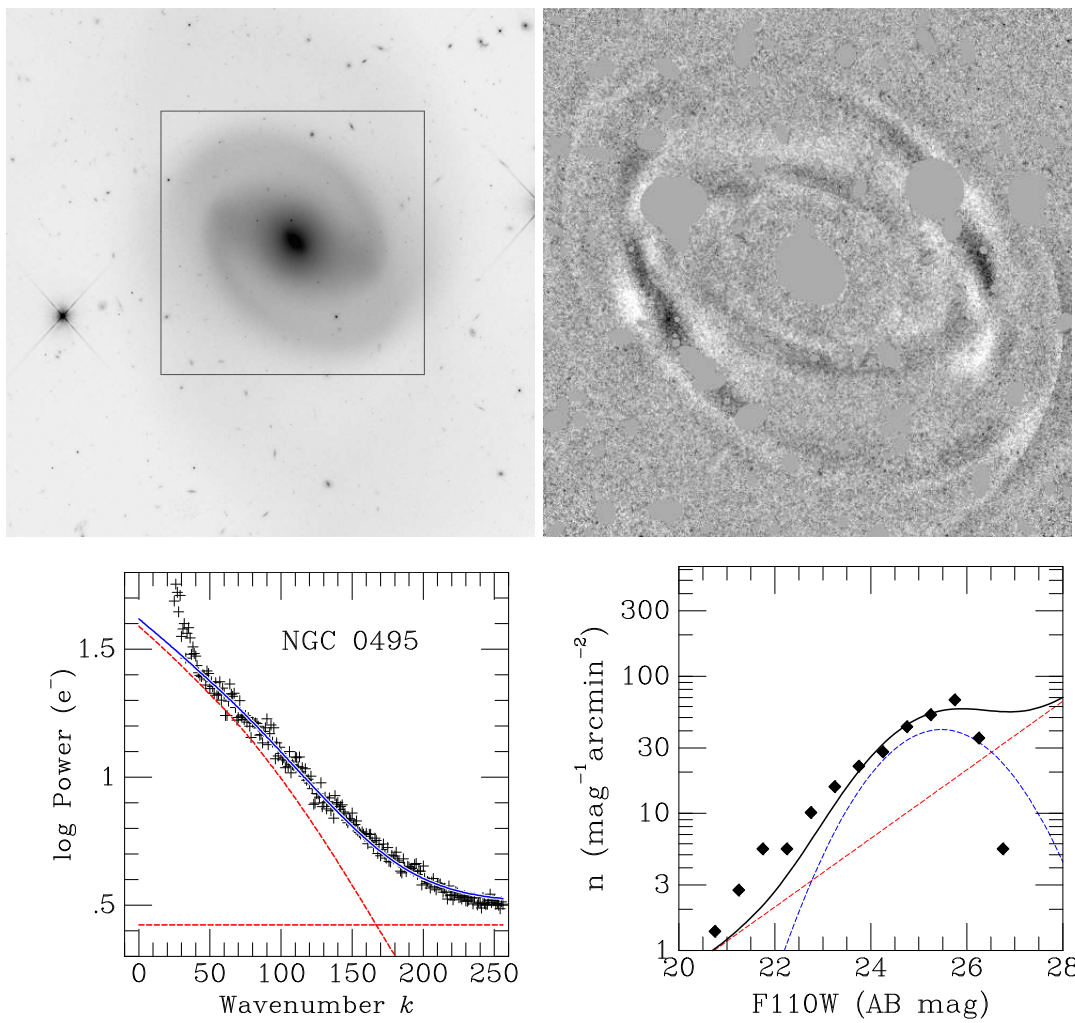
Figure 13. Combined figure for NGC 495.
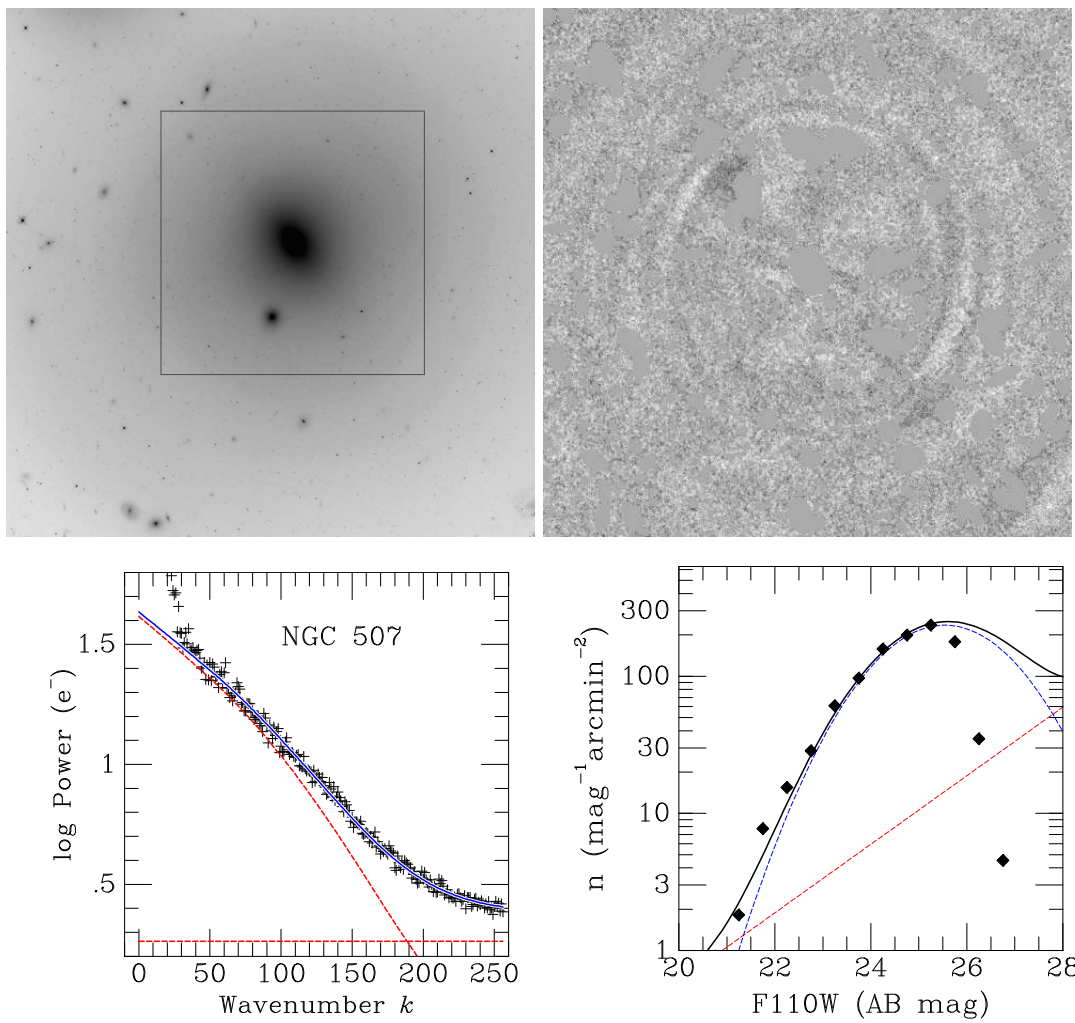
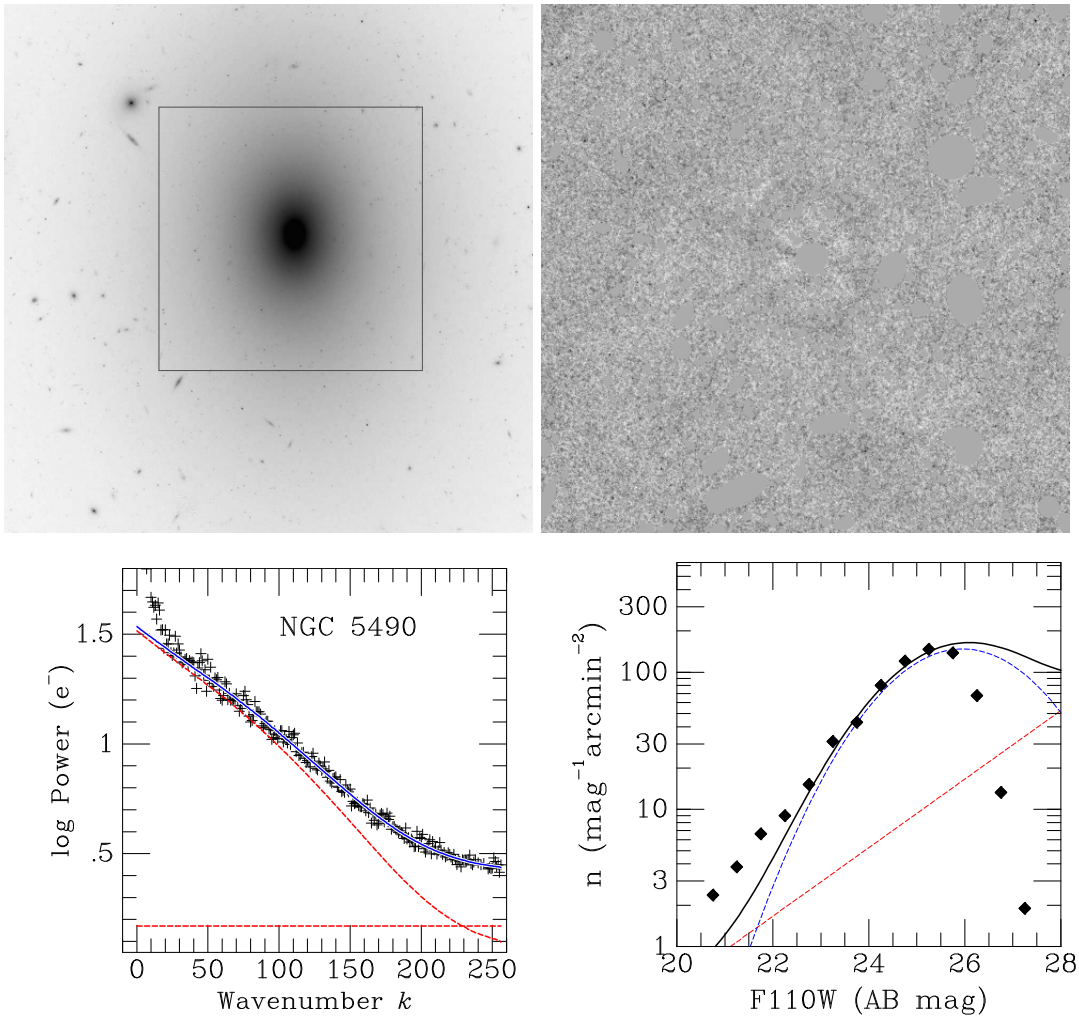**Figure 14.** Combined figure for NGC 507.
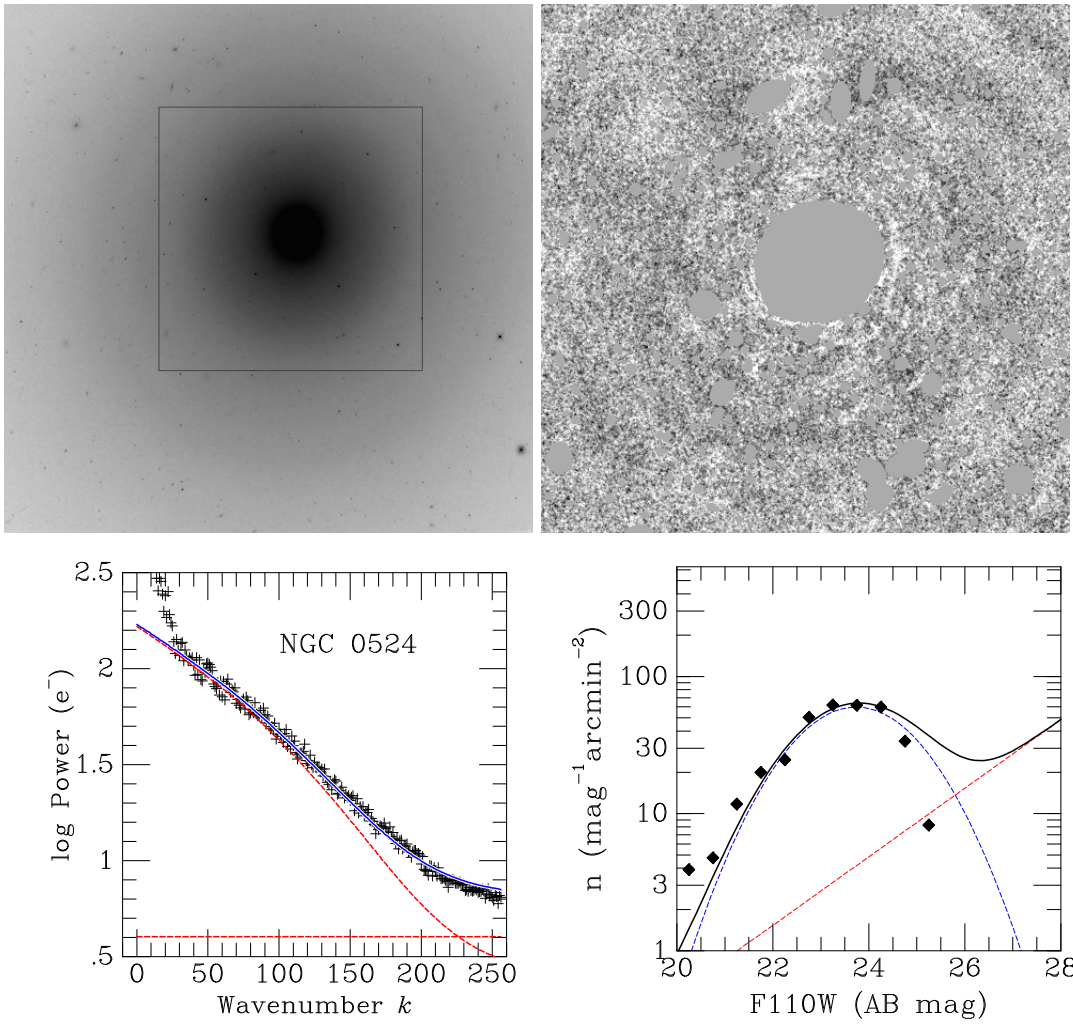
Figure 15. Combined figure for NGC 524.
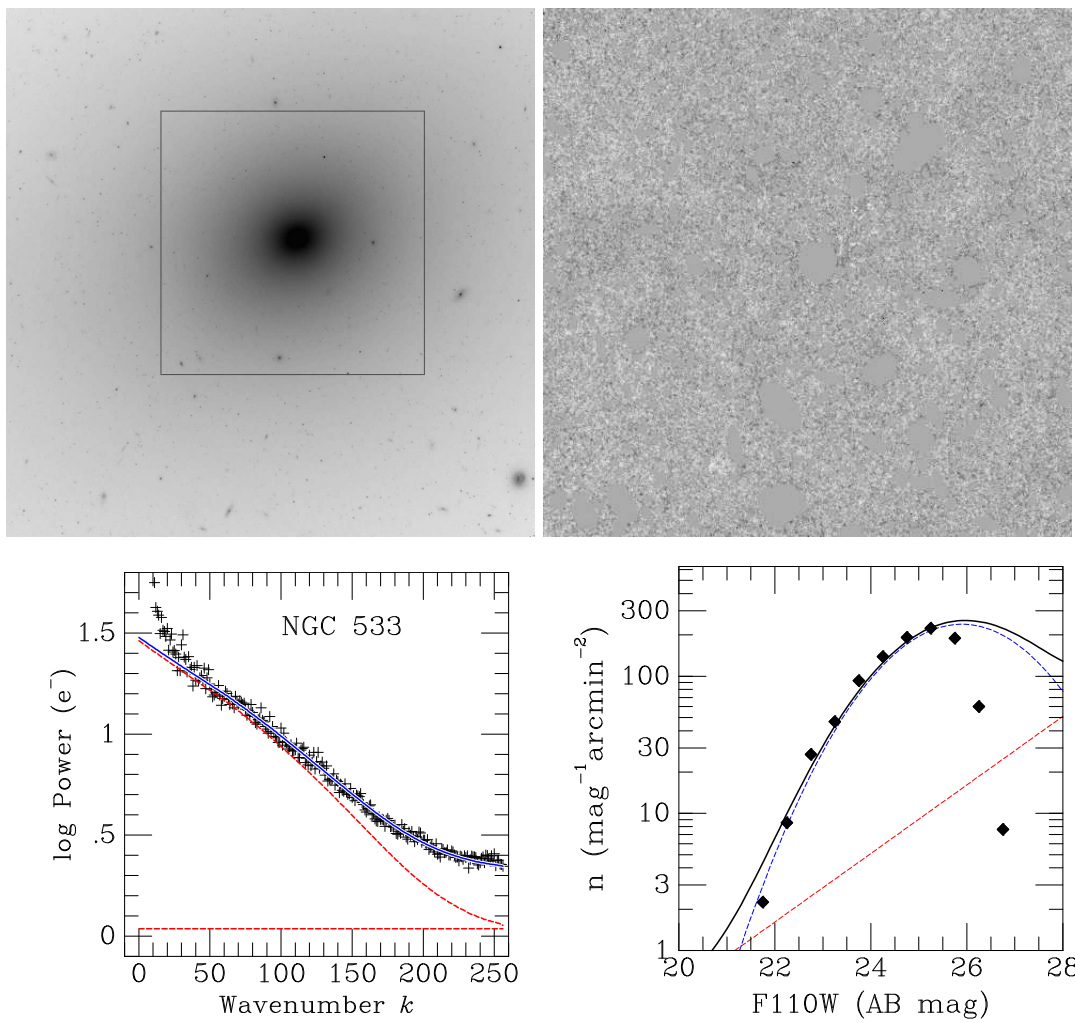
Figure 16. Combined figure for NGC 533.
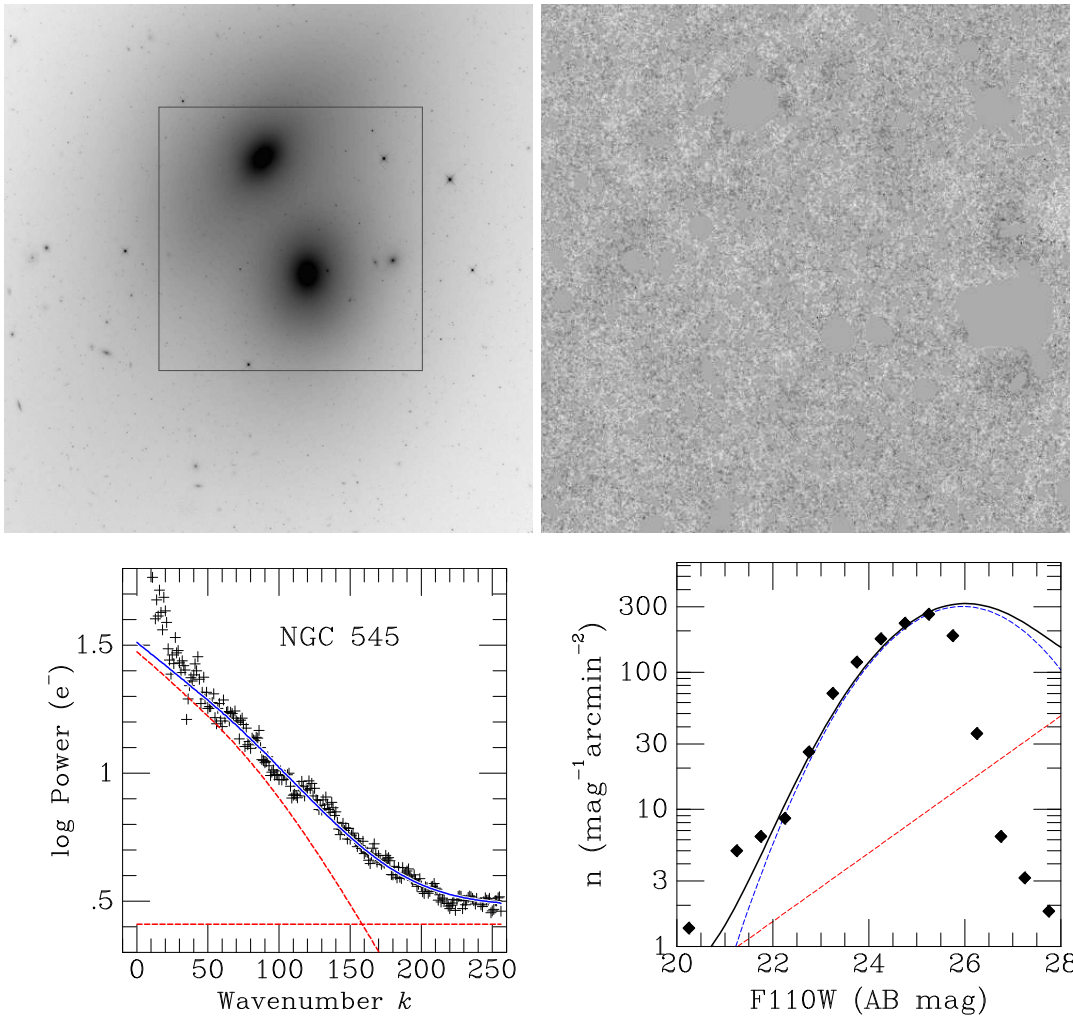
Figure 17. Combined figure for NGC 545 (top; NGC 547 is also visible.)
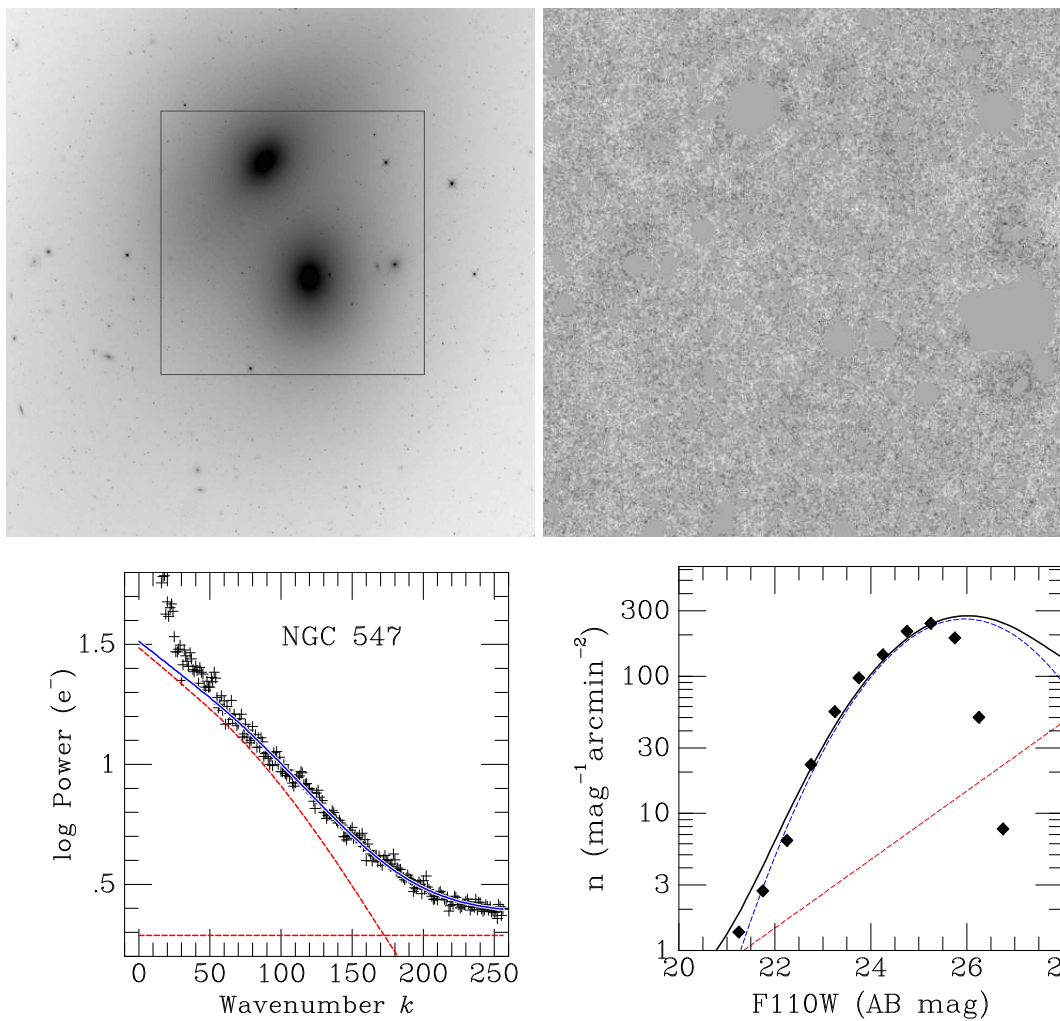
Figure 18. Combined figure for NGC 547. (bottom; NGC 545 is also visible.)
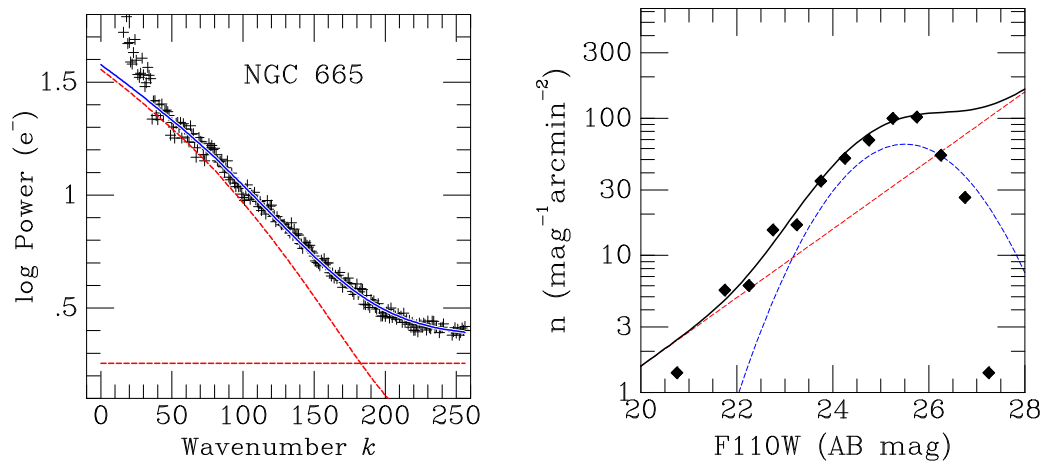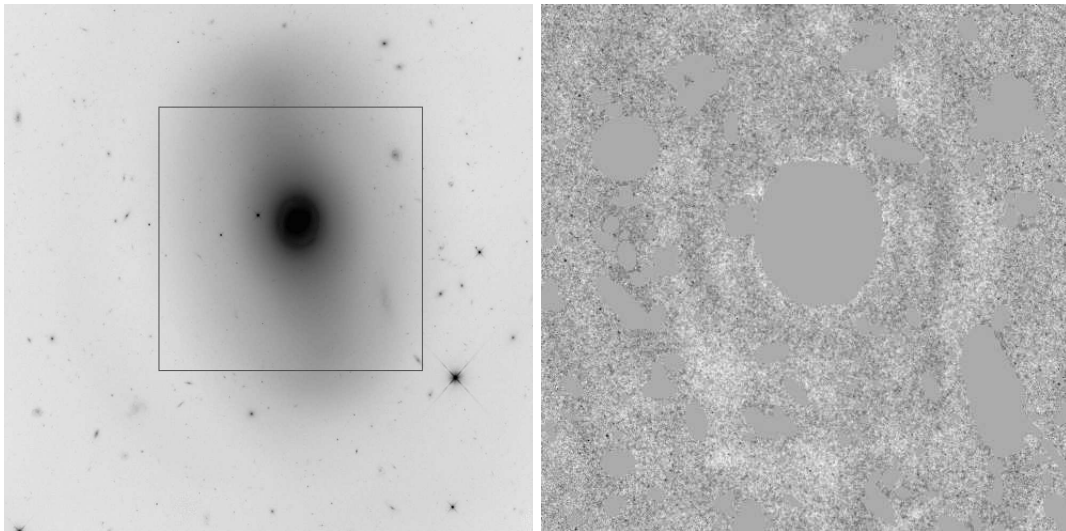
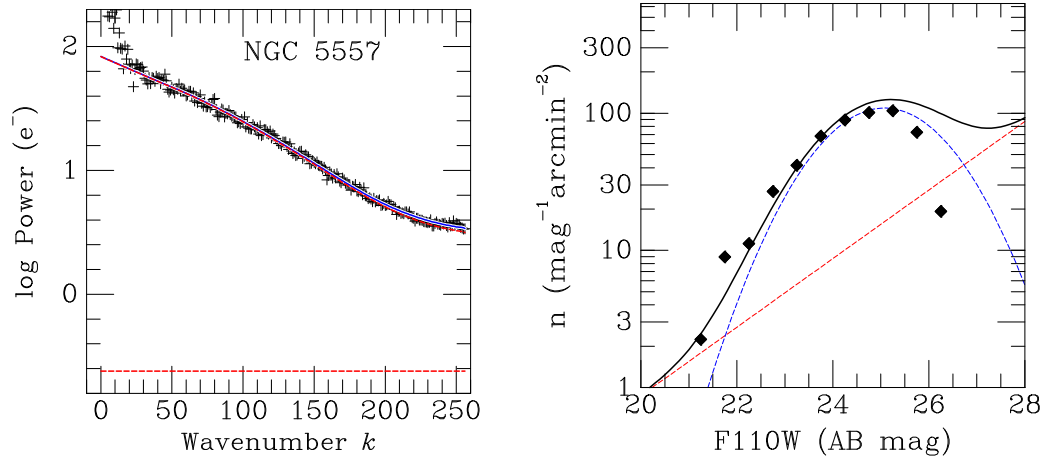**Figure 19.** Combined figure for NGC 665.
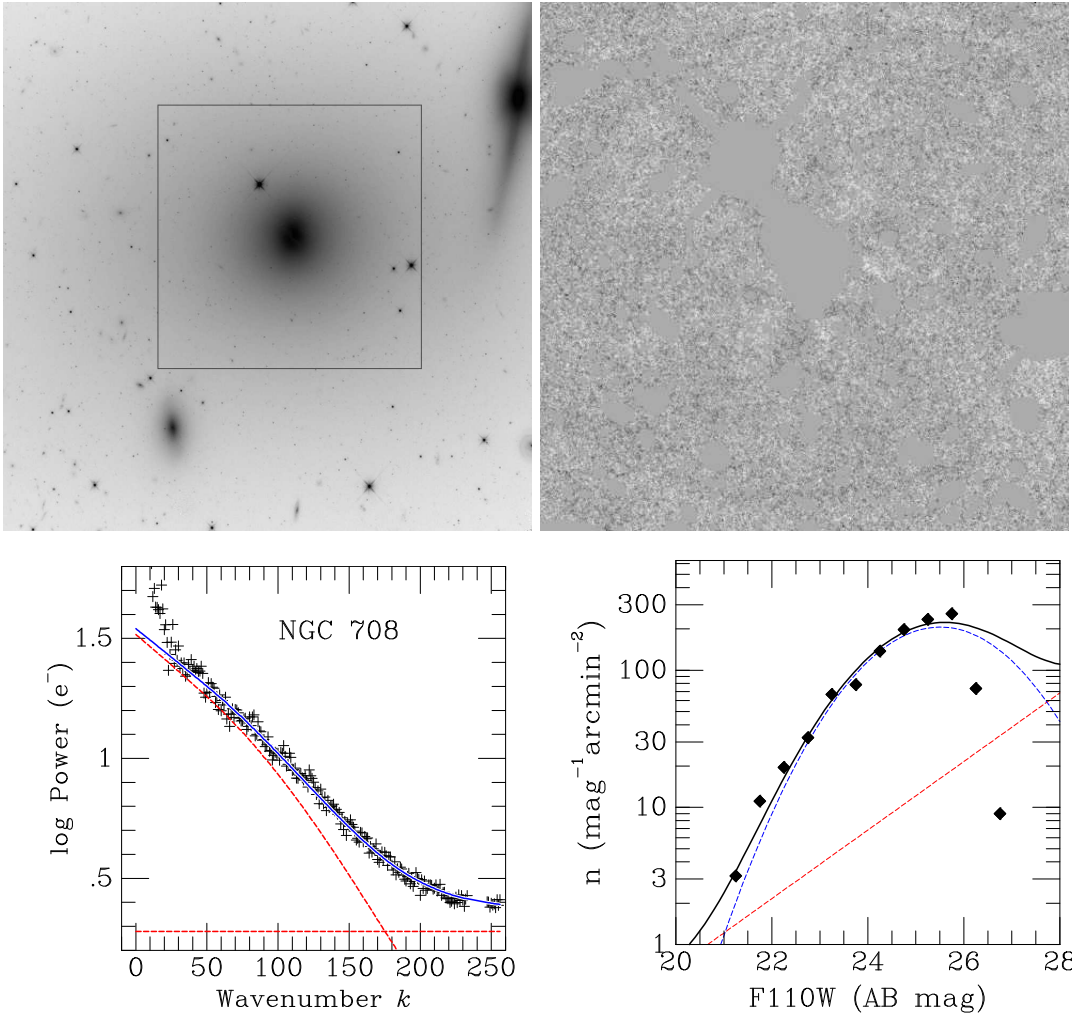
Figure 20. Combined figure for NGC 708.
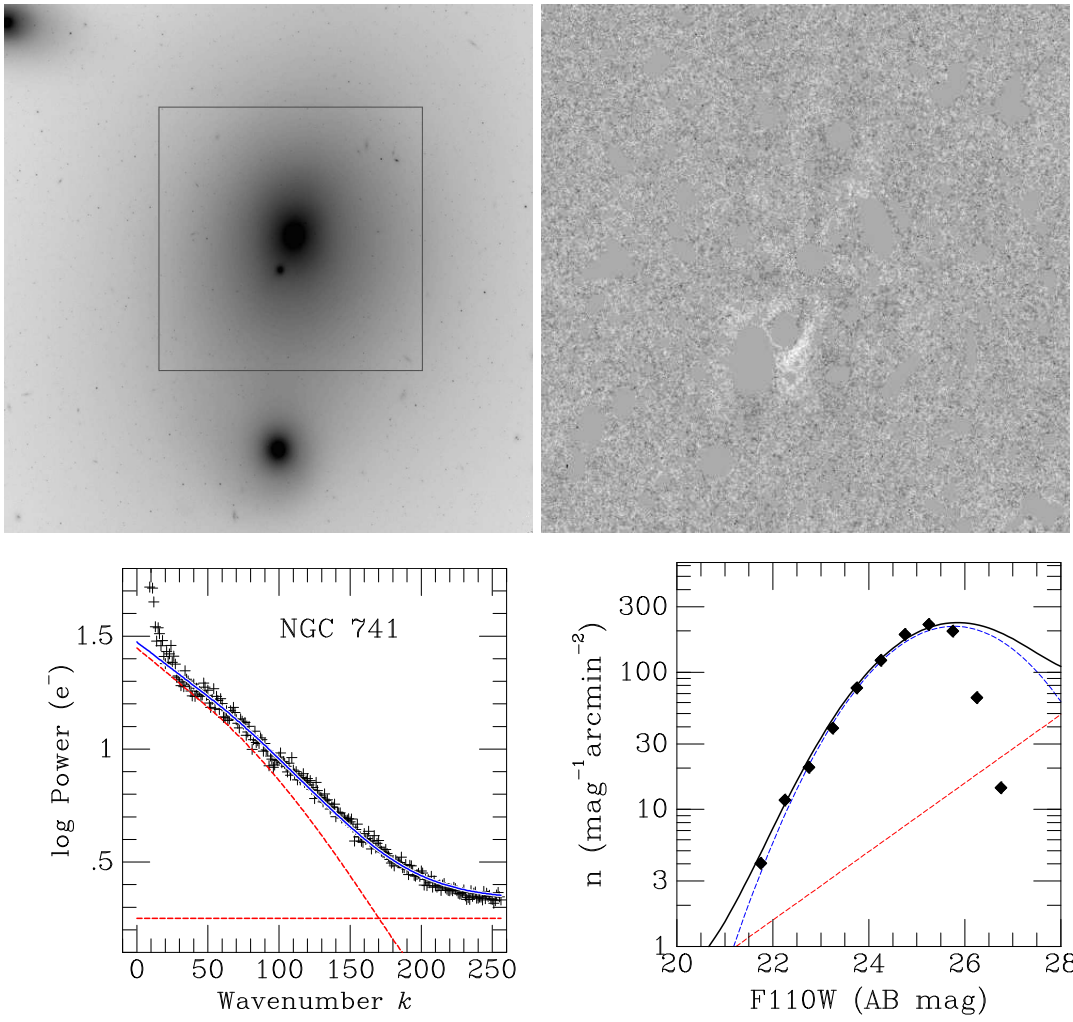
Figure 21. Combined figure for NGC 741.
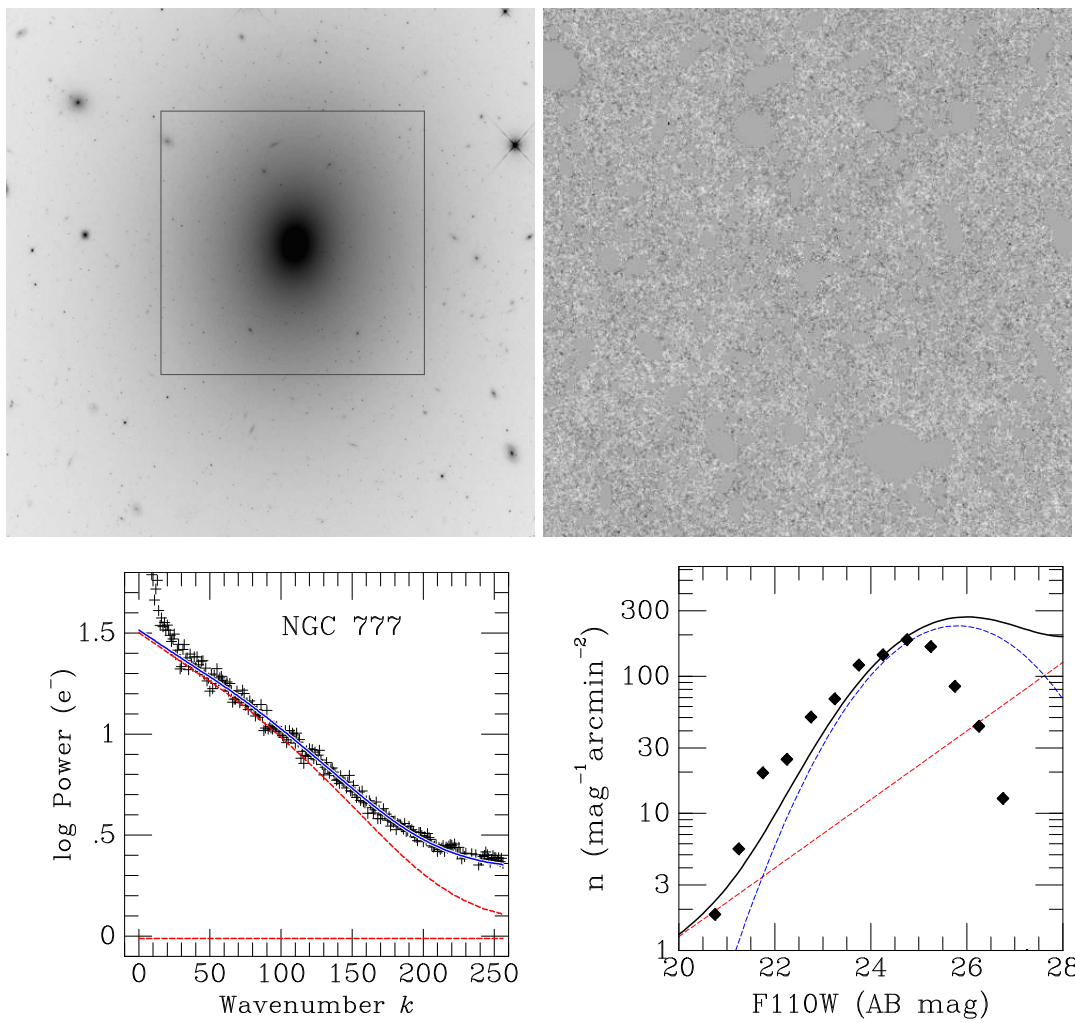
Figure 22. Combined figure for NGC 777.
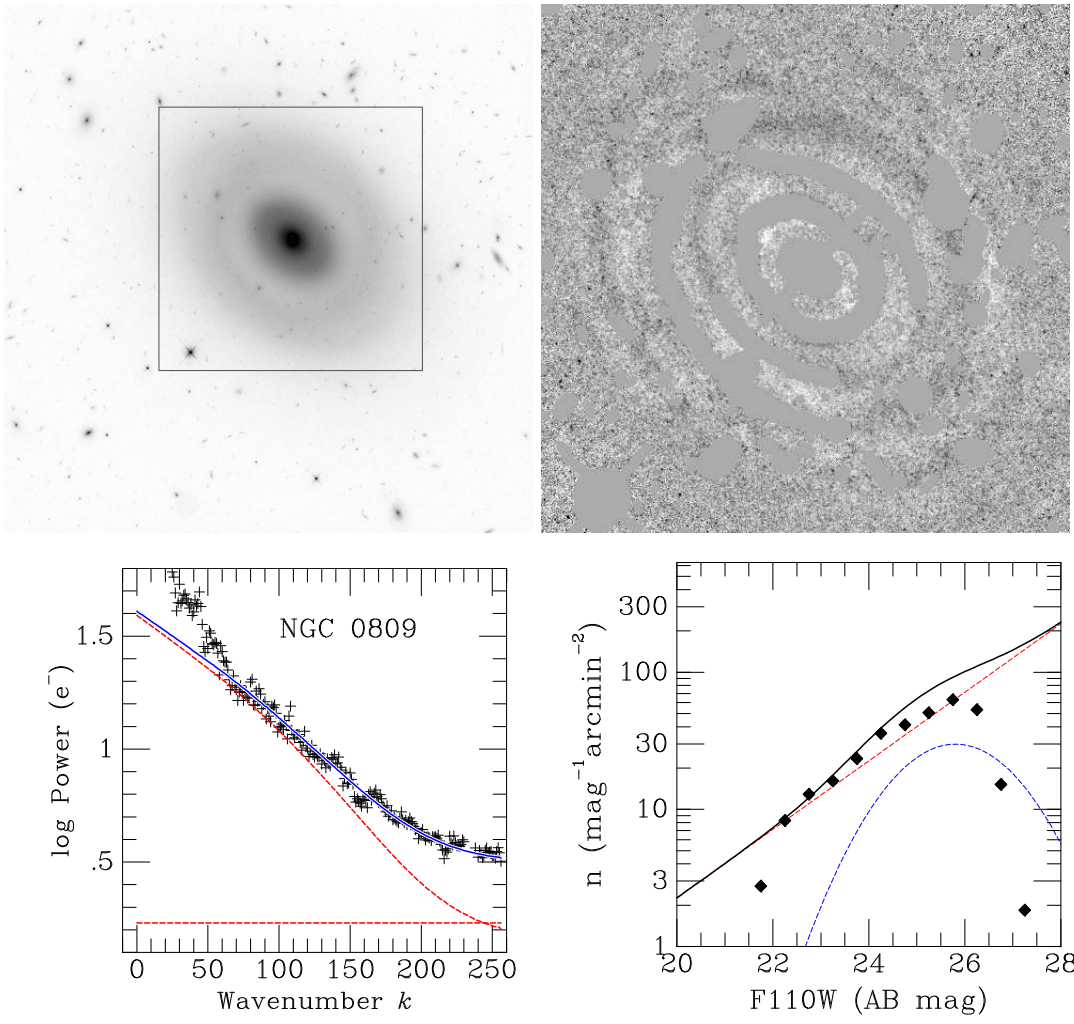
Figure 23. Combined figure for NGC 809.
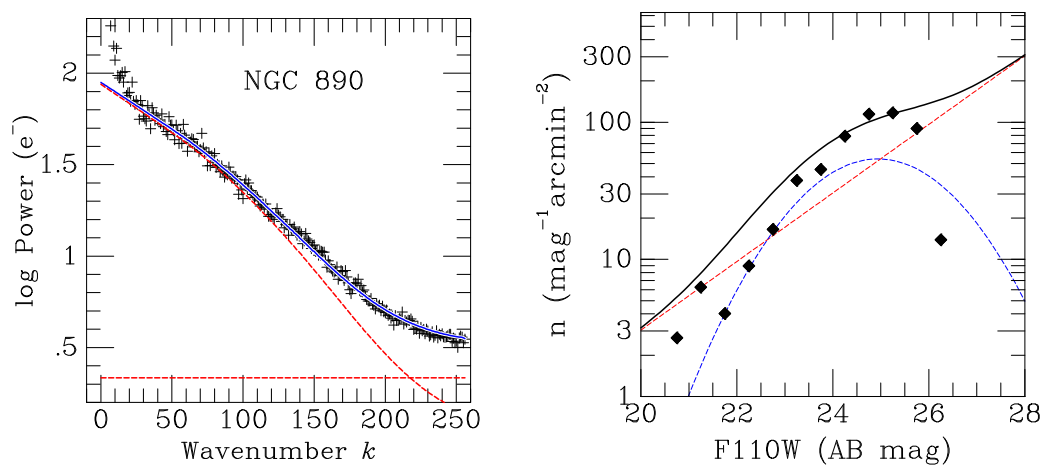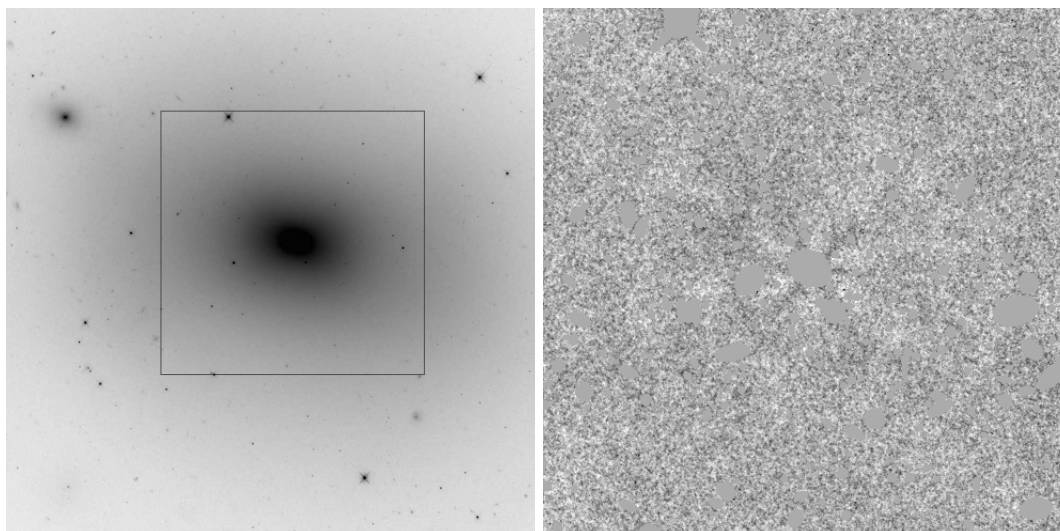
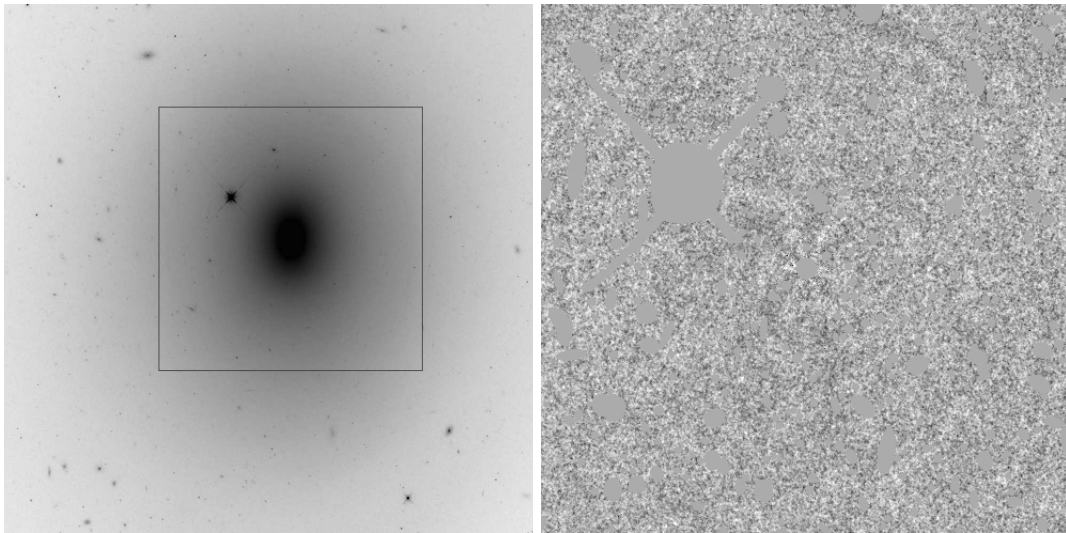**Figure 24.** Combined figure for NGC 890.
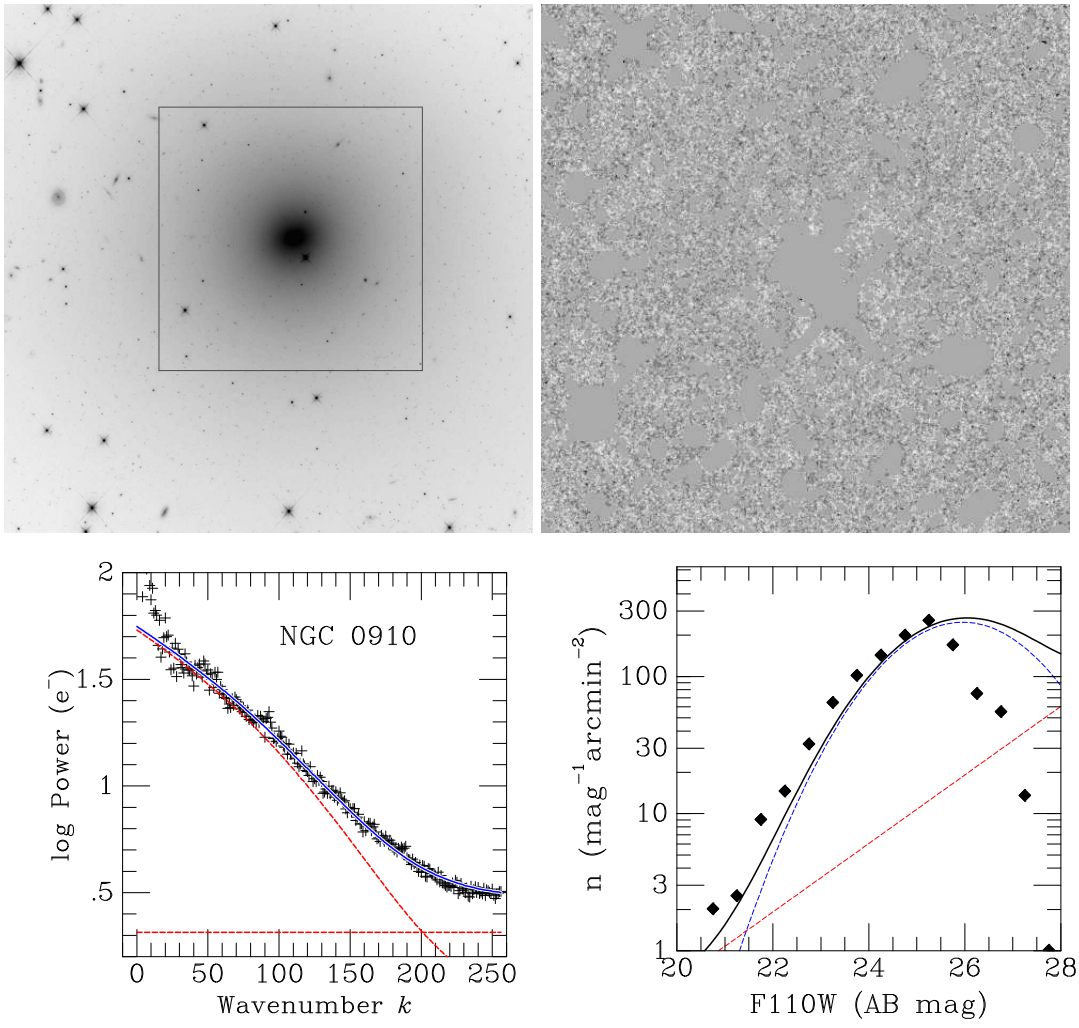
Figure 25. Combined figure for NGC 910.
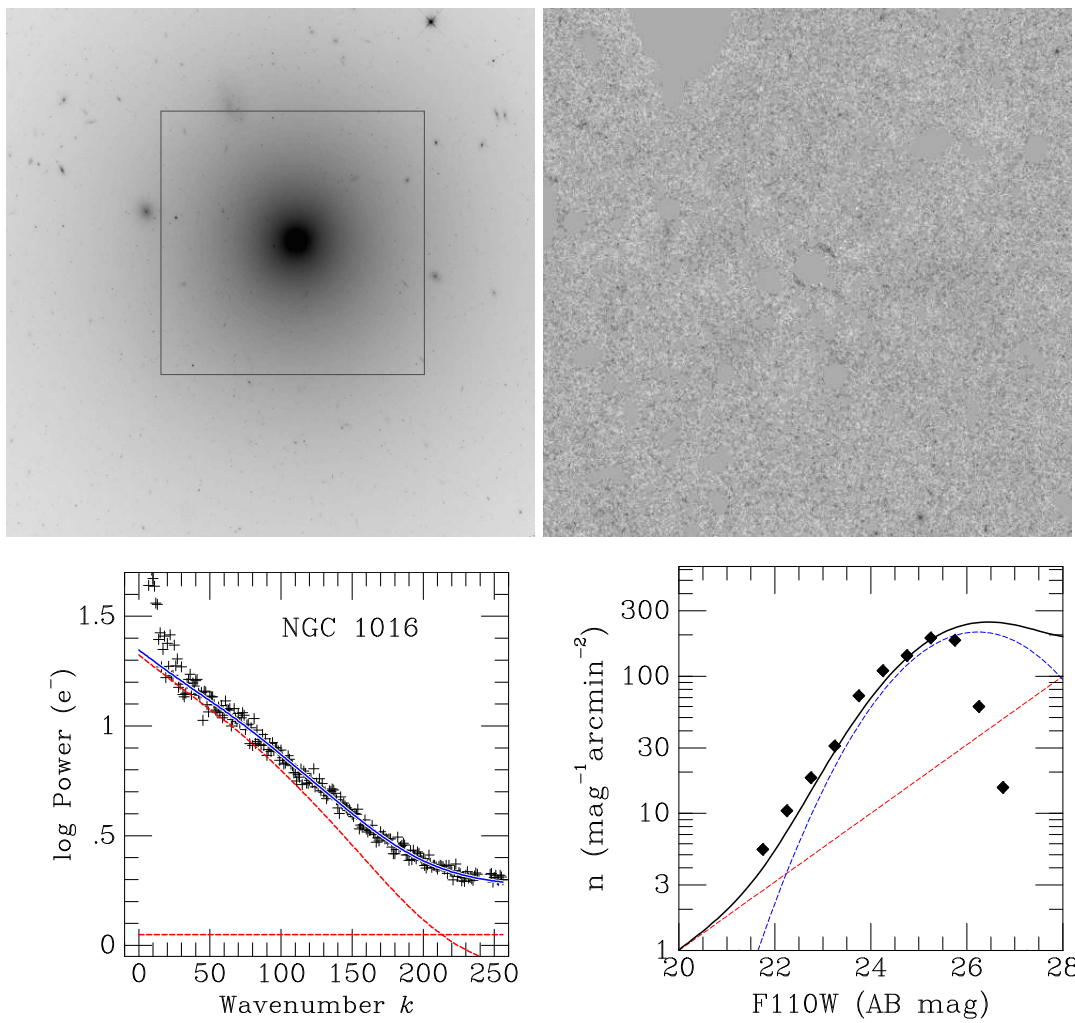
Figure 26. Combined figure for NGC 1016.
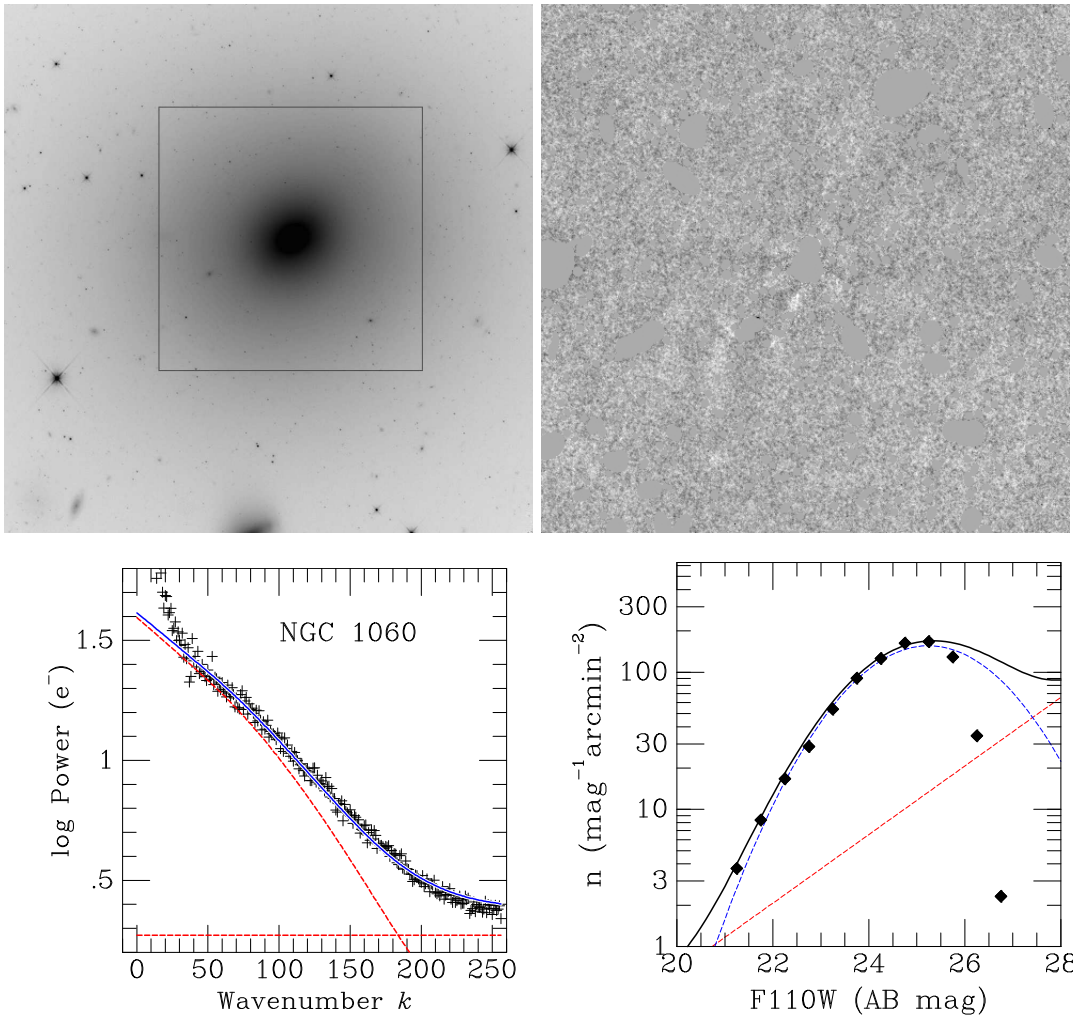
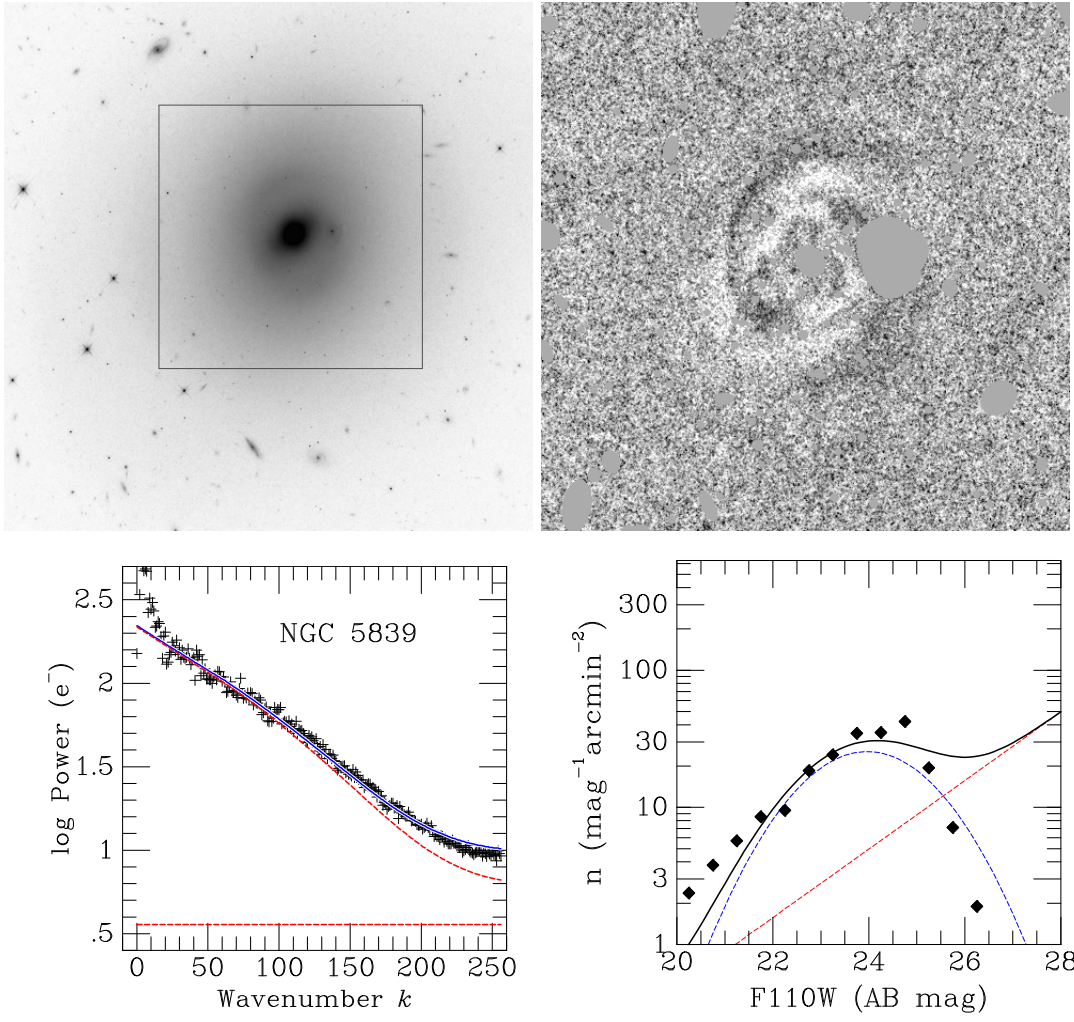**Figure 27.** Combined figure for NGC 1060.
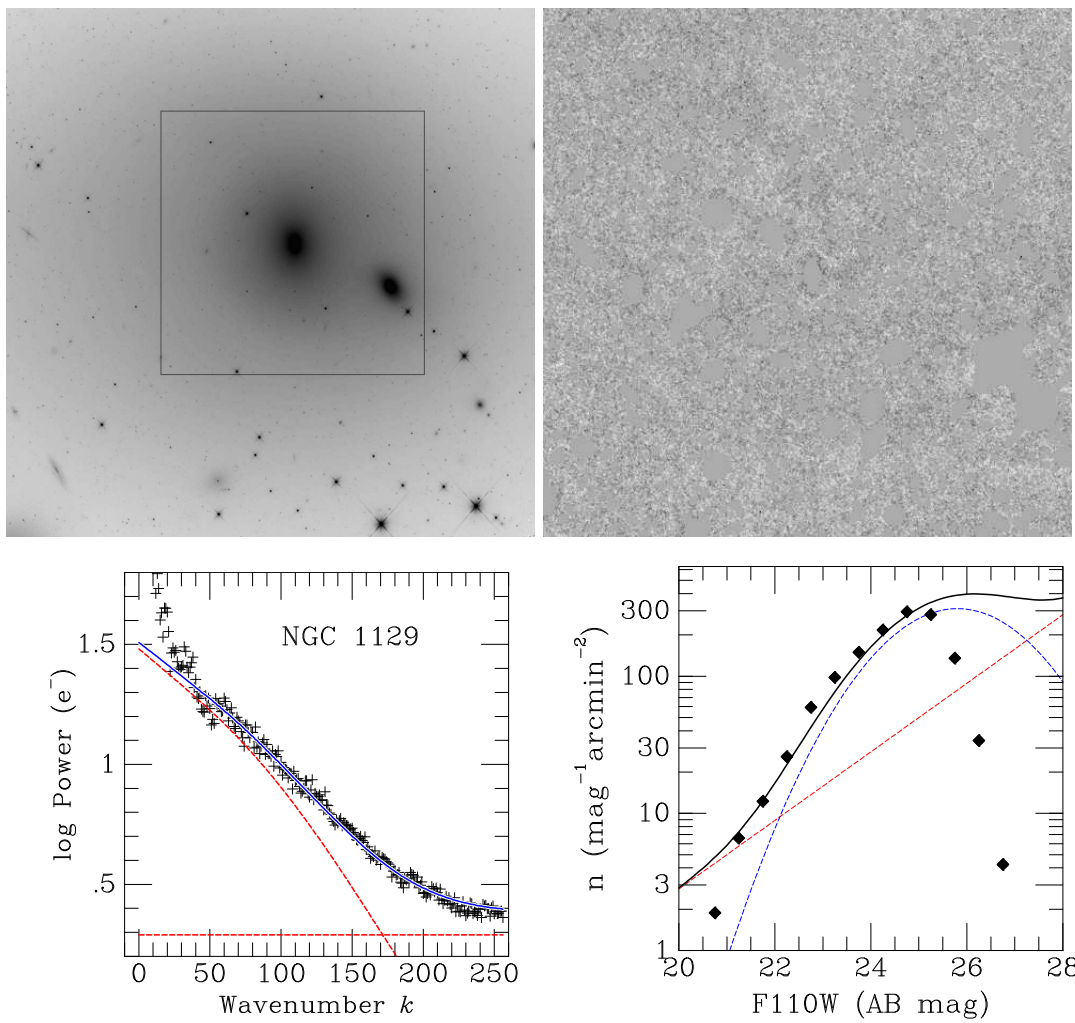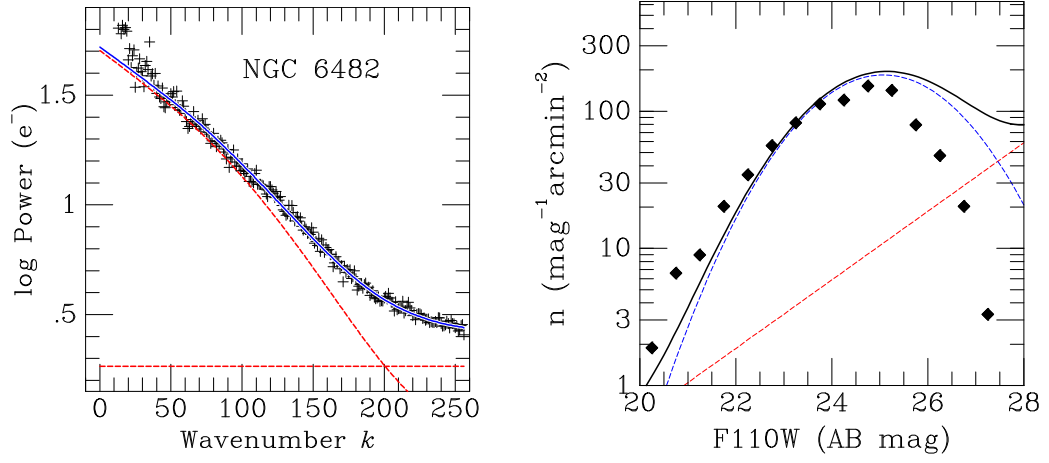
Figure 28. Combined figure for NGC 1129.
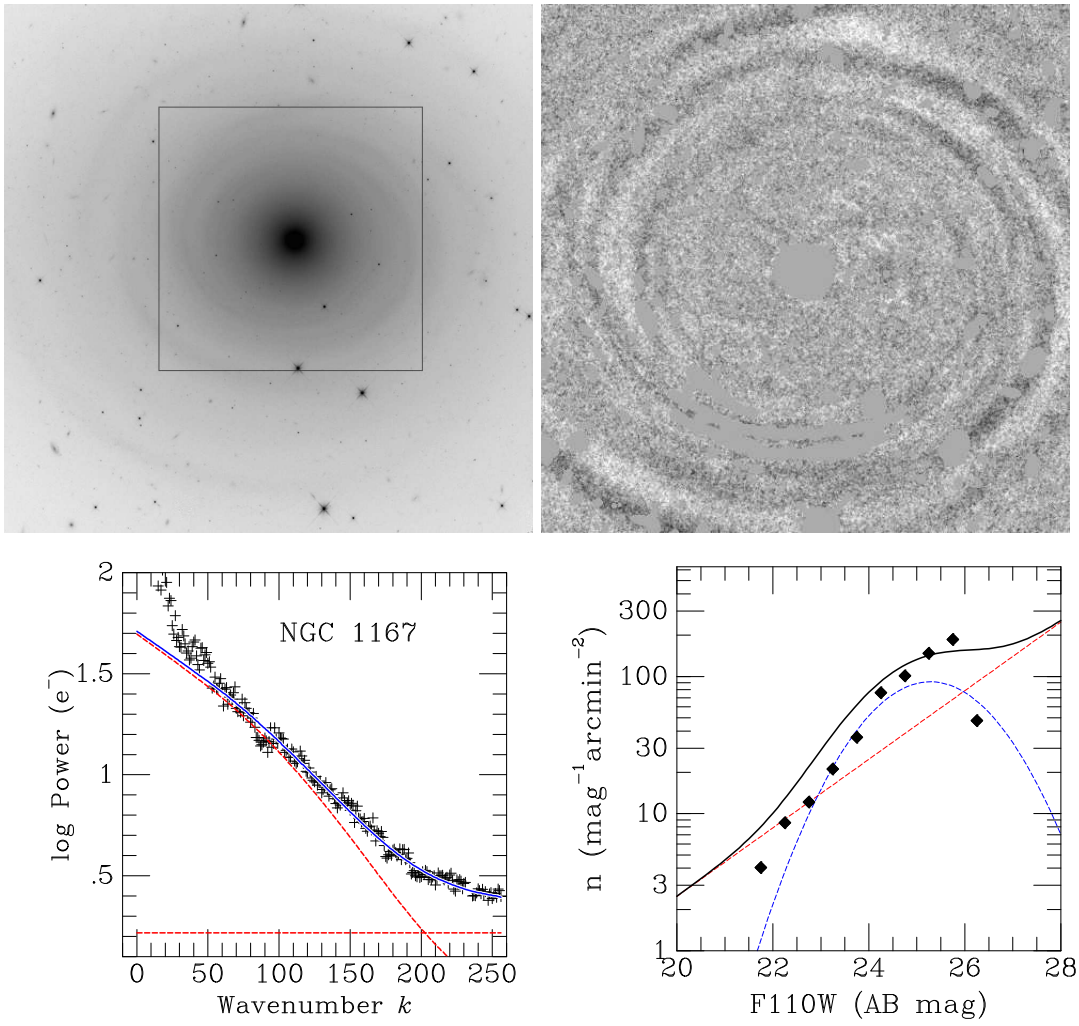
Figure 29. Combined figure for NGC 1167.
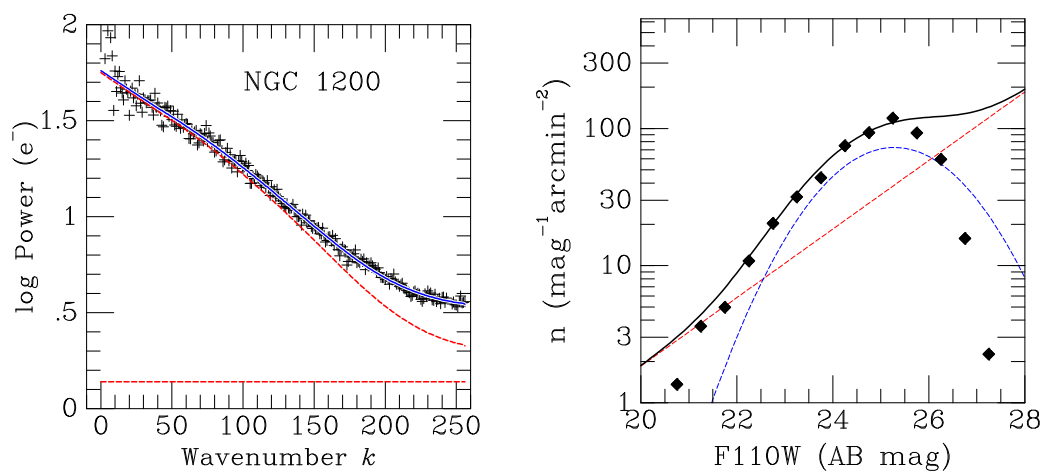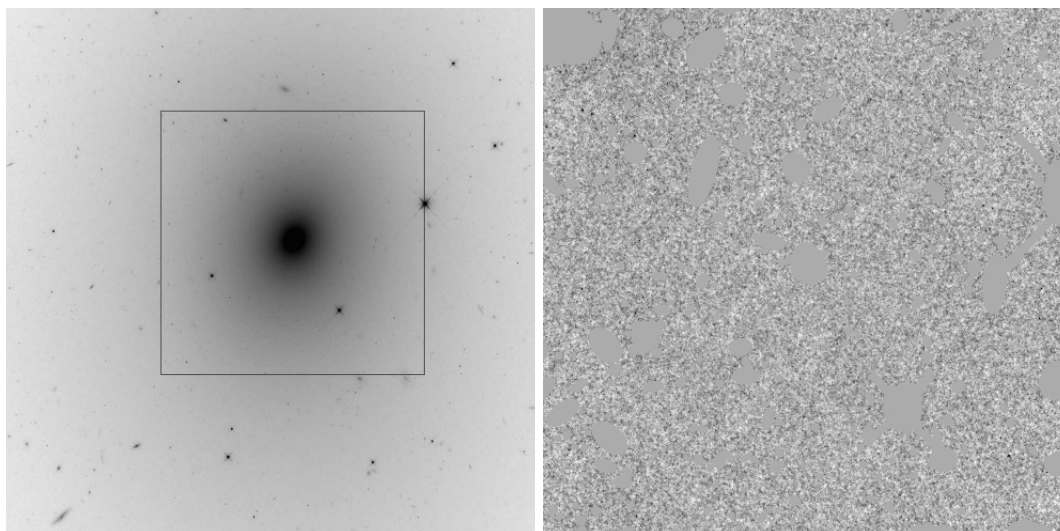
Figure 30. Combined figure for NGC 1200.
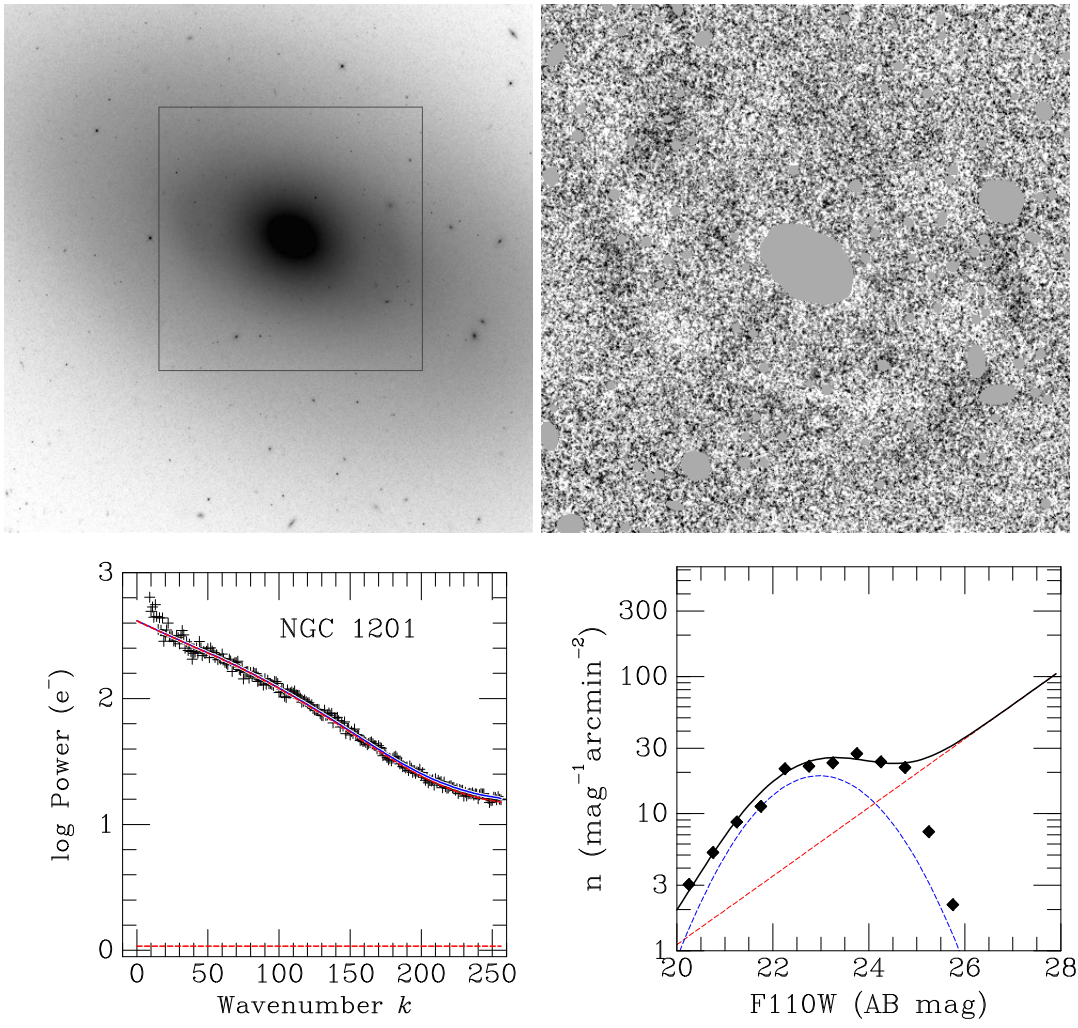
Figure 31. Combined figure for NGC 1201.
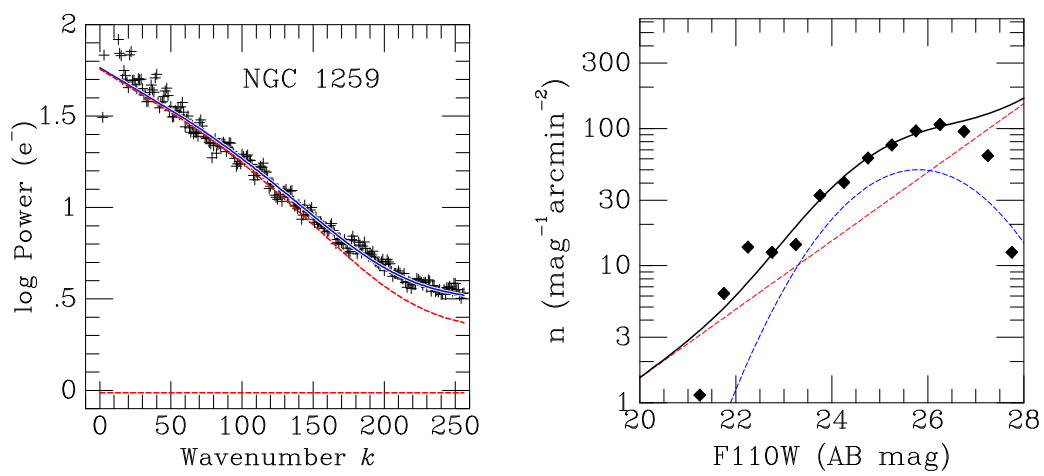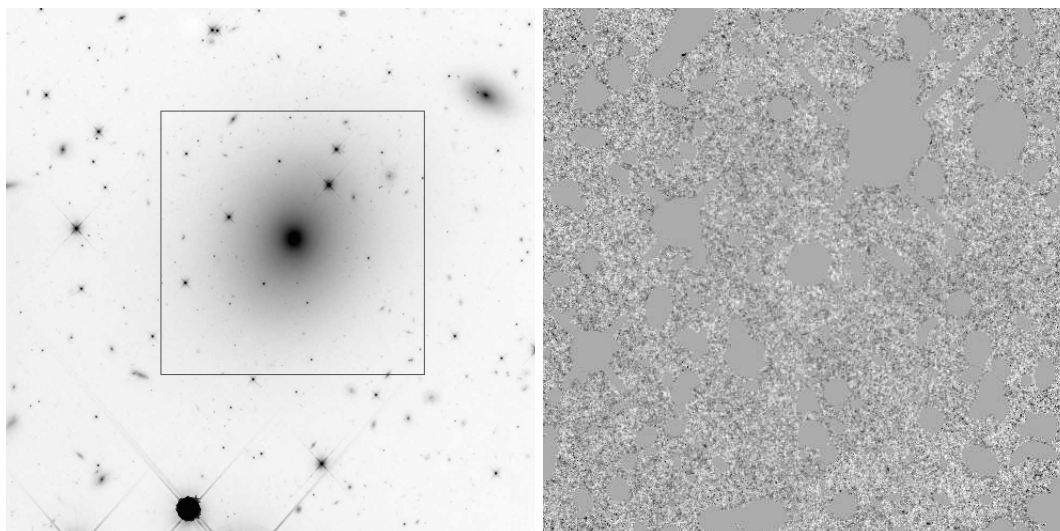
Figure 32. Combined figure for NGC 1259.
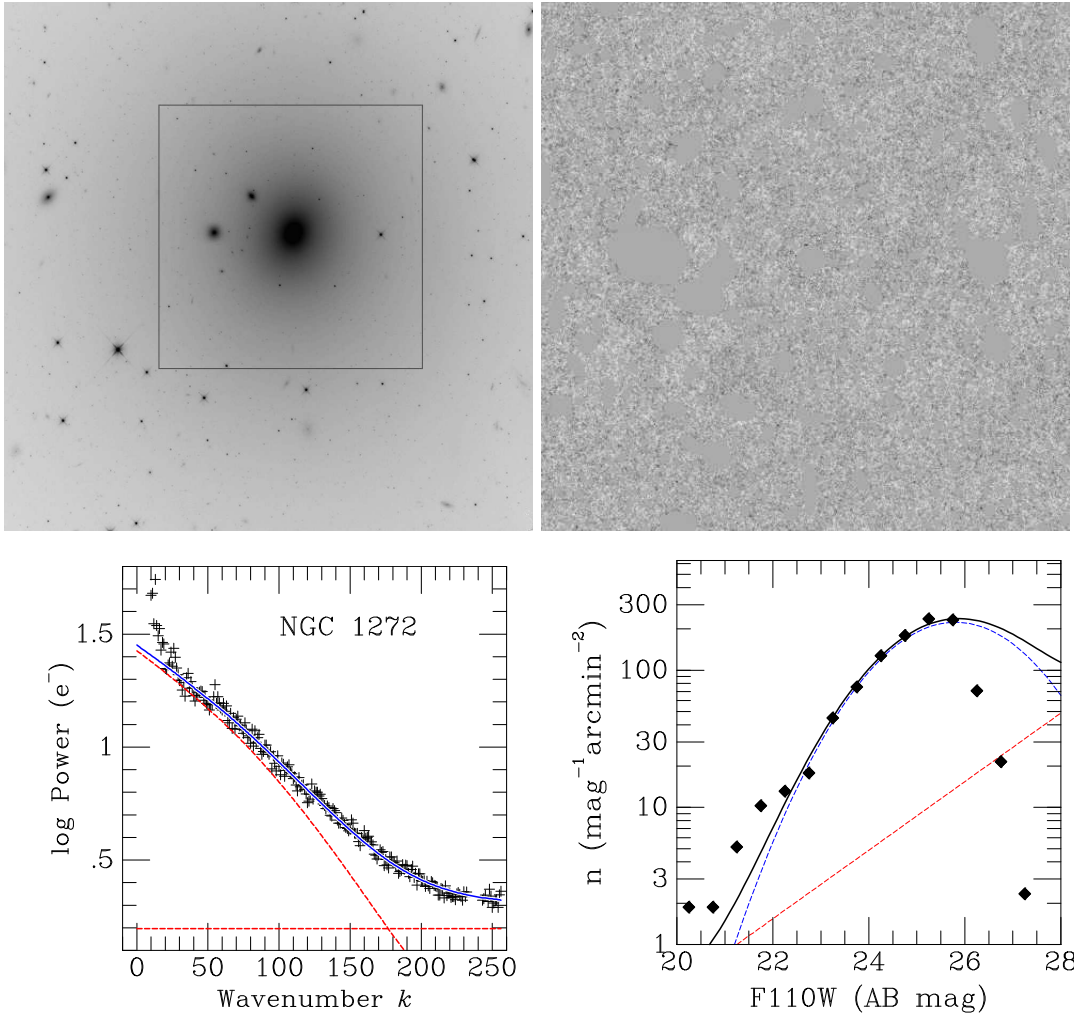
Figure 33. Combined figure for NGC 1272.
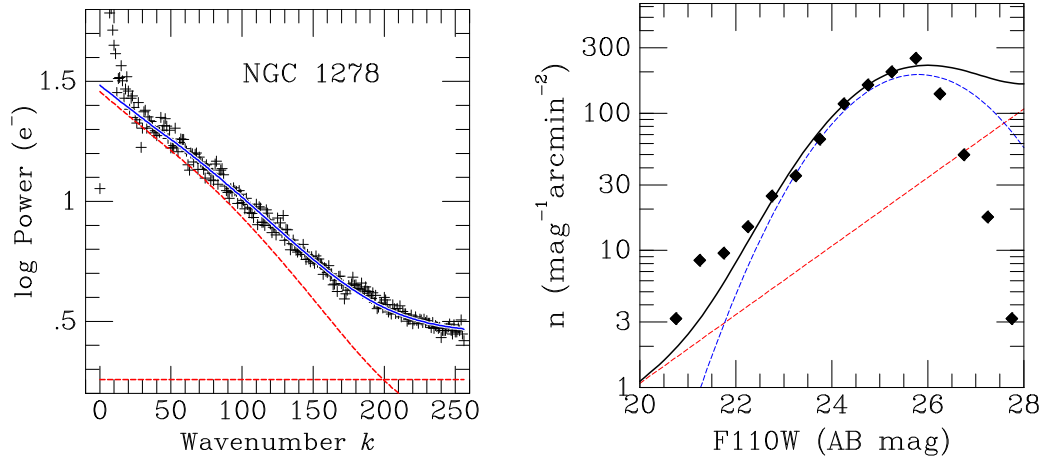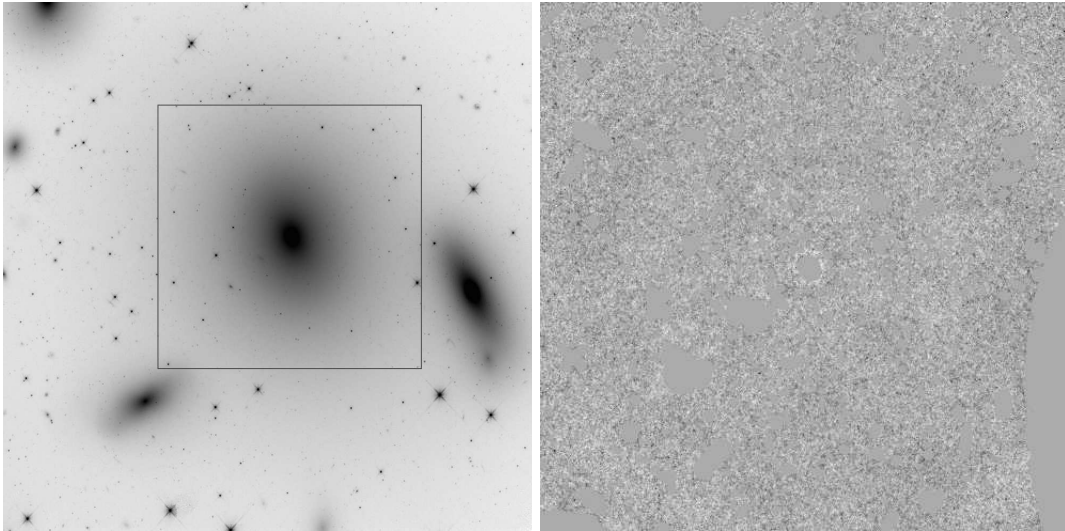
Figure 34. Combined figure for NGC 1278.
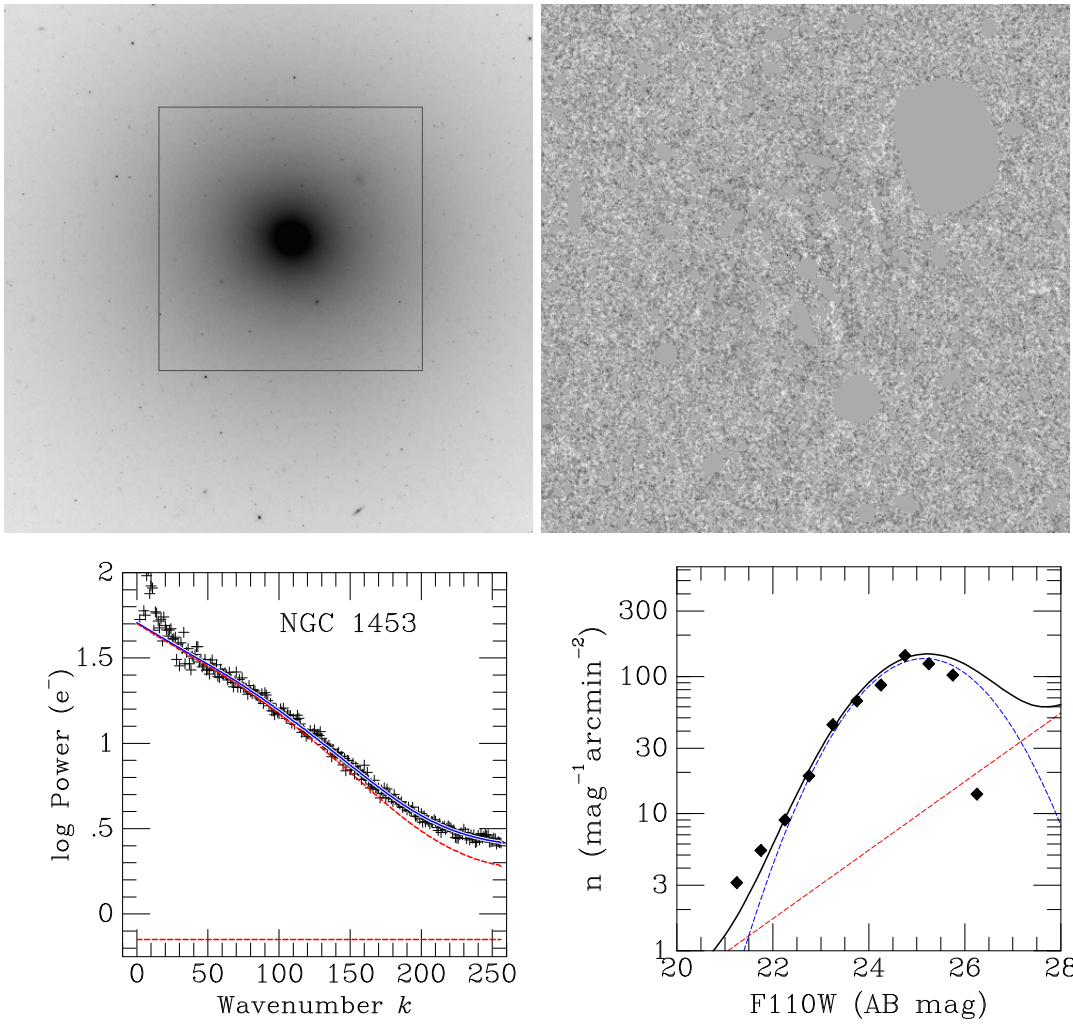
Figure 35. Combined figure for NGC 1453.
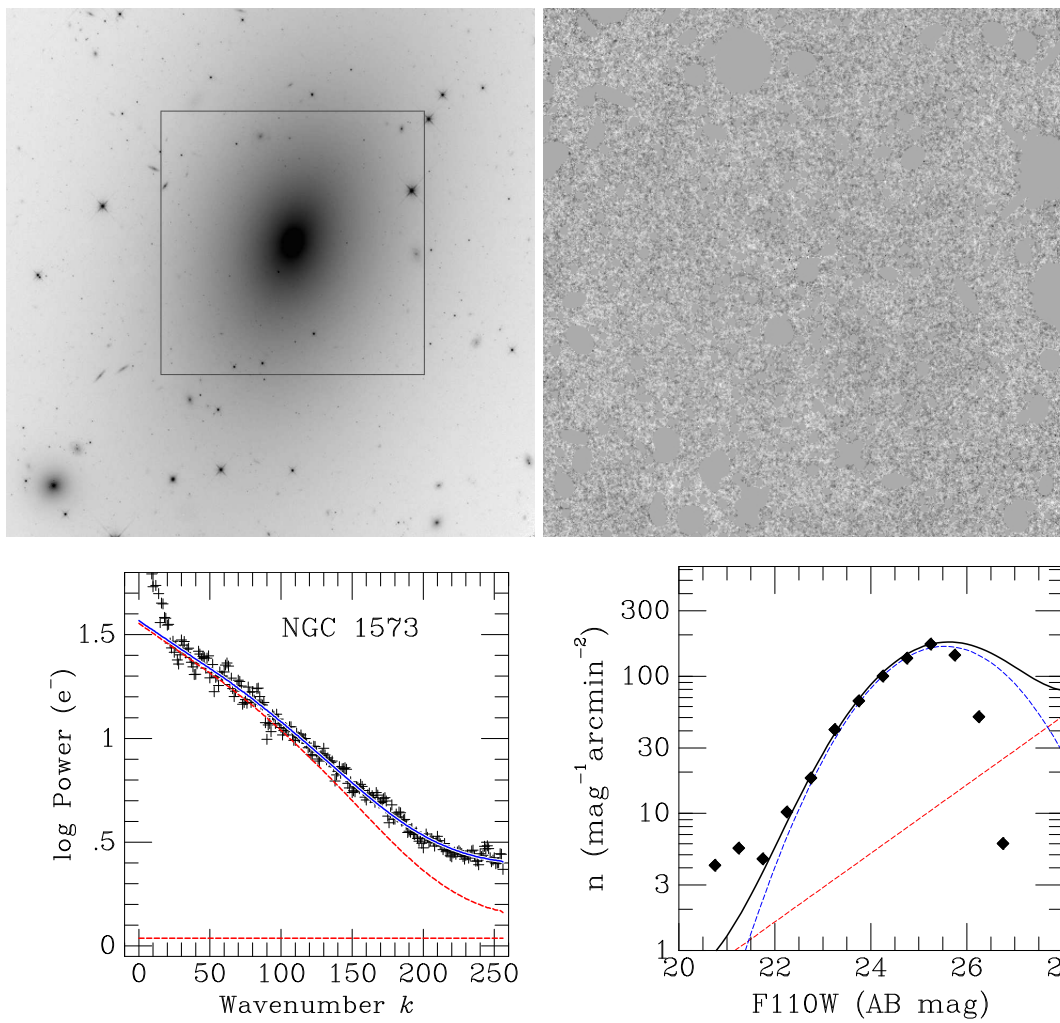
Figure 36. Combined figure for NGC 1573.

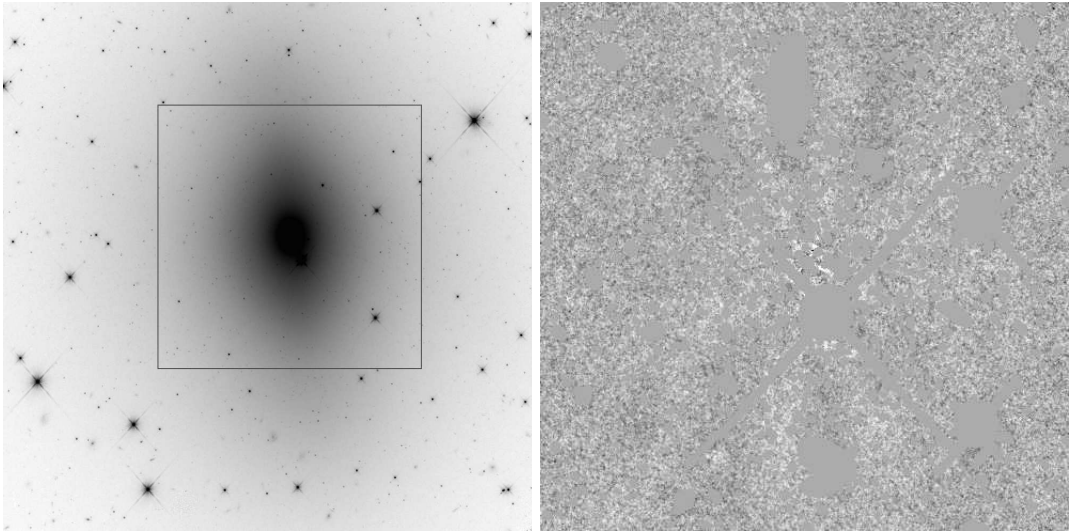**Figure 37.** Combined figure for NGC 1600.

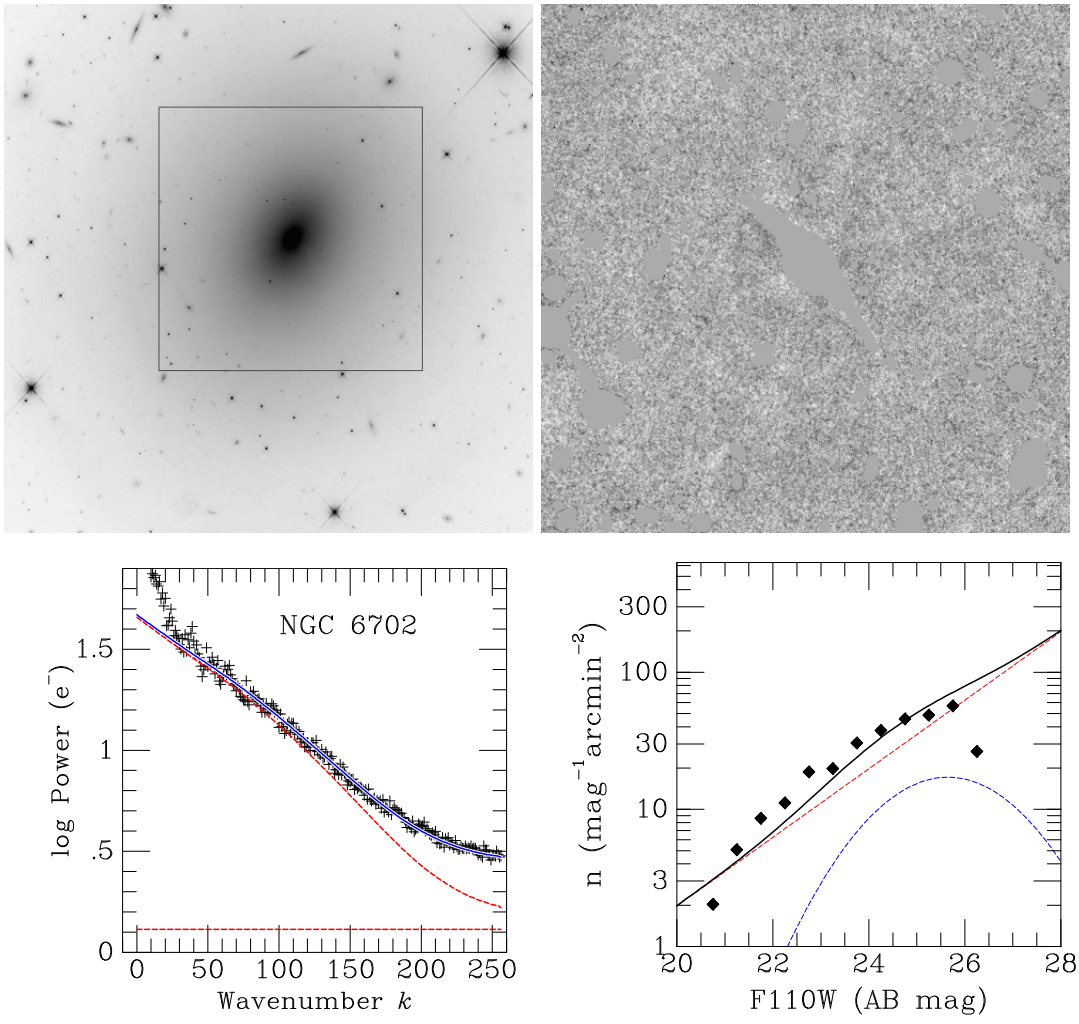**Figure 38.** Combined figure for NGC 1684.

Figure 39. Combined figure for NGC 1700.

Figure 40. Combined figure for NGC 2258.

Figure 41. Combined figure for NGC 2274.

Figure 42. Combined figure for NGC 2340.
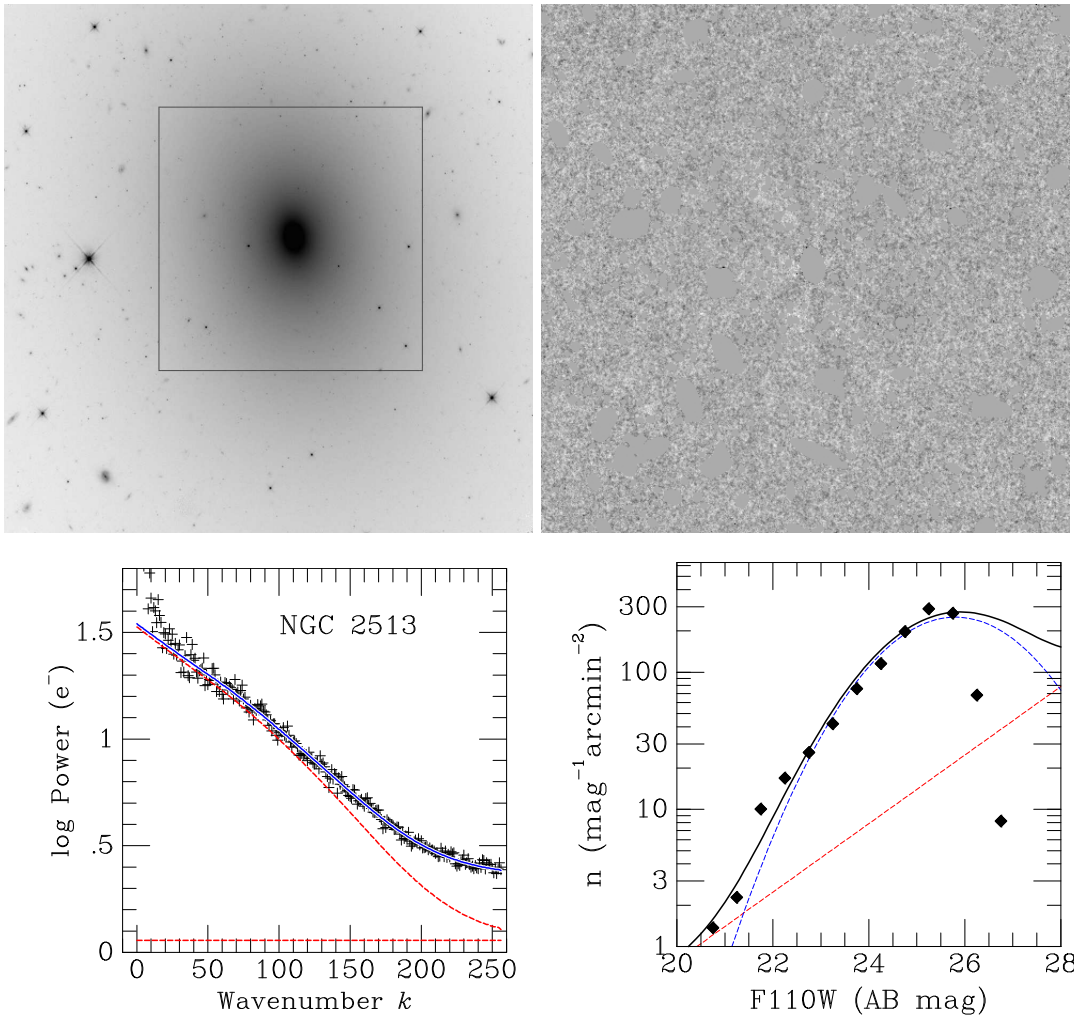
Figure 43. Combined figure for NGC 2513.

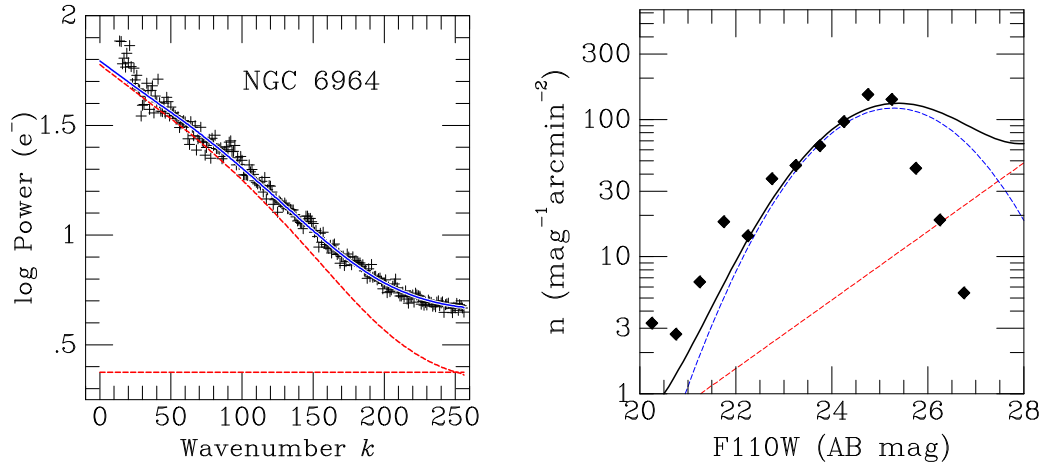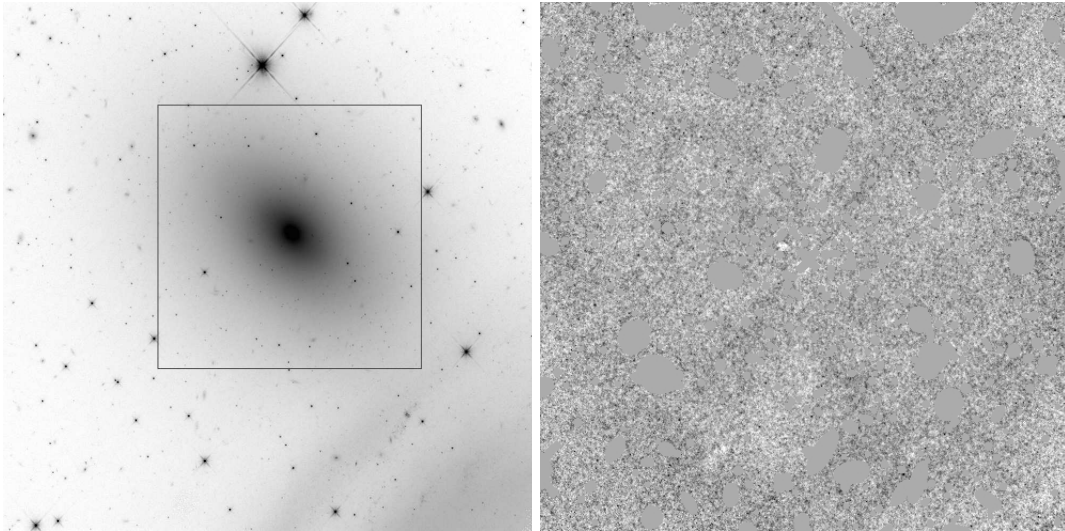**Figure 44.** Combined figure for NGC 2672.
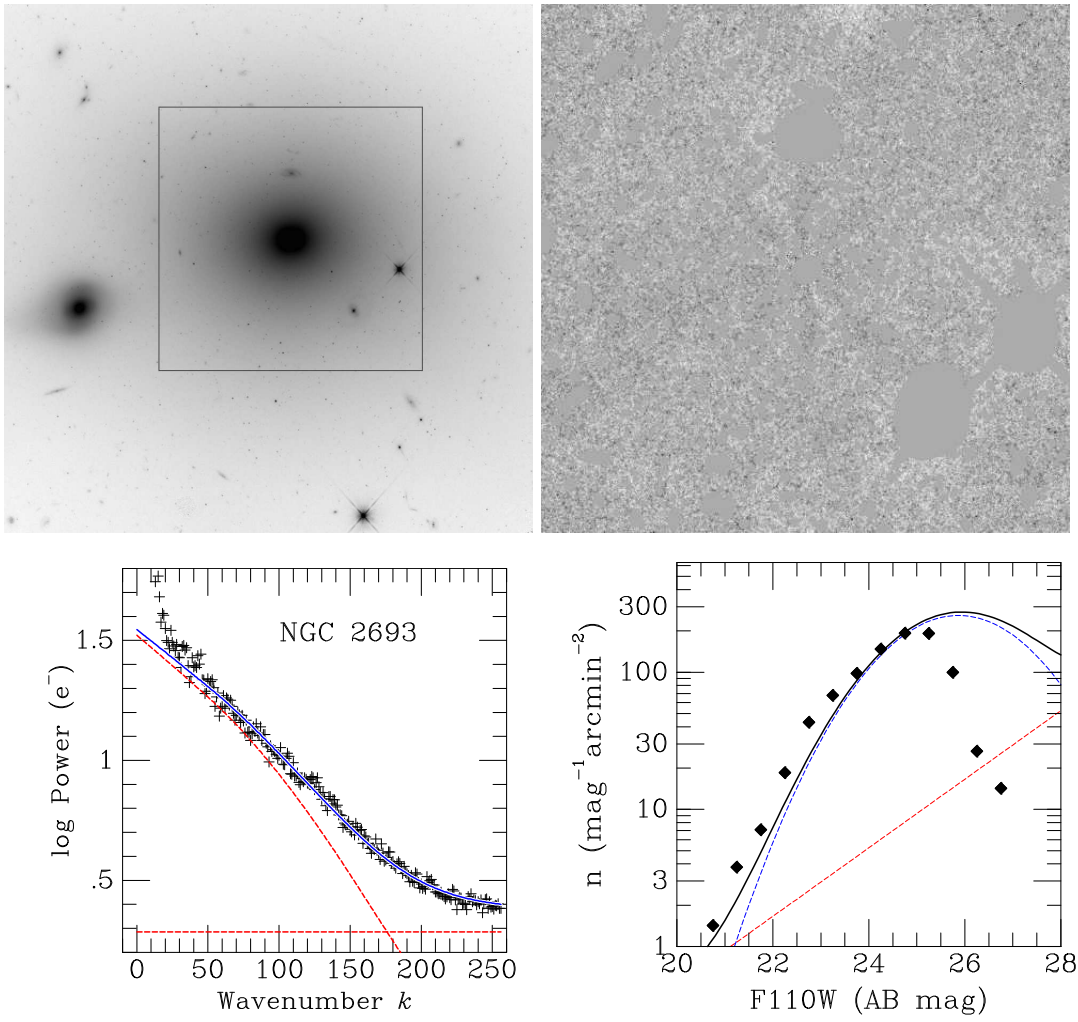
Figure 45. Combined figure for NGC 2693.

Figure 46. Combined figure for NGC 2765.

Figure 47. Combined figure for NGC 2962.

Figure 48. Combined figure for NGC 3158.

Figure 49. Combined figure for NGC 3392.

Figure 50. Combined figure for NGC 3842.

Figure 51. Combined figure for NGC 4036.

Figure 52. Combined figure for NGC 4073.

Figure 53. Combined figure for NGC 4386.

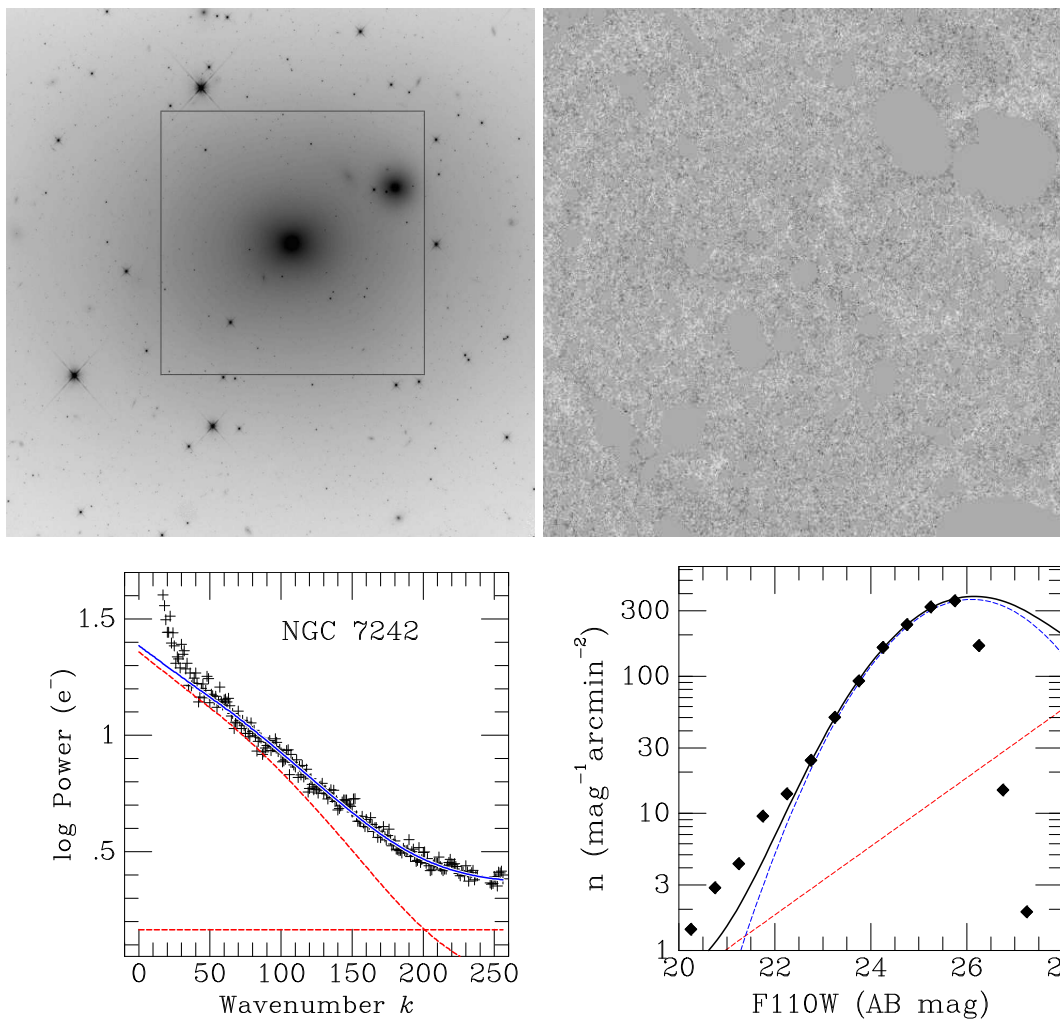**Figure 54.** Combined figure for NGC 4839.

Figure 55. Combined figure for NGC 4874.

Figure 56. Combined figure for NGC 4914.

Figure 57. Combined figure for NGC 5322.

Figure 58. Combined figure for NGC 5353.

Figure 59. Combined figure for NGC 5490.

Figure 60. Combined figure for NGC 5557.

Figure 61. Combined figure for NGC 5839.

Figure 62. Combined figure for NGC 6482.

Figure 63. Combined figure for NGC 6702.

Figure 64. Combined figure for NGC 6964.
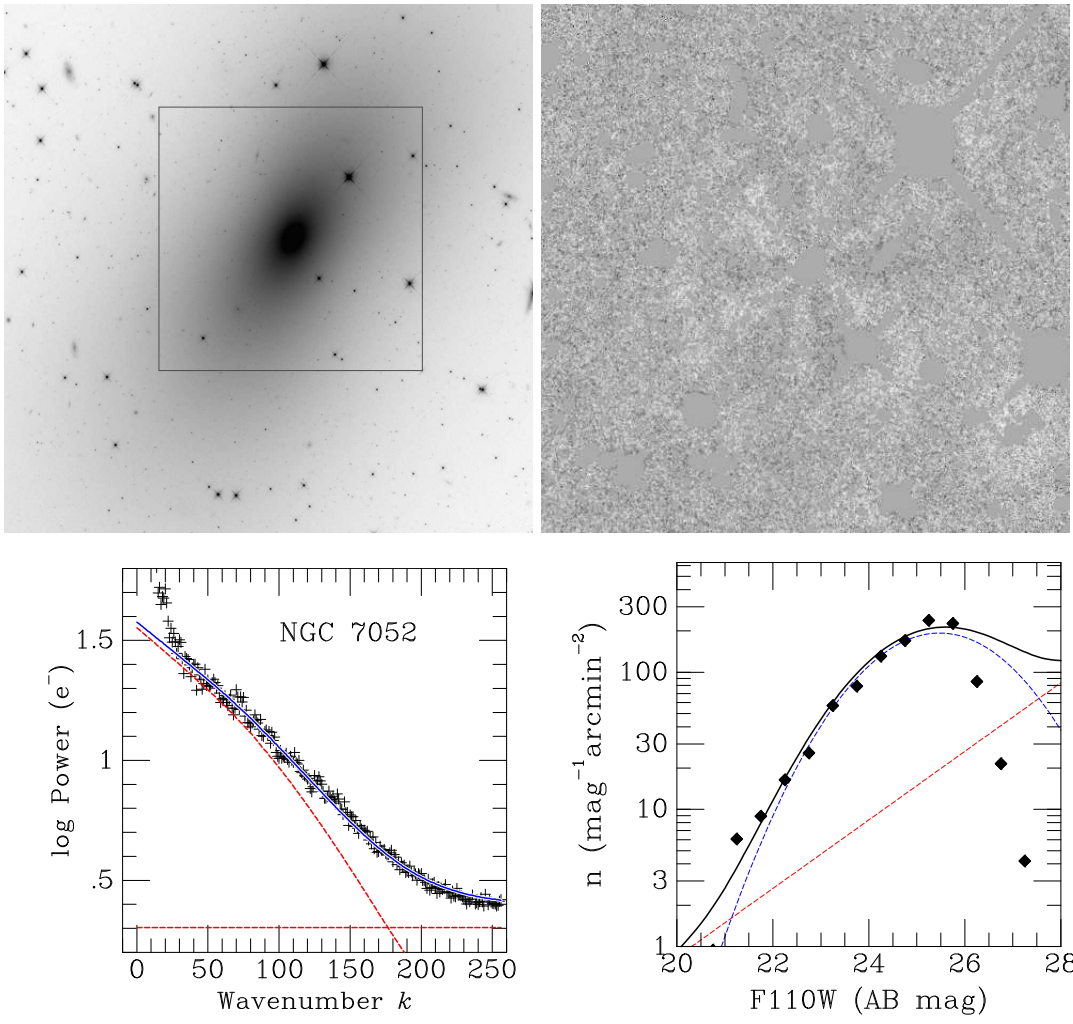
Figure 65. Combined figure for NGC 7052.
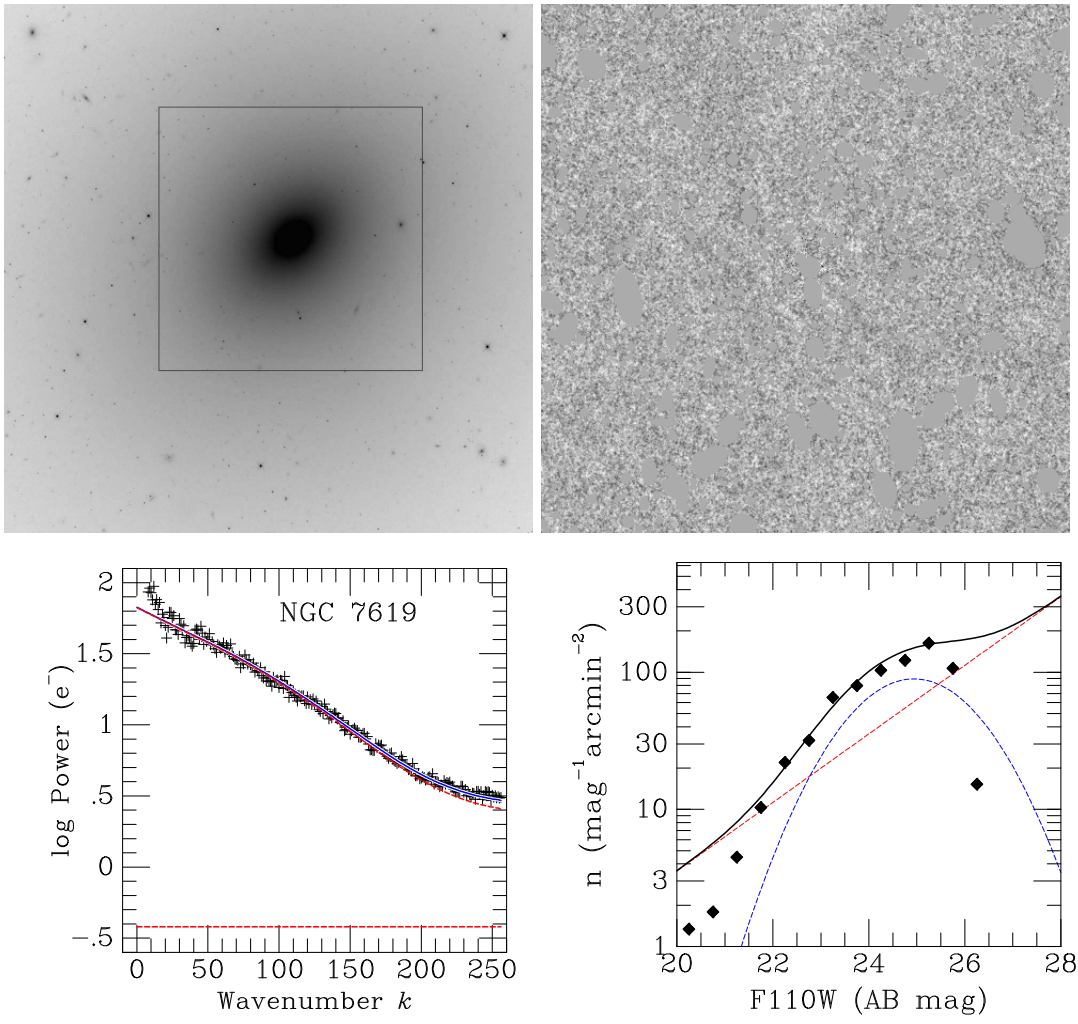
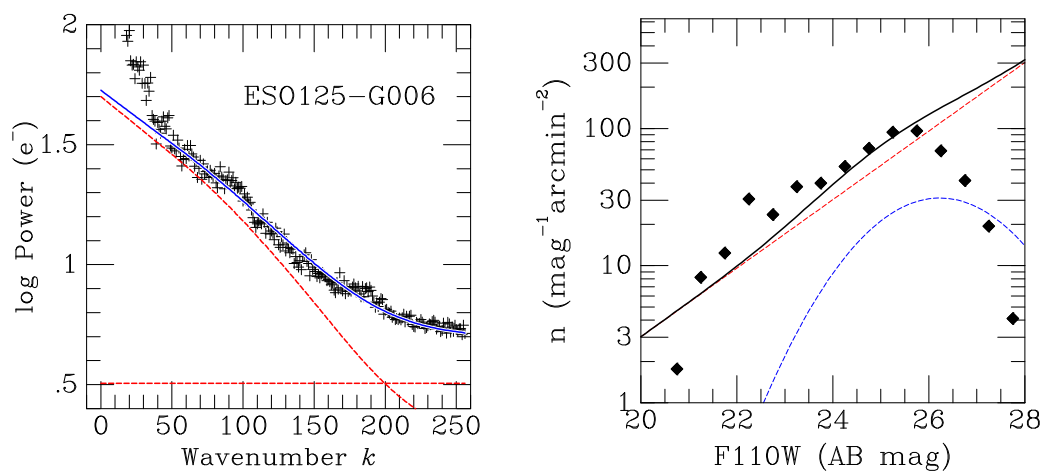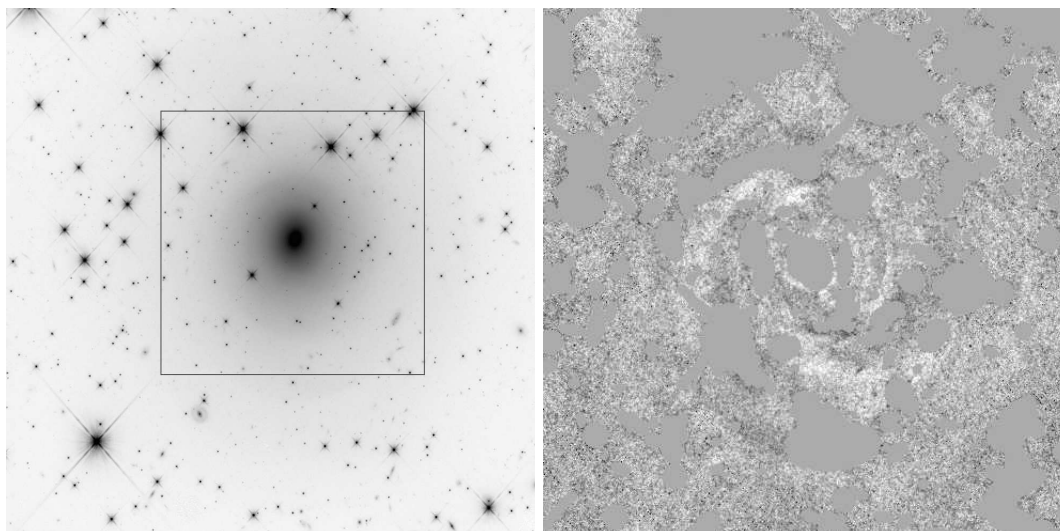**Figure 66.** Combined figure for NGC 7242.

Figure 67. Combined figure for NGC 7619.

Figure 68. Combined figure for ESO125-G006.